Radiation and Strain Effects in Silicon-Germanium Bipolar Complementary Metal Oxide Semiconductor Technology

A Thesis
Presented to
The Academic Faculty

by

Becca M. Haugerud

In Partial Fulfillment
of the Requirements for the Degree
Master of Science
in Electrical and Computer Engineering

Georgia Institute of Technology
April 2005

Radiation and Strain Effects in Silicon-Germanium Bipolar Complementary Metal Oxide Semiconductor Technology

Approved by:

Professor John D. Cressler, Advisor
School of Electrical and Computer Engineering
Georgia Institute of Technology

Professor Joy Laskar
School of Electrical and Computer Engineering
Georgia Institute of Technology

Professor John Papapolymerou
School of Electrical and Computer Engineering
Georgia Institute of Technology

Date Approved: April 18, 2005

ACKNOWLEDGEMENTS

I would like to sincerely thank Dr. John D. Cressler for all his technical guidance and support throughout my master's program. I would also like to acknowledge the other members of my thesis advisory committee, Dr. Joy Laskar and Dr. John Papapolymerou.

I am grateful to Dr. Guofu Niu for his technical insights on the effects of radiation on CMOS devices. I would also like to thank Akil Sutton, Mustayeen Nayeem, Jon Comeau, Ramkumar Krithivasan, A.P. Gnana Prakash, and Sunitha Venkataraman for all their assistance in the completion of this work.

I am grateful to the National Semiconductor SiGe team as well as the IBM SiGe team for providing wafers used in these studies. I would also like to thank the following for supporting this work: BAE Systems, DTRA under the Radiation Hardened Microelectronics Program, NASA-GSFC under the Electronics Radiation Characterization Program, DARPA, and the Georgia Electronic Design Center at Georgia Tech. The assistance of Paul Marshall, Cheryl Marshall, and Ray Ladbury made the radiation experiments possible and is greatly appreciated. In addition, I wish to thank Dr. Rona Belford and Lloyd Bosworth for their help in the strain application process.

Finally, I am grateful to my family and friends for their support throughout my life.

TABLE OF CONTENTS

LIST OF TABLES

LIST OF FIGURES

SUMMARY

This work examines the effects of radiation and strain on silicon-germanium (SiGe) heterojunction bipolar transistor (HBT) BiCMOS technology. First, aspects of the various SiGe HBT BiCMOS technologies and the device physics of the SiGe HBT are discussed. The performance advantages of the SiGe HBT over the Si BJT are also presented.

Chapter II offers a basic introduction to key radiation concepts. The space radiation environment as well as the two common radiation damage mechanisms are described. An overview of the effects of radiation damage on Si-based semiconductor devices, namely bipolar and CMOS, is also presented.

Next, the effects of proton and gamma radiation on a new first-generation SiGe HBT technology are investigated. The results of a differential SiGe HBT LC oscillator subjected to proton irradiation are also presented as a test of circuit-level radiation tolerance. Finally, a technology comparison is made between the results of this work and the three different previously reported SiGe technologies. All reported SiGe HBT technologies to date show acceptable proton radiation tolerance up to Mrad levels.

Chapter IV investigates the effects of effects of mechanical planar biaxial strain in SiGe HBT BiCMOS technology. This novel strain method is applied post fabrication, unlike many other straining methods. We report increases in the nFET saturated drain current, transconductance, and effective mobility for an applied strain of 0.123%. The pFET device performance degrades for this type of low-level strain.

CHAPTER I

INTRODUCTION

1.1 Motivation

Silicon-germanium (SiGe) heterojunction bipolar transistor (HBT) BiCMOS technology offers significant performance enhancement over silicon (Si) bipolar technology. The combination of the high performance of the SiGe HBT with state-of-the-art CMOS provides several advantages over III-V semiconductors for mixed-signal applications, such as lower cost, ease of CMOS integration, and higher yield. SiGe BiCMOS technology gives device and circuit designers flexibility on several levels [1]. Device designers can use the SiGe HBT to achieve frequencies that are impossible to attain in Si technologies. Circuit designers can trade the SiGe HBT's excess gain-bandwidth for other key figures-of-merit in a given application, such as low power or low noise.

Designers of RF and microwave circuits for spaceborne satellite systems are increasingly using high performance terrestrial devices as opposed to radiation-hardened devices in their designs as a cost saving measure [2]. Radiation testing and hardness assurance of such devices is a necessity before they are subjected to the harsh radiation environment of space. Previous reports indicate that SiGe BiCMOS technology is quite tolerant to various types of radiation and is a viable candidate for high-speed, low-cost space applications [3]. Thus, the results of space qualification testing on new SiGe technologies is of great interest to the space community.

Dimensional scaling of CMOS technology has long yielded enhanced device performance, higher MOSFET packing density, and most importantly lower cost. However, today as scaling becomes increasingly difficult and expensive, other alternatives to dimensional scaling are being investigated. Strained silicon (Si) is garnering attention because of the

substantial enhancements in carrier mobility observed in this material. Strained Si CMOS has presented itself as a feasible way of enhancing the device performance without scaling the device dimensions.

This thesis investigates the effects of radiation and strain on various SiGe HBT BiCMOS technologies. The proton and gamma radiation tolerance of a new commercial SiGe HBT is investigated for the first time. This work also examines the impact of irradiation substrate bias on proton damage in 130 nm CMOS technology. Finally, the effects of mechanical planar biaxial tensile strain applied, post fabrication, to SiGe HBT BiCMOS technology are investigated. Results presented in this thesis have been presented at the 2004 Topical Meeting on Silicon Monolithic Integrated Circuits in RF Systems. This work has also been accepted for publication in *Solid-State Electronics* under the title "The Effects of Mechanical Planar Biaxial Strain in Si/SiGe HBT BiCMOS Technology" [4]. The results of proton damage in 130 nm CMOS will be presented at the 2005 IEEE Radiation Effects Data Workshop [5]. The results of the proton and gamma radiation investigation on a new SiGe HBT will be submitted to *Solid-State Electronics* [6].

1.2 SiGe HBT BiCMOS Technology

SiGe HBT BiCMOS technology is widely recognized as a suitable candidate for a host of analog, digital, and RF through mm-wave circuit applications. This technology also combines SiGe HBTs with state-of-the-art CMOS. The SiGe HBT uses bandgap engineering to achieve III-V like performance while maintaining compatibility with conventional Si CMOS manufacturing. This technology allows for system-on-a-chip (SoC) integration.

A SiGe HBT is formed by introducing a SiGe epi layer into the base of a Si bipolar junction transistor (BJT). This layer typically consists of a Si buffer, boron-doped graded SiGe alloy active layer, and a Si cap. A significant difference between the SiGe HBT and a Si BJT is the fact that epitaxial growth allows the base to be more heavily doped at a given base width which leads to lower base resistance and improved dynamic response [3].

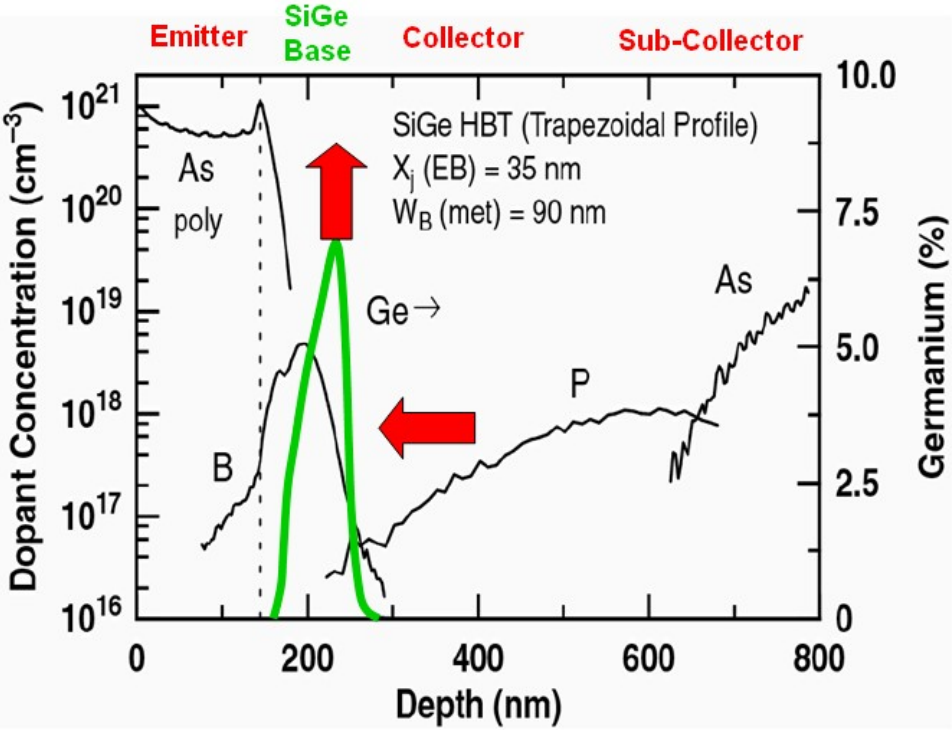

Figure 1: Representative SIMS profile for a first generation SiGe HBT.

Figure 1 depicts a SIMS doping and Ge profile for a representative first generation SiGe HBT.

Several SiGe HBT BiCMOS technologies are investigated in this work. The first is the National BiCMOS8 SiGe HBT process technology, which is a new commercial offering. This first-generation SiGe HBT BiCMOS technology is a six metal layer process comprised of standard and high breakdown SiGe HBTs, along with low and high voltage CMOS, and a variety of passive elements. This process, as with most SiGe HBT technologies, features a self-aligned emitter-base junction, in-situ doped polysilicon emitter, and shallow and deep trench isolation. A schematic cross-section is shown in Figure 2 and a SEM cross-section is depicted in Figure 3. The standard high-performance SiGe HBT in this process has a 0.4 μm emitter stripe width, achieves a peak f_T of 60 GHz, a peak f_{max} of 60-70 GHz, and a BV_{CEO} of 3.3V. The low voltage CMOS has a minimum length of 0.24 μm with 2.75V V_{DD} and the high voltage CMOS features a minimum length of 0.4 μm with 3.6V V_{DD}.

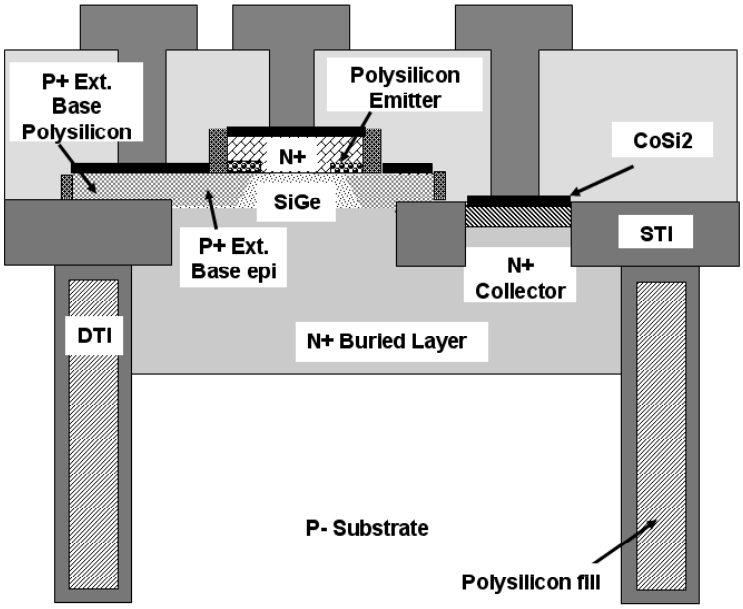

Figure 2: A schematic device cross-section of the National BiCMOS8 SiGe HBT.

Another first generation technology used in this work is the IBM 5HP technology, which is a three metal layer process that integrates nominal and high breakdown SiGe HBTs with 0.35 μm CMOS, and also includes RF passives elements. The nominal breakdown SiGe HBT features a 0.5 μm drawn emitter stripe width, 47 GHz peak f_T, 69 GHz peak f_{max}, and a BV_{CEO} of 3.3V. The CMOS has an effective length of 0.35 μm with 3.3V V_{DD} [7]. The third SiGe BiCMOS technology investigated is the second generation IBM 7HP. This is a laterally and vertically scaled version of the 5HP technology with full copper metalization. This process combines a 0.2 μm drawn emitter width, BV_{CEO} of 2.5V, peak f_T of 120 GHz, and peak f_{max} of 100 GHz SiGe HBT with three distinct 0.18μm Si CMOS device versions. The nominal threshold voltage and high threshold voltage have minimum length of 0.18 μm with 1.8V V_{DD}, and the thick oxide CMOS has a minimum length of 0.3 μm with 3.3V V_{DD}[8]. A schematic cross-section of the SiGe HBT and CMOS devices (nFET) is depicted in Figure 4.

A fully-integrated third generation 200 GHz SiGe BiCMOS technology (IBM 8HP) is also investigated. This process incorporates a 0.12 μm drawn emitter stripe width, 207

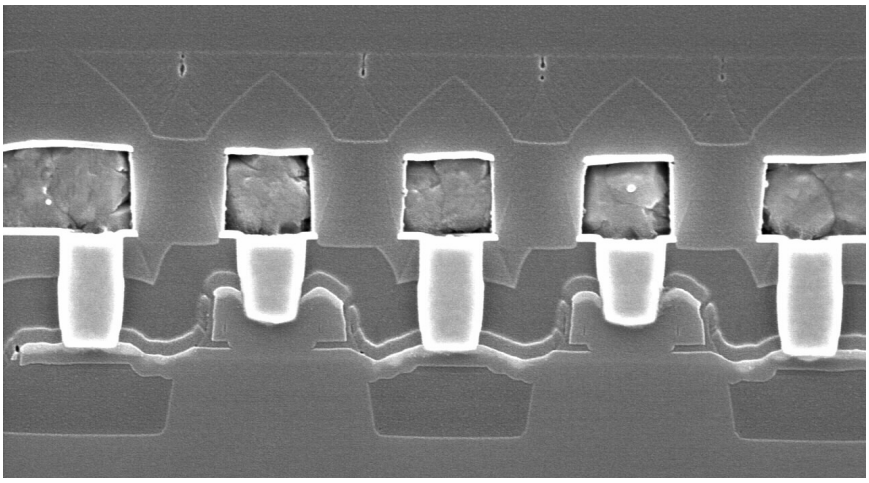

Figure 3: SEM device cross-section of the National BiCMOS8 SiGe HBT.

GHz f_T, 285 GHz f_{max}, and 1.7V BV_{CEO} SiGe HBT with 130 nm Si CMOS technology (having an effective minimum gate length of 0.12μm). Two types of Si CMOS devices are available in this technology (1.2V and 2.5V), with minimum channel lengths of 0.12 μm and 0.24 μm, respectively [9]. The performance metrics of the SiGe BiCMOS technologies discussed in this work are summarized in Table 1.

1.3 Device Physics of SiGe HBTs

This section describes the operation of the SiGe HBT as compared to a similarly constructed Si BJT [3]. As mentioned above, the SiGe HBT is formed by introducing a SiGe alloy into the base of a Si BJT. The SiGe HBT uses bandgap engineering in Si to achieve III-V like performance while maintaining compatibility with conventional Si CMOS manufacturing. The SiGe film is grown pseudomorphically on a Si substrate resulting in biaxial compressive strain in the film. The addition of Ge to Si alters the band structure from that of pure Si. Ge has a smaller bandgap energy than Si (0.66 eV and 1.12 eV respectively), consequently SiGe has a smaller bandgap than Si. The compressive strain in the SiGe film also alters both the conduction and valence bands yielding an additional bandgap reduction. The strain splits the previously degenerate 6-fold Si conduction band into 2-fold

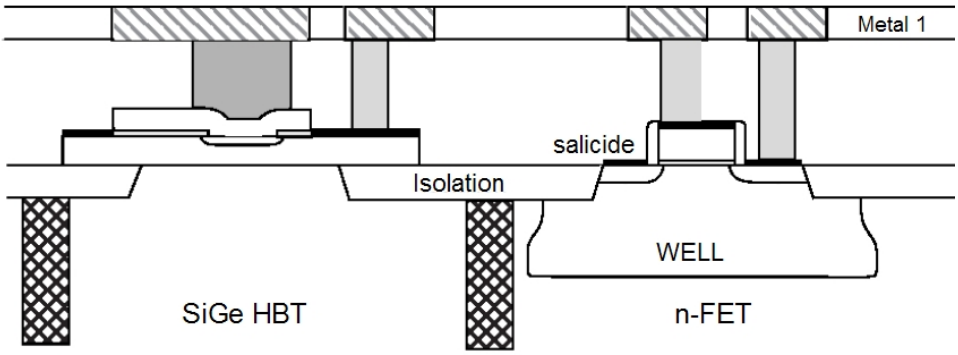

Figure 4: Schematic cross-section of the 7HP SiGe HBT BiCMOS technology.

Table 1: Target device parameters for various SiGe BiCMOS technologies.

SiGe BiCMOS Technology	National BiCMOS8	IBM 5HP	IBM 7HP	IBM 8HP
SiGe HBT Parameters				
Drawn Emitter Width (μm)	0.4	0.5	0.2	0.12
V_A (V)	175	65	120	150
BV_{CEO} (V)	3.3	3.3	2.5	1.7
Peak f_T (GHz)	60	48	120	207
Peak f_{max} (GHz)	60-70	69	100	285
nFET Parameters				
Channel L (μm)	0.24	0.35	0.18	0.12
V_{DD} (V)	2.75	3.3	1.8	1.2

and 4-fold degenerate bands. Compressive strain also alters the valence band by splitting the heavy-hole and light-hole bands. In total, the bandgap reduces by approximately 75 meV for every 10% Ge introduced. The majority of the Ge induced band offset occurs in the valence band, which is desired for npn transistors. The Si-SiGe heterojunctions in the emitter-base (EB) and collector-base (CB) junctions of the SiGe HBT contribute to the significant performance enhancement, both *dc* and *ac*, over the Si BJT. A look at the energy band diagrams for a graded-base SiGe HBT and an identically fabricated Si BJT (Figure 5) biased in forward active mode depicts the band structure changes described above. Due to the presence of Ge in the base, there is a slight reduction in the base bandgap at the EB junction ($\Delta E_{g,Ge}(x = 0)$) and a much larger reduction at the CB junction ($\Delta E_{g,Ge}(x = W_b)$).

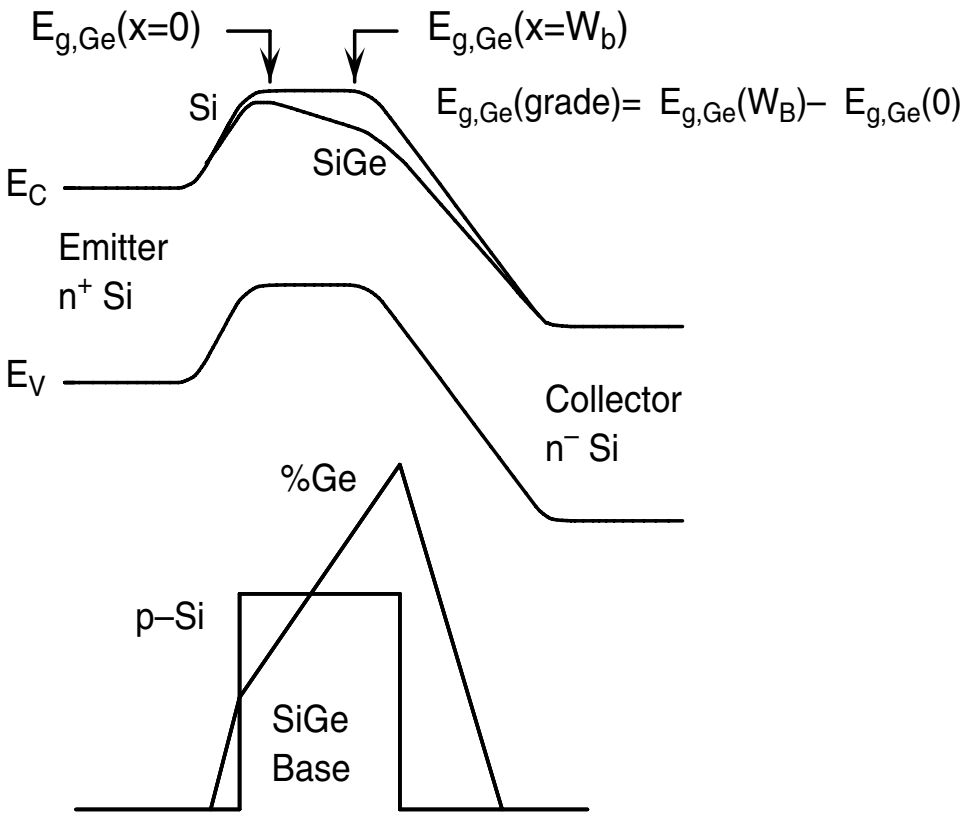

Figure 5: Energy band diagram for a graded base SiGe HBT and a Si BJT.

This position dependent bandgap change is due to the grading of Ge across the base and induces a built-in electric field in the neutral base region. The induced field positively impacts the minority carrier transport.

From Figure 5, we see that the emitter-base potential barrier is reduced in the SiGe HBT with respect to the Si BJT, thereby allowing increased electron injection from emitter to base. The enhanced electron injection leads to a higher collector current and current gain. An expressions for the collector current density (J_C) can be derived in closed-form from the generalized Moll-Ross J_C relation [10],

$$J_C = \frac{q(e^{qV_{BE}/kT-1})}{\int_0^{W_b} \frac{p_b(x)dx}{D_{nb}(x)n_{ib}^2(x)}} \tag{1}$$

where W_b is the neutral base width for the applied bias V_{BE}, $p_b(x)$ is the base doping, and D_{nb} is the minority electron diffusivity in the base. The intrinsic carrier density in the SiGe

HBT is given by

$$n_{ib}^2 = \gamma n_{io}^2 e^{\Delta E_{gb}^{app}/kT} e^{[\Delta E_{g,Ge}(grade)]x/(W_b kT)} e^{\Delta E_{g,Ge}(0)/kT} \tag{2}$$

where $\Delta E_{gb}^{app}/kT$ is the apparent bandgap narrowing due to heavy doping in the base and $\Delta E_{g,Ge}(grade)$ is defined as $\Delta E_{g,Ge}(W_b) - \Delta E_{g,Ge}(0)$. The low-doping intrinsic carrier density for Si is $n_{io}^2 = N_C N_V e^{-E_{go}/kT}$ and $\gamma = (N_C N_V)_{SiGe}/(N_C N_V)_{Si} < 1$ is the effective density-of-states ratio between SiGe and Si [11]. An expression for J_C in a SiGe HBT can be obtained by substituting Equation 2 into 1[12], [13]:

$$J_{C,SiGe} = \frac{qD_{nb}}{N_{ab}^- W_b} \left(e^{qV_{BE}/kT} - 1\right) n_{io}^2 e^{\Delta E_{gb}^{app}/kT} \left\{ \frac{\widetilde{\gamma}\widetilde{\eta} e^{\Delta E_{g,Ge}(0)/kT} \Delta E_{g,Ge}(grade)/kT}{1 - e^{-\Delta E_{g,Ge}(grade)/kT}} \right\} \tag{3}$$

where "$\sim$" denotes position-averaged quantities, N_{ab}^- is the ionized doping level in the base, and $\tilde{\eta} = \left(\widetilde{D_{nb}}\right)_{SiGe} / (D_{nb})_{Si} > 1$ is the minority electron diffusivity ratio between SiGe and Si. Note the first term in Equation 3 corresponds to the Si BJT and the second term represents the modification of J_C due to the Ge content in the base. Figure 6 depicts the Gummel characteristics for a typical SiGe HBT and a similarly constructed Si BJT. The SiGe HBT exhibits higher collector current and approximately the same base current as the Si BJT, as expected. The increase in J_C for the SiGe HBT in turn leads to an increase in current gain (β). The current gain ratio between a SiGe HBT and an identically constructed Si BJT can be expressed as:

$$\frac{\beta_{SiGe}}{\beta_{Si}} \cong \frac{J_{C,SiGe}}{J_{C,Si}} = \frac{\widetilde{\gamma}\widetilde{\eta} \Delta E_{g,Ge}(grade)/kT e^{\Delta E_{g,Ge}(0)/kT}}{1 - e^{-\Delta E_{g,Ge}(grade)/kT}} \tag{4}$$

The current gain depends linearly on the band offset due to Ge grading across the base and exponentially on the Ge induced band offset at the EB junction as Equation 4 indicates. Therefore, β is dependent on the Ge profile shape and can be modified for particular circuit applications. The introduction of Ge in the base in effect decouples β from the base doping. This fact implies that the base doping can be increased with out degrading β. Note that higher base doping reduces the base resistance, which has positive implications in terms of frequency response and broadband noise.

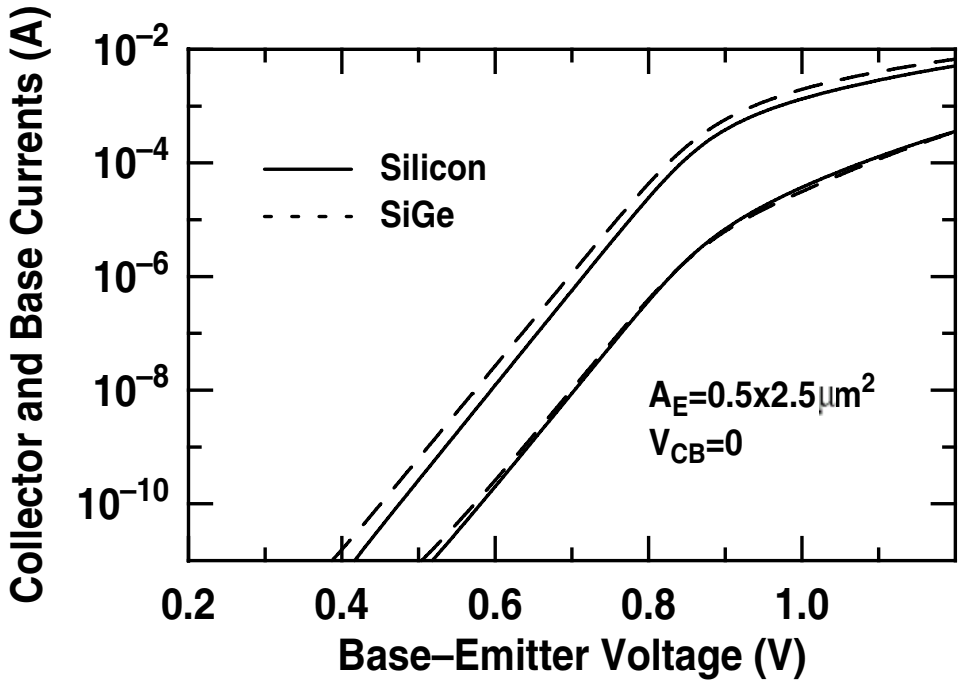

Figure 6: Representative Gummel plot for a SiGe HBT as compared to a Si BJT.

The output conductance is an important design parameter for analog circuits and is described by the Early voltage (V_A). A graded Ge profile in the base of the SiGe HBT leads to the enhancement of V_A compared to that of the Si BJT as shown below:

$$\frac{V_{A,SiGe}}{V_{A,Si}}\Big|_{V_{BE}} = e^{\Delta E_{g,Ge}(grade)/kT}\left[\frac{1-e^{-\Delta E_{g,Ge}(grade)/kT}}{\Delta E_{g,Ge}(grade)/kT}\right] \tag{5}$$

The Early voltage depends exponentially on the Ge grading across the base, which decouples V_A from the base doping and hence β. Consequently a high "current-gain–Early voltage product" (βV_A product), a figure-of-merit for analog applications, can be maintained independent of the base profile:

$$\frac{\beta V_{A,SiGe}}{\beta V_{A,Si}} = \widetilde{\gamma}\widetilde{\eta}e^{\Delta E_{g,Ge}(0)/kT}e^{\Delta E_{g,Ge}(grade)/kT}. \tag{6}$$

Note that the βV_A product for the SiGe HBT is enhanced over the Si BJT and is an exponential function of the band offset at the EB junction as well the Ge grading across the base.

Two important *ac* figures-of-merit are the unity-gain cutoff frequency (f_T) and the maximum oscillation frequency (f_{max}). Both parameters are positively impacted by the Ge content in the base as is shown below. The unity-gain cutoff frequency is given by:

$$f_T = \frac{1}{2\pi}\left[\frac{1}{g_m}(C_{eb}+C_{cb}) + \tau_b + \tau_e + \frac{W_{CB}}{2v_{sat}} + r_c C_{cb}\right]^{-1} \tag{7}$$

where g_m is the intrinsic transconductance, C_{eb} and C_{cb} are the EB and CB depletion capacitances, τ_b is the base transit time, τ_e is the emitter charge storage delay time, W_{CB} is the CB space-charge region width, v_{sat} is the saturation velocity, and r_c is the collector resistance. The grading of Ge across the base induces a built-in electric field in the neutral base region (directed from collector to emitter). This field accelerates the minority carriers across the base which effectively reduces the base transit time for the SiGe HBT:

$$\frac{\tau_{b,SiGe}}{\tau_{b,Si}} = \frac{2}{\widetilde{\eta}}\frac{kT}{\Delta E_{g,Ge}(grade)}\left\{1 - \frac{kT}{\Delta E_{g,Ge}(grade)}\left[1 - e^{-\Delta E_{g,Ge}(grade)/kT}\right]\right\}. \tag{8}$$

Due to the inverse relationship between the emitter charge storage delay time and *ac* β, τ_e is reduced for the SiGe HBT:

$$\frac{\tau_{e,SiGe}}{\tau_{e,Si}} \simeq \frac{J_{C,Si}}{J_{C,SiGe}} = \frac{1 - e^{-\Delta E_{g,Ge}(grade)/kT}}{\widetilde{\gamma}\widetilde{\eta}\frac{\Delta E_{g,Ge}(grade)}{kT}e^{\Delta E_{g,Ge}(0)/kT}}. \tag{9}$$

From Equation 7, it is clear that the reductions of both τ_b and τ_e will increase the f_T of the SiGe HBT over the Si BJT. The maximum oscillation frequency is given by:

$$f_{max} = \sqrt{\frac{f_T}{8\pi C_{bc} r_b}} \tag{10}$$

where r_b is the *ac* base resistance and C_{bc} is the base-collector capacitance. The increase in f_T as well as a reduction in r_b aid in improving the f_{max} of the SiGe HBT.

1.4 Summary

An overview of the SiGe HBT BiCMOS technology as well as the physics of operation are presented in this chapter. The SiGe HBT offers significant advantages over the Si BJT including increased β, V_A, f_T, and f_{max}. These performance enhancements coupled with

the integration with state-of-the-art CMOS make SiGe HBT BiCMOS technology a viable candidate for system-on-a-chip (SoC) integration.

Chapter II of this thesis describes some basic radiation concepts and nomenclature. An overview of the space radiation environment and the types of radiation present are discussed. This is followed by a description of the two major radiation damage mechanisms and their effects on Si semiconductor devices. In Chapter III, the effects of proton and gamma irradiation on SiGe HBTs is investigated. This chapter also examines the impact of substrate bias on proton damage in a 130 nm CMOS technology. Chapter IV investigates the effects of mechanical planar biaxial strain the on CMOS devices included in various Si/SiGe HBT BiCMOS technologies. Chapter V presents conclusions of the work reported in this thesis as well as suggestions for future directions for this research.

CHAPTER II

RADIATION CONCEPTS

2.1 Introduction

As we continue to explore the solar system, there is an increasing need for electronic systems that can withstand the harsh radiation conditions this environment presents. Predicting the exact radiation conditions the devices and circuits are exposed to is quite difficult. There are many factors to consider such as: the radiation environment, orbital path and altitude, and the length of the mission. Thus designers of space-born electronic systems must have a basic understanding of the radiation environment and its effects on devices and circuits. This chapter provides an overview of the space radiation environment, basic terminology, as well as radiation damage mechanisms and their effect on both bipolar and CMOS devices.

2.2 Space Radiation Environment

An overview of the space radiation environment is given in this section [14]. The space radiation environment is known to have a detrimental effect on semiconductor devices and materials. Radiation levels vary with changes in the solar magnetic field, which are attributed to long-term (22-year cycle) variations as well as storms such as solar flares and coronal mass ejections (CMEs). This solar activity is divided into two major cycles, the solar maximum and the solar minimum. The solar maximum is approximately a seven year period of high activity, while the solar minimum is about four years of relatively low activity. The solar wind and it's magnetic field interact with the Earth's magnetic field producing the radiation fields near Earth as seen in Figure 7.

Some charged particles in the solar wind are trapped by the Earth's magnetic field

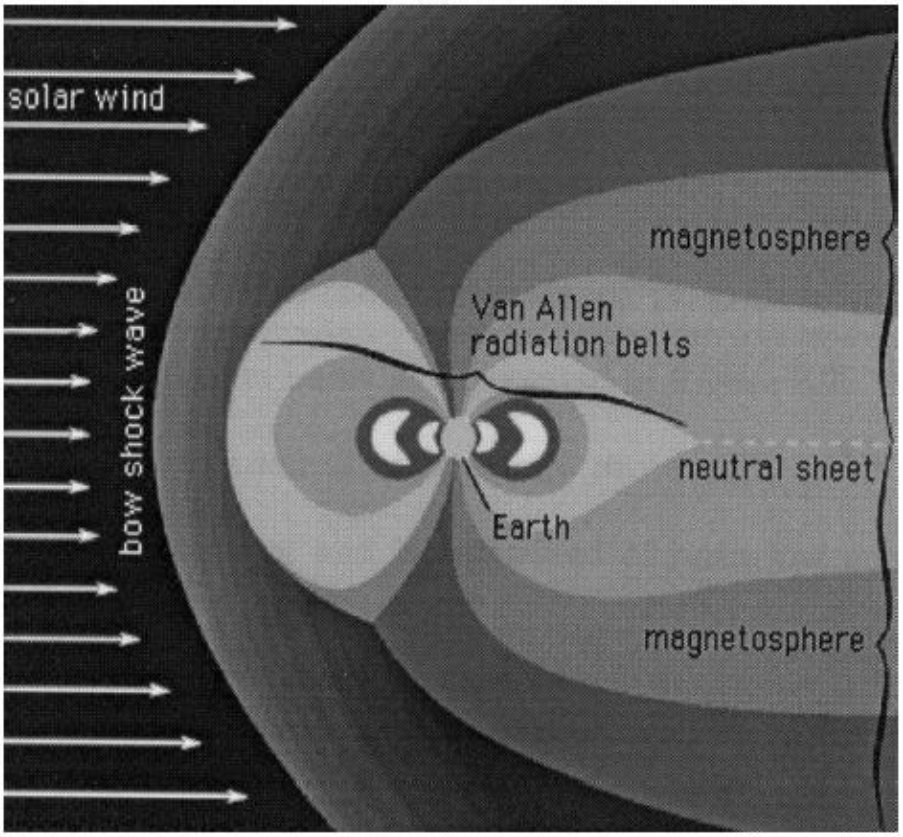

Figure 7: Illustration of the solar wind and radiation belts surrounding the Earth.

forming the Van Allen radiation belts. The Lorentz force acts on the trapped particles causing them move in a spiral around magnetic field lines and thereby restricts them to a defined area. The Lorentz force is given by:

$$F = q\,(\mathbf{E} + \mathbf{v} \times \mathbf{B}) \tag{11}$$

where q is the charge, $\mathbf{E}$ is the electric field, $\mathbf{v}$ is the velocity, and $\mathbf{B}$ is the magnetic field. Models indicate the Van Allen belts are toroidal in structure and consist mainly of trapped energetic protons and electrons. The lower altitude 'inner' belt is comprised mostly of protons ranging in energy from tens of keV to hundreds of MeV. Electrons up to a few MeV compose two higher altitude outer toroids. The particle population varies with the activity of the sun. During the solar maximum, electron population increases while proton population decreases. The particle fluxes in a given solar cycle are isotropic to first order. However, there is one known region over the Atlantic Ocean off the coast of South America where the offset of the Earth's geomagnetic axis from the earth rotation axis leads to increased particle flux at low altitudes (300- 500 km). This region is known as the South Atlantic Anomaly (SAA). The exposure levels a spacecraft may experience due to the trapped particles in the Van Allen belts depend on the altitude and inclination of orbit. It is known that the particle flux varies most for inclinations between $0^o < i < 30^o$ and altitudes in the range of 200 to 600 km.

Galactic cosmic ray particles also contribute to radiation in the space environment. The particles originate outside of the solar system and include all ions in the periodic table. The cosmic ray particles, composed of approximately 83% protons, 13% α-particles, 3% electrons, and 1% heavier nuclei, have low level fluxes and energies ranging from tens of MeV to hundreds of GeV. Due to the high energies, these particles primarily cause Single Event Effects (SEE). They are always present, but intensities reach a peak during the solar minimum and are lowest during the solar maximum. As in the case of trapped particles in the Van Allen belts, the exposure a spacecraft experiences depends on the inclination and altitude of orbit. In this case, particle flux variations are primarily dependent on inclination,

with altitude a secondary factor.

Solar events such as flares and CMEs produce energetic protons, alphas, heavy ions, and electrons that add to the space radiation environment. Solar events may last anywhere from several hours to a few days and engender particles with energies up to a few hundred MeV. Two categories of solar events are defined corresponding to two types of solar x-ray flares, gradual and impulse. Gradual events are characterized by an x-ray intensity decay over many hours and are coupled with CMEs, which produce large proton fluences. There is a sharp peak in x-ray emission, as well as an increase in heavy ions for impulse solar events. During solar maximum, there are approximately ten gradual events per year and about 1000 impulse events per year. Again, the radiation levels a spacecraft experiences depend primarily on the inclination and secondarily on the altitude of orbit.

2.3 Radiation Terminology

The amount of energy an energetic particle or photon deposits in a particular material is measured in units of *rad* ("radiation absorbed dose") where

$$1 \text{ rad} = 100 \text{ ergs/gram} = 6.24 \times 10^{13} \text{ eV/gram} \tag{12}$$

The SI unit for total ionizing dose is the gray (Gy) where

$$100 \text{ rad} = 1 \text{ Grey(Gy)} = 1 \text{ J/kg} \tag{13}$$

The rad is a material dependent property, as the energy absorbed depends on the density of the target material. Thus, when using the rad unit, the target material must also be specified. For Si based electronics, typical units are rad(Si) or rad(SiO_2), where 1.000 rad(SiO_2) = 0.945 rad(Si). The ionizing dose rate is given in rad per second. The particle flux is defined as the number of incident particles per unit area and time (particles/cm^2s). Particle fluence is the time integral of particle flux given in units of particles/cm^2.

2.4 Particle Categories

There are many particles present in the space environment. This section separates radiating particles into two categories, namely photons and charged particles. Characteristics and interaction mechanisms of the particles are examined [15], [16].

2.4.1 Photons

Photons, gamma, and x-rays have no mass or electric charge and are extremely penetrating. They interact with the target material via different mechanisms depending on the photon energy. The three interactions are the photoelectric effect, Compton scattering, and pair production with each one creating a energetic free electron. Figure 8 depicts the relative importance of the different photon interactions as a function of photon energy and the atomic number (Z) of the target material. The dashed line indicates Si (Z=14), the target material, in which the photoelectric effect dominates for photon energies below 50 keV, Compton scattering dominates for energies between 50 keV and 20 MeV, and pair production takes place for energies greater than 20 MeV.

As indicated by Figure 8, the photoelectric effect occurs for low energy photons. In this process the incident photon typically penetrates the inner most shell (K) of the target atom. The incident photon then transfers all its energy to the bound atomic electron, which causes it to be ejected from this shell. The electron is ejected with a kinetic energy given by:

$$E_{\text{kin}} = h\nu - B_{\text{e}} \tag{14}$$

where $h\nu$ is the incident photon energy and B_{e} is the electronic binding energy.

Compton scattering is dominant in Si for photon energies between 50 keV and 20 MeV. In this process, a photon collides with an atomic electron imparting an energy that is much greater than the binding energy of the electron. A portion of the incident photon energy is absorbed by the electron during collision, creating a Compton electron. The residual energy from this collision is deflected out from the original point of collision as lower energy

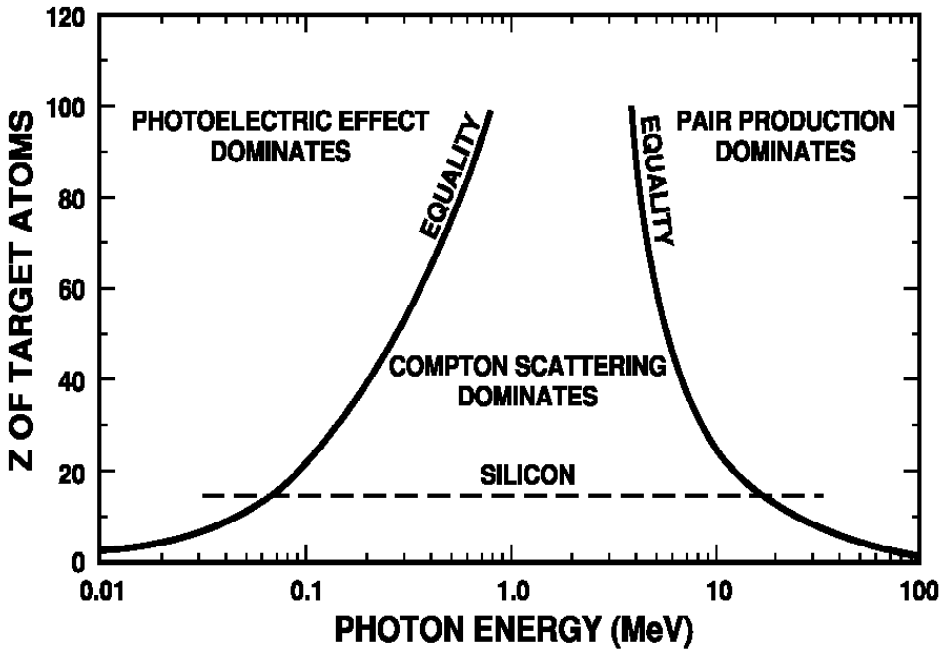

Figure 8: Importance of the different photon interactions as a function of photon energy and the atomic number (Z) of the target material (after [17]).

photon that goes on traveling through the target material. Note that Compton scattering is the dominant mechanism for ^{60}Co gamma radiation.

Pair production is the simultaneous creation of an electron-positron pair ($e^- + e^+$) as a result of a high energy photon (such as a gamma photon) coming under the influence of a strong nuclear electric field. The positron is the anti-matter counterpart of an electron having the same mass as an electron, but opposite charge. The threshold energy for pair production is 1.02 MeV. If the incident photon energy is greater than the threshold, the remaining energy appears as kinetic energy in the electron-positron pair.

2.4.2 Heavy Charged Particles

Heavy charged particles, such as protons, alphas, and other heavy ions are far less penetrating than photons. They interact with matter primarily through Rutherford (or Coulomb) scattering and also through nuclear interactions for high energy particles. The incident

particle ionizes and/or excites atomic electrons through Rutherford scattering. Atomic displacement can also occur by Rutherford scattering if enough energy is transferred to the atom. The nuclear interactions that a heavy charged particle and the target material may experience involve elastic scattering, inelastic scattering, and transmutation. During scattering, the incident particle yields some of its energy to a target atom and displaces the atom from its lattice position. The displaced atom is referred to as the primary knock-on, which in-turn loses energy to ionization and can displace other lattice atoms. Elastic scattering is said to have occurred when the energy given up by the particle is greater than the energy necessary for displacement. In the inelastic scattering process, the target atom captures the incident particle and then emits the particle at a lower energy. The target atom is in an excited state due to this energy loss. The atom returns to it original state by emitting a gamma-ray. Inelastic collisions can also bring about atomic displacement. In transmutation, the target atom captures the incident particle and emits a different particle, consequently converting the atom from one element to another.

2.5 Radiation Damage Mechanisms

There are two main radiation damage mechanisms that occur in spaceborne electronic systems: ionization damage and displacement damage. Ionization damage can be divided into two categories: total ionizing dose (TID) and Single Event Effects (SEE). The concentration of this work is on TID and displacement damage, thus SEE will not be discussed here. TID ionization and displacement damage are examined in this section [3], [15], [16], [18].

2.5.1 Ionization Damage

Ionization damage results from the generation of electron-hole pairs in the material. The incident energetic particle loses energy as it passes through the material, creating electron-hole pairs along its path. The amount of energy transferred to ionization is determined by the particle's Linear Energy Transfer (LET) function, which is the energy transferred

per unit of path traveled by the ionizing particle normalized by the density of the target material. The LET function is given by:

$$LET = \rho_m^{-1} dE/dx \tag{15}$$

where

$$\frac{-dE}{dx} = 2Pq^4 Z_1^2 Z_2 N_{at} \frac{M_2}{m} \frac{1}{E} \ln\left(\frac{4E}{E_{eh}}\right) \tag{16}$$

and q is the absolute value of the electron charge, P is the stopping number of the material, Z_1 and Z_2 are the atomic charges of the incident particle and the target material respectively, N_{at} is the atomic density of the target material, M_2 is the atomic mass of the target material, m is the mass of the incident particles, E is the energy of the incident particles, and E_{eh} is the mean ionization energy. The units are MeV-cm^2/mg. The LET of the particle is a function of the energy, mass, and charge of the particle as well as the mass of the target material.

Ionization damage is generally due to protons, electrons, gammas, and x-rays. The most common degradation effect of ionizing radiation is charge trapping by pre-existing or radiation-induced traps. For semiconductor devices, ionization damage is typically associated with the surface of a device and occurs primarily in isolating oxides and in oxide-semiconductor interfaces. The charge trapping in the oxide leads to the formation of generation/recombination centers.

2.5.2 Displacement Damage

Particles such as alphas, protons, electrons, and neutrons can cause displacement damage. Incident photons can also produce displacement damage (to a lesser extent) via the Compton Effect. Displacement damage occurs when nuclear collisions between the incident particle and the atom leads to displacement of the atom from its original lattice position. If the atom is displaced to a nonlattice position, the resulting defect is called an interstitial and its former position is referred to as a vacancy. Together the vacancy and interstitial are called a Frenkel pair. If a significant amount of kinetic energy is transferred in the collision,

the primary knock-on can displace other atoms forming a defect cluster. The amount of energy given up to atomic displacements per unit path length is expressed by the particle's Non-Ionizing Energy Loss (NIEL). This is equivalent to the LET for ionization damage and hence has the same units of MeV-cm^2/mg. The particle NIEL can be calculated based on differential cross sections and particle-atom interaction kinematics:

$$NIEL = \frac{N}{A} \int L[T(\Theta)] T(\Theta) \left\{ \frac{d\sigma}{d\Omega} \right\} d\Omega \tag{17}$$

where N is Avogadro's number, A is the gram atomic weight of the target material (Si), $d\sigma/d\Omega$ is the differential cross section for recoil in direction Θ, $T(\Theta)$ is the recoil energy, and $L[T(\Theta)]$ is the fraction of the recoil energy that goes into displacements[19].

In semiconductor device, defects due to displaced atoms give rise to new energy levels in the bandgap, which in turn change the electrical properties of the device. These radiation-induced defects yield several processes that alter material and device properties described as follows. The first process is thermal generation of electron-hole pairs through radiation-induced defect levels near midgap, which is significant in the depletion region of devices. The presence of the defects leads to an increase in the thermal generation rate, which in turn causes an increase in leakage current for silicon devices. The second process is the recombination of electron-hole pairs. Carrier lifetime is decreased due to the radiation-induced recombination centers. The third process involves the trapping of carriers at defect centers, which leads to increasing the transfer inefficiency in charge-couple devices. The fourth process is the compensation of donors and acceptors by defect centers. This brings about a decrease in the equilibrium majority carrier concentration, which will affect all device and circuit parameters that depend on the carrier concentration. The fifth process, trap-assisted tunneling via radiation-induced defects, can lead to device current increases under certain conditions. The sixth process occurs when defects act as scattering centers, causing a reduction in carrier mobility. The seventh effect is carrier type conversion due to the reduction in carrier concentration as previously discussed. Finally, the eighth effect is enhanced effectiveness for thermal generation of carriers. This effect arises when the

radiation-induced defects are located in a high field region of the device.

2.6 Radiation Effects on Si-based Semiconductor Devices

Radiation damage affects the performance of various semiconductor devices in different ways. This is due to differences in device operation and fabrication. The effects of radiation damage on both Si bipolar transistors and CMOS devices are reviewed in this section [3], [15], [16].

2.6.1 Radiation Effects on Bipolar Devices

Bipolar device performance is affected by both ionization and displacement damage. The classic signature of radiation damage in bipolar transistors is an increase in the base current and hence a decrease in current gain.

As mentioned above, ionization damage leads to trapped charge in the isolating oxides and oxide - semiconductor (Si) interfaces. In a *npn* bipolar device, the trapped oxide charge alters the surface potential at the spacer oxide and base-emitter junction interface. Subsequently, the Si p-type base region is depleted and causes an increase in the base current (I_B). The increase in I_B leads to a degradation in the current gain ($\beta = I_C/I_B$), where I_C is the collector current. The p-type surface layer could also become inverted depending on the doping density and amount of trapped hole charge. If inversion occurs, an increase in the leakage current along the field oxide is possible. Surface recombination in the base-emitter depletion region is coupled with the density of radiation-induced interface traps. An increase in the number of interface traps also enhances the surface recombination velocity (s_r). The increase in s_r corresponds to an increase in the recombination base current and hence a decrease in current gain.

The primary consequence of displacement damage in Si bipolar devices is current gain degradation. This occurs because radiation-induced recombination centers produce a reduction in minority carrier lifetime. It is know that over a large range of displacement

damage, the reciprocal current gain increases with particle fluence. A displacement damage factor can be calculated using the Messenger-Spartt equation at fixed V_{BE} [19]:

$$\frac{1}{\beta(\phi)} = \frac{1}{\beta(0)} + K(E)\phi \tag{18}$$

where $\beta(0)$ is the pre-radiation current gain, $K(E)$ is the damage factor, and ϕ is the particle fluence.

Generation centers due to displacement can increase the leakage current in the reverse-biased base-collector junction. Note that narrow base widths and high base doping can significantly reduce the effects of displacement damage.

2.6.2 Radiation Effects on CMOS Devices

CMOS devices are majority carrier devices and displacement damage is not a concern unless the incident particles are extremely energetic and cause type conversion. Ionization damage produces trapped charge in the gate oxide as well as in the field and isolation oxides. Figure 9 illustrates the effects of ionizing radiation on oxides. Radiation-induced charge trapped in the gate oxide causes a shift in the flat-band voltage (ΔV_B), which corresponds to a threshold voltage shift due to trapped oxide charge. The ΔV_B is proportional to the square of the oxide thickness. The trapped oxide charge also leads to a degradation in transconductance (g_m). Interface traps, when charged, contribute to the radiation-induced threshold voltage shift. Coulombic scattering at the charged oxide and interface traps leads to a reduction in low-field mobility. The amount of radiation-induced trapped charge in the gate oxide decreases with the oxide thickness. Similar trends have been observed for the generation of interface traps. In today's scaled submicron CMOS, the gate oxides are very thin (few nm) and essentially no net charges are trapped. Therefore, there is negligible change in threshold voltage, g_m, and low-field mobility in devices with very thin oxides.

The ionizing radiation degradation in scaled submicron CMOS is primarily due to trapped charges in the field and isolation oxides since they are much thicker than the gate

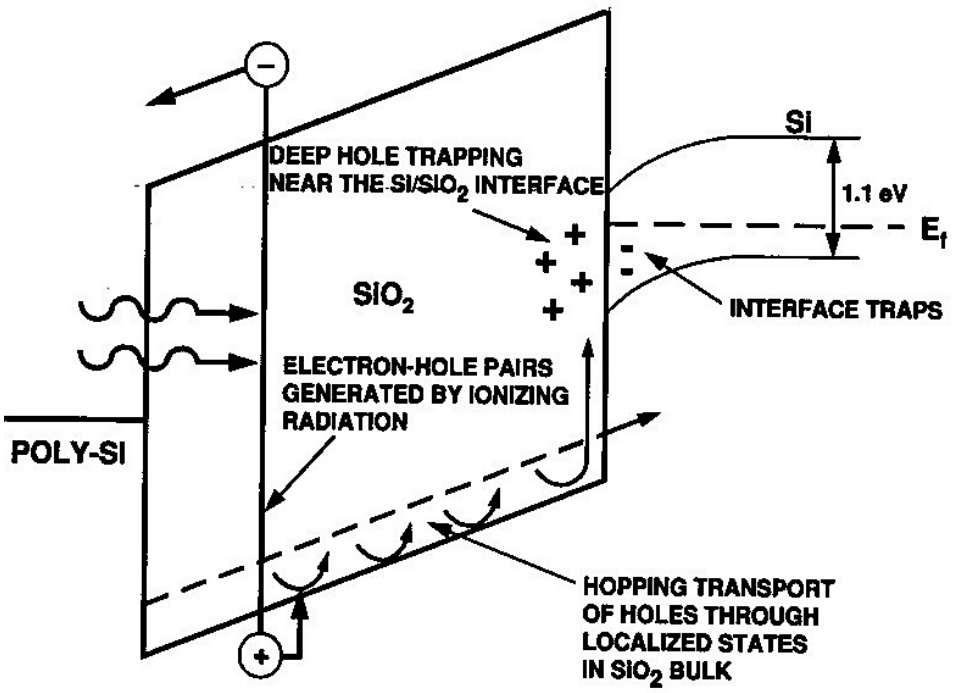

Figure 9: Ionizing radiation effects on oxides.

oxide. These charges degrade the subthreshold conduction leading to high off-state leakage. Most commercial submicron technologies use Shallow Trench Isolation (STI). There are two common leakage paths in the STI. The first path is along the sidewalls of a device which produces an increase in subthreshold leakage. The second path is in between devices causing the parasitic field transistor to turn on.

2.7 Summary

The radiation response of a semiconductor device depends on the radiation environment and the type of radiation, as well as the operation and fabrication processes of the particular device. Ionizing radiation affects the performance of both bipolar and CMOS devices, while displacement damage is typically only an issue for bipolar devices. The next chapter presents experimental results on the proton and gamma radiation tolerance on SiGe HBTs as well as the effects of proton radiation on scaled CMOS.

CHAPTER III

RADIATION EFFECTS IN SIGE HBT BICMOS TECHNOLOGIES

3.1 Introduction

The semiconductor industry is continuously striving for faster, smaller, and cheaper integrated circuits (ICs). These trends are also emerging as the driving force for the space community. The use of commercial-off-the-shelf (COTS) parts and system-on-a-chip (SoC) integration are the two major steps the space community is employing to reach the goal of faster, smaller, and cheaper parts. The use of COTS parts saves a considerable amount of money previously spent on radiation-hardening techniques. SoC integrates digital, RF, and analog blocks on the same chip, thus reducing system costs. This integration scheme also reduces the weight and size of the system. As Chapter I indicates, SiGe BiCMOS technology is a viable candidate for SoC integration and the present chapter discusses the radiation response of this technology.

First, the effects of gamma and proton radiation on SiGe HBTs is presented. Proton radiation effects on SiGe HBTs were recently reported for three different commercially available SiGe HBT BiCMOS technologies [3], [20], [21]. The present work investigates both the proton and gamma radiation response of the National BiCMOS8 SiGe HBT process technology, a new commercial offering. This work presents both gamma and proton data for a representative SiGe HBT device, as well as the effects of protons on a differential LC RF oscillator fabricated on a pre-production hardware lot of the same process technology with identical device dimensions. Finally, we compare proton radiation results in this work with those reported previously for other SiGe technologies.

Next, the effects of proton irradiation on the *dc* and *ac* properties of 130 nm Si CMOS technology are investigated. It is well known that the tolerance to ionizing radiation generally improves with CMOS technology scaling, due to the natural thinning of the gate oxide and shallow trench isolation. Circuit designers are increasingly taking advantage of the effects of both static and dynamic body (substrate) biasing to improve circuit performance (analog circuits) and reduce power dissipation (digital circuits) [22]-[24]. A reverse body bias is known to increase the threshold voltage and reduce the off-state leakage current, for instance, which is of great interest from a radiation perspective in many spaceborne circuits. This work reports for the first time the results of proton radiation on 130 nm Si CMOS technology (having an effective minimum gate length of 0.12μm) for two different irradiation substrate bias conditions. The nFETs investigated are part of a fully-integrated, third generation, 200 GHz SiGe HBT BiCMOS technology (IBM SiGe 8HP) [9]. Two types of Si CMOS devices are available in this technology (1.2V and 2.5V), with minimum channel lengths of 0.12 μm and 0.24 μm, respectively. The technology was not intentionally radiation-hardened in any way. We also compare the proton radiation tolerance observed on this 130 nm CMOS node (IBM SiGe 8HP) with those previously reported for a 180 nm CMOS node (IBM SiGe 7HP).

3.2 Proton and Gamma Radiation Effects in SiGe HBTs

The SiGe BiCMOS wafers were diced, mounted, and subsequently wirebonded in 28-pin dual inline packages (DIP). Several standard *npn* SiGe HBTs of various emitter geometries (A_E) were investigated. A device with A_E of 0.4×1.4 μm^2 is used here to investigate the effects of proton and gamma irradiation. The proton tolerance of a fully-integrated SiGe LC tank oscillator circuit is also investigated.

The 63.3MeV proton irradiation was performed at the Crocker Nuclear Laboratory at

the University of California at Davis. The dosimetry measurements used a five-foil secondary emission monitor calibrated against a Faraday cup. The radiation source (Ta scattering foils) located several meters upstream of the target establish a beam spatial uniformity of about 15% over a 2.0 cm radius circular area. Beam currents from about 20 nA to 100 nA allow testing with proton fluxes from 1.0×10^9 to 1.0×10^{12} proton/cm^{2}sec. The dosimetry system has been previously described [25], [26], and is accurate to about 10%. The SiGe HBT *dc* test structures were irradiated with all terminals grounded with proton fluences ranging from 1.0×10^{12} to 5.0×10^{13} p/cm^2 (equivalent gamma doses of 135 and 6,759 krad(Si), respectively). The *ac* test structures and circuits were irradiated with all terminals floating at a proton fluence of 5.0×10^{13} p/cm^2.

Gamma irradiation was performed using a J.L. Shepard Model 81 Co-60 source at Goddard Space Flight Center Radiation Effects Facility (GSFC REF). Dose rates varied from 20.5 to about 29.1 rad(Si)/sec. The dose was uniform to within 10% across all test samples, as determined using an ion chamber probe. In accordance with MIL-STD 883 Method 1019.6, a Pb/Al box was used to decrease the flux of secondary gammas and ensure a monochromatic gamma ray spectrum. The SiGe HBT *dc* test structures were irradiated with all terminals terminated inside black conductive foam, with gamma total doses ranging from 92 krad(Si) to 3,792 krad(Si). The *ac* test structures were also irradiated with all terminals floating at a gamma dose of 3,792 krad(Si).

Previous reports indicate that irradiations performed with all terminals grounded demonstrate similar results to irradiations with all terminals floating, and should be considered worst case [27]. Wirebonding of *ac* test structures and circuits is not compatible with robust broadband measurements, and hence on-wafer probing of S-parameters was used to characterize the high-frequency performance. All samples were measured at room temperature. The wirebonded *dc* test structures were measured after each dose step using an Agilent 4155 Semiconductor Parameter Analyzer. The *ac* measurements were made post

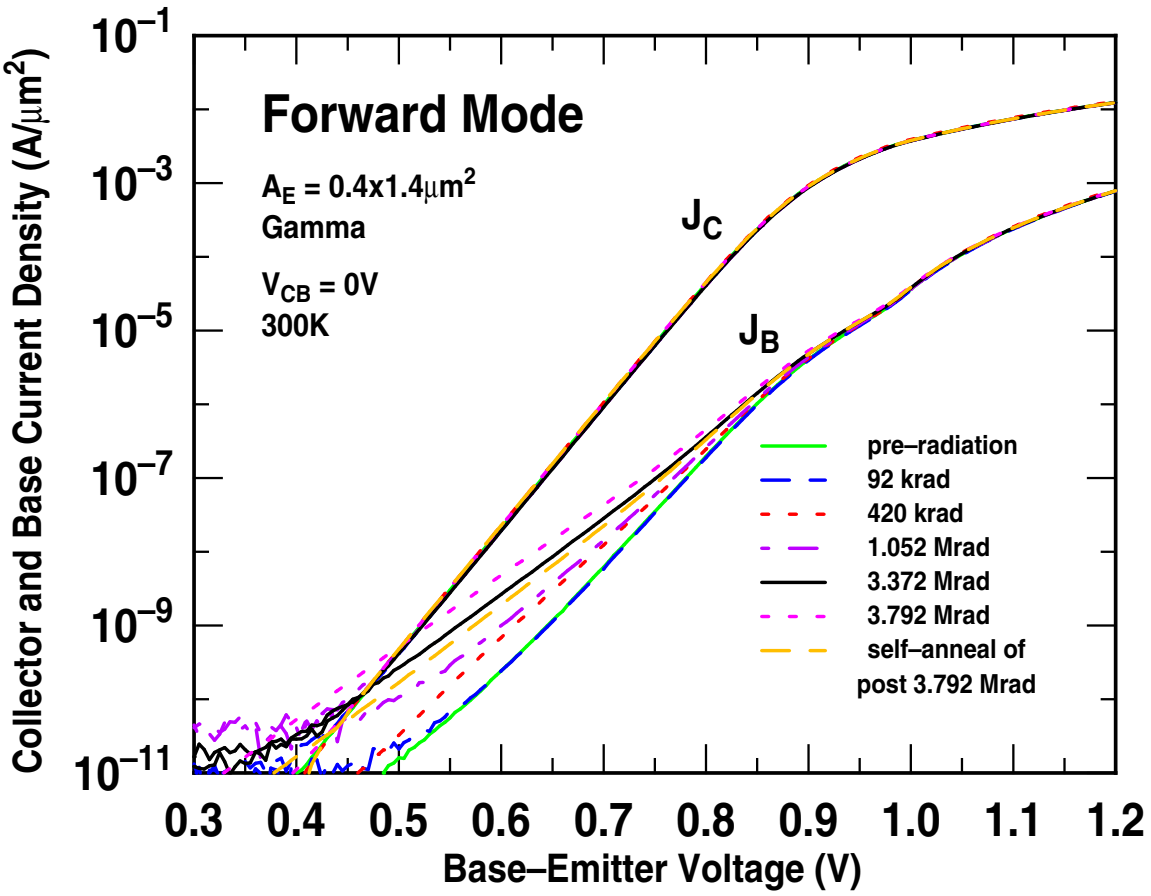

Figure 10: Forward-mode Gummel characteristics as a function of gamma dose.

radiation with an Agilent 8510C Vector Network Analyzer (*ac*) using the techniques discussed in [28]. The LC oscillator circuit was measured using an Agilent 8563 spectrum analyzer with phase noise module.

3.2.1 *dc* Results

Representative forward-mode Gummel characteristics for SiGe HBTs subjected to gamma and proton irradiation are shown in Figures 10 and 11, respectively. These plots illustrate the radiation induced damage in the emitter-base (EB) junction of the device. There is an observed increase in base current with both proton fluence and gamma dose, which is indicative of radiation-induced damage in SiGe HBTs [3]. This increase is due to radiation engendered generation/recombination (G/R) trap centers located around the periphery

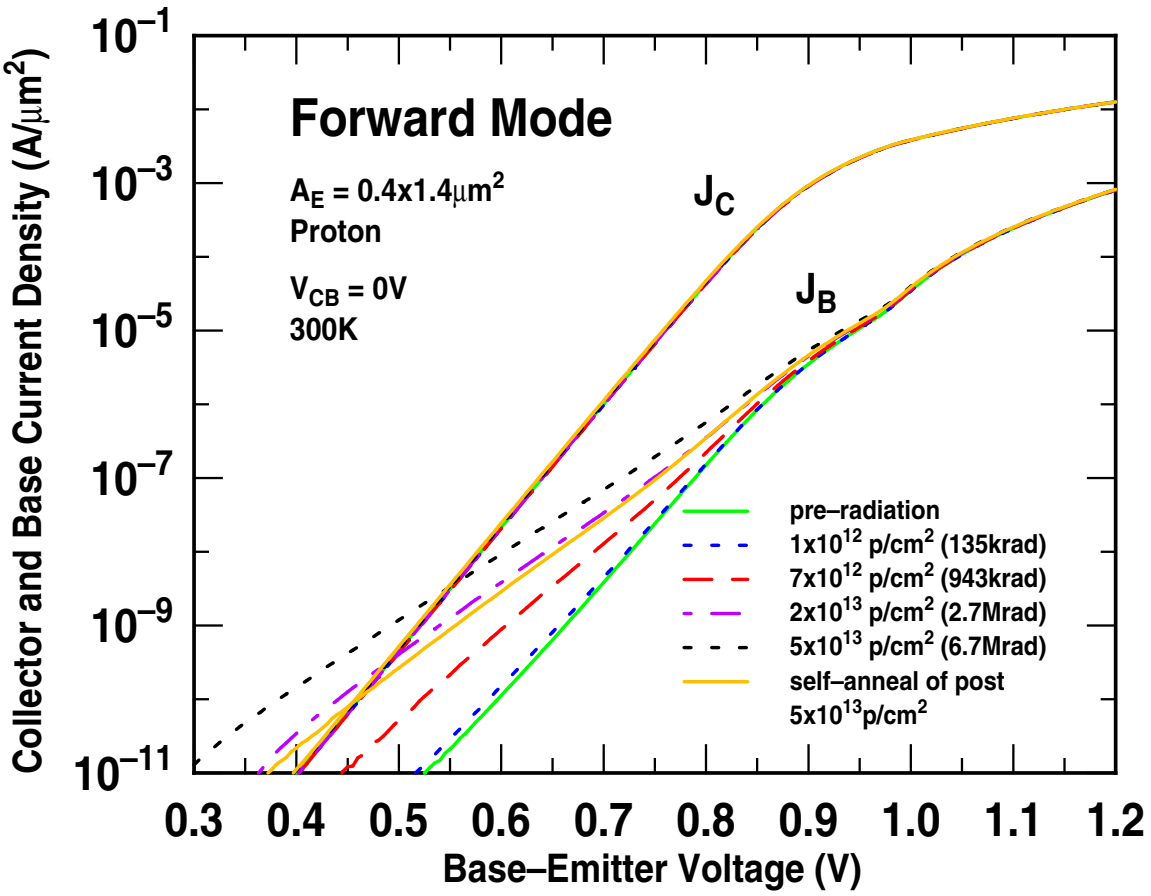

Figure 11: Forward-mode Gummel characteristics as a function of proton fluence.

of the EB spacer oxide [29]. The inverse-mode (a switch of the emitter and collector terminals) Gummel characteristics are used to assess the radiation damage of the physical collector-base (CB) junction. The inverse-mode Gummel characteristics for gamma and proton irradiation are shown in Figures 12 and 13, respectively. It appears that there is significantly more radiation induced degradation at the CB junction as compared to the EB junction for gamma radiation. However, Figure 13 indicates there is slightly less degradation at the CB junction as compared to the EB junction for proton radiation in this technology. The radiation induced traps are believed to be physically located along the shallow trench isolation (STI) edge [3].

The forward-mode base-current increase, for both gamma and proton irradiation, also leads to a degradation in current gain (β) and a shift in peak β as seen in Figures 14 and 15,

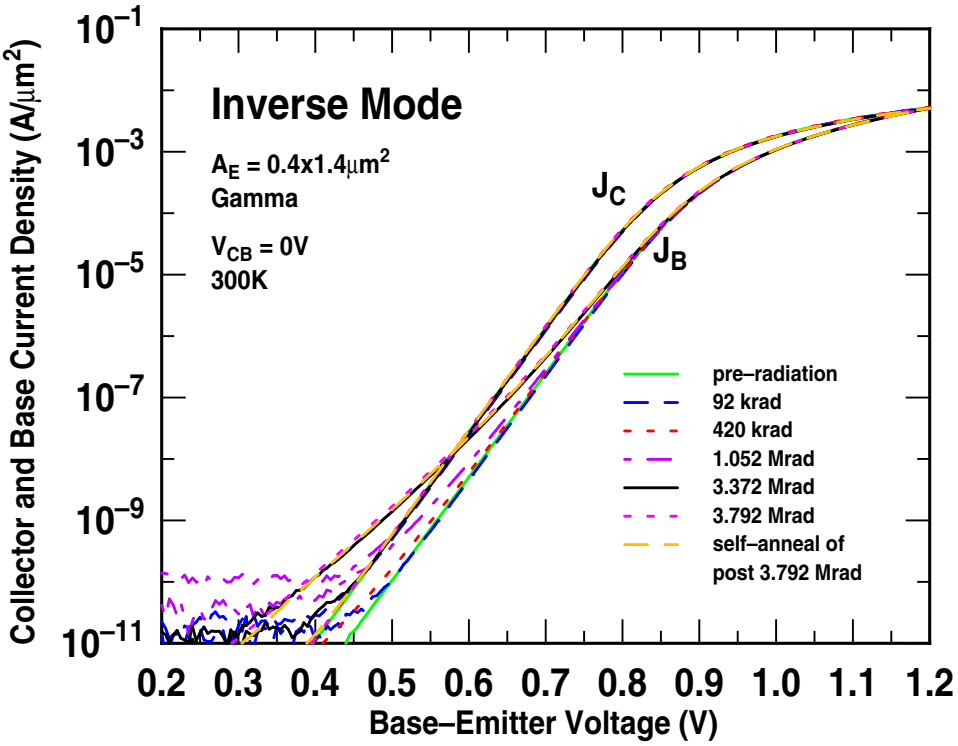

Figure 12: Inverse-mode Gummel characteristics as a function of gamma dose.

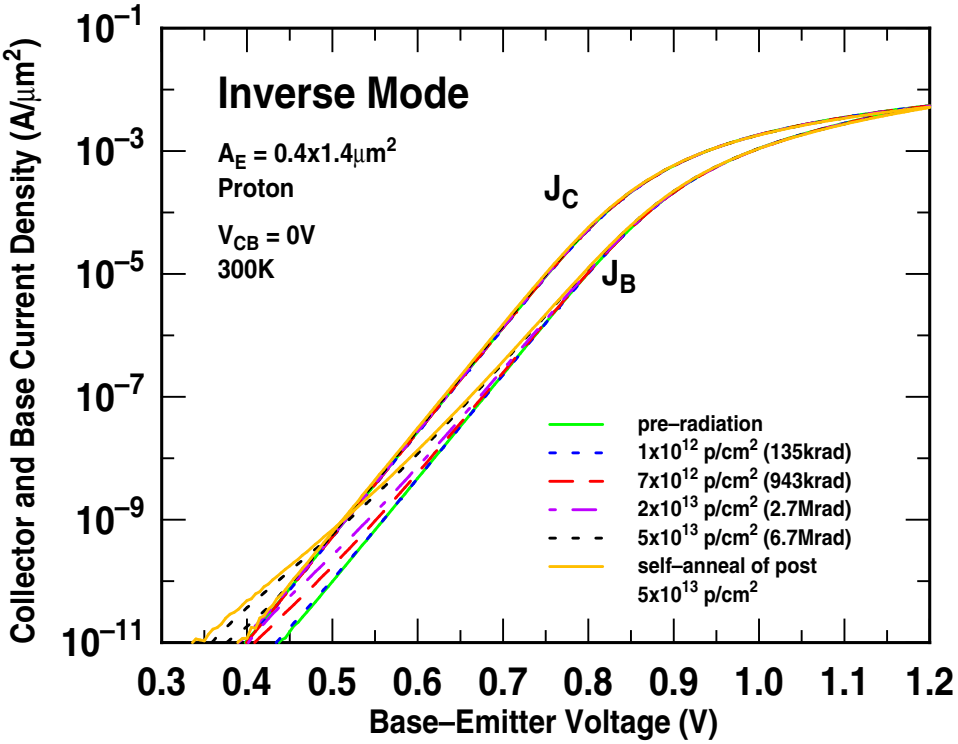

Figure 13: Inverse-mode Gummel characteristics as a function of proton fluence.

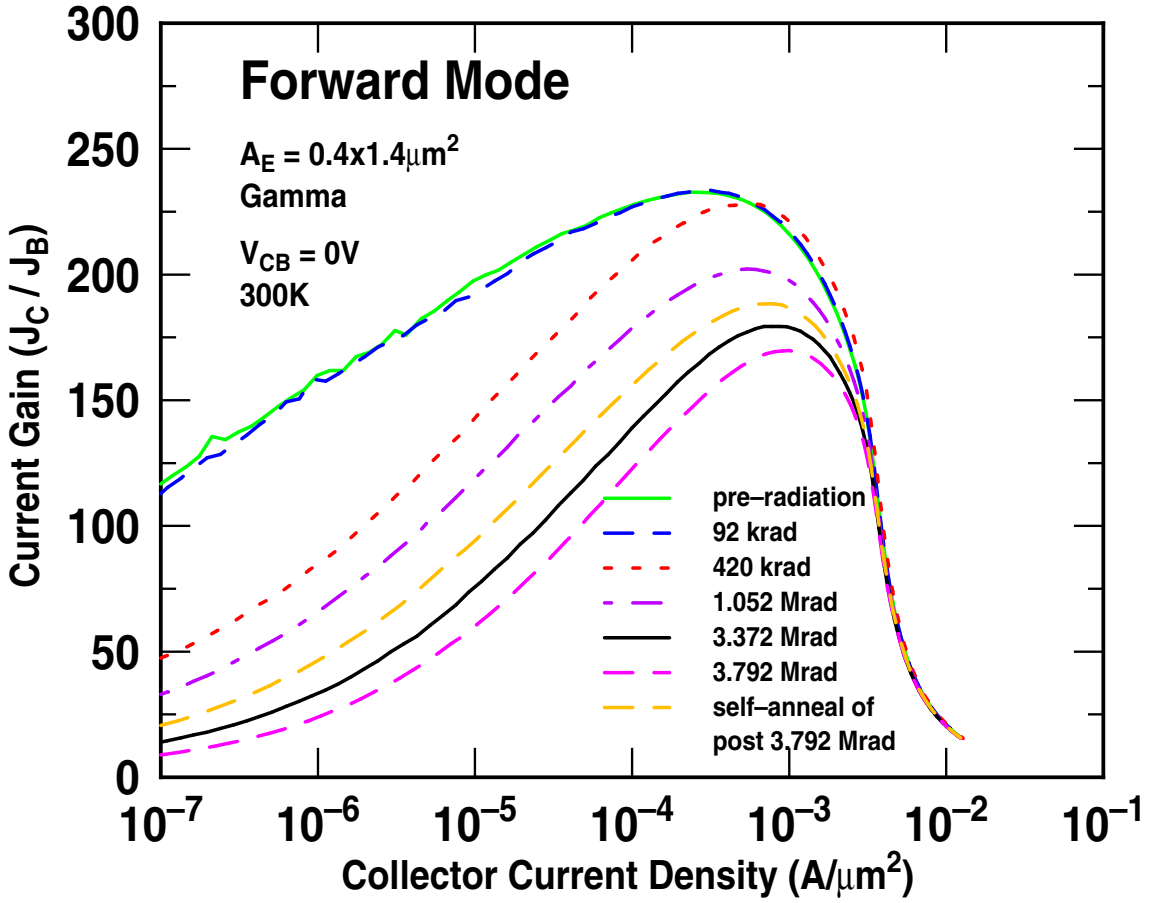

Figure 14: Current gain as a function of gamma dose.

respectively. The significant decrease occurs at low collector current density (J_C), as expected. In fact there is negligible change in the post-radiation β at peak cutoff frequency (a collector current density of approximately 2 mA/μm^2), which is good news for circuits that typically are biased at or near this operating point.

3.2.2 Proton versus Gamma

The effects of proton and gamma irradiation on this National BiCMOS8 SiGe technology are quantitatively compared in this section. Proton radiation generates more forward-mode excess base-current (ΔI_B) than gamma radiation, especially at fixed equivalent gamma

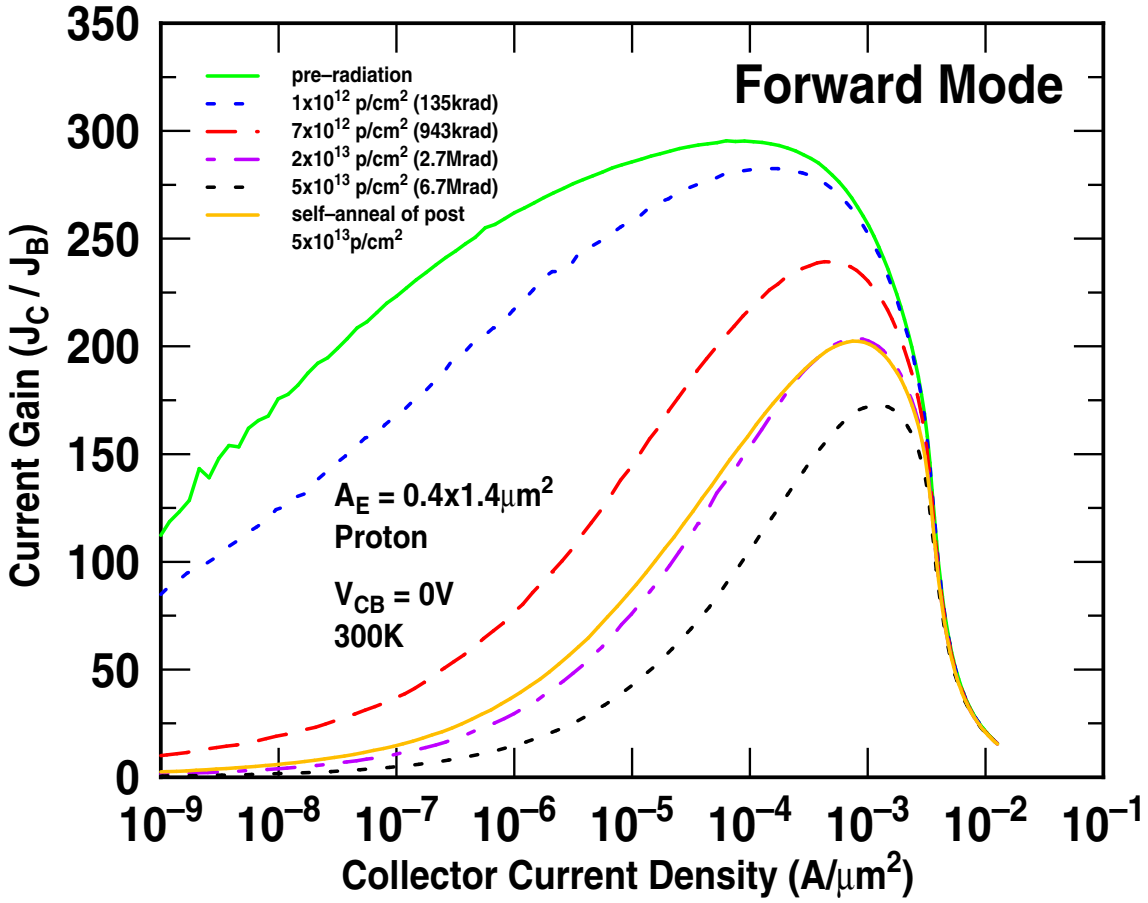

Figure 15: Current gain as a function of proton fluence.

doses below 1Mrad, as evidenced in Figure 16. This is indicative of the fact protons induce both displacement and ionization damage, while gamma rays produce very little displacement damage. We expect to see the same result for the inverse-mode of operation. However, a look at the inverse-mode excess base-current (Figure 17) indicates gamma rays induce much more radiation damage than protons along the STI edge of the device. This unexpected result was also observed in other SiGe technologies [30]. It is possible the anomalous result is a dose rate effect. The gamma dose rate varied from 20.5 to about 29.1 rad(Si)/sec, while the proton dose rate was much higher at approximately 1000 rad(Si)/sec. Further investigations are planned to aid in determining the exact cause of this unexpected result. The larger proton ΔI_B is again manifested in the forward-mode β degradation as shown in Figure 18.

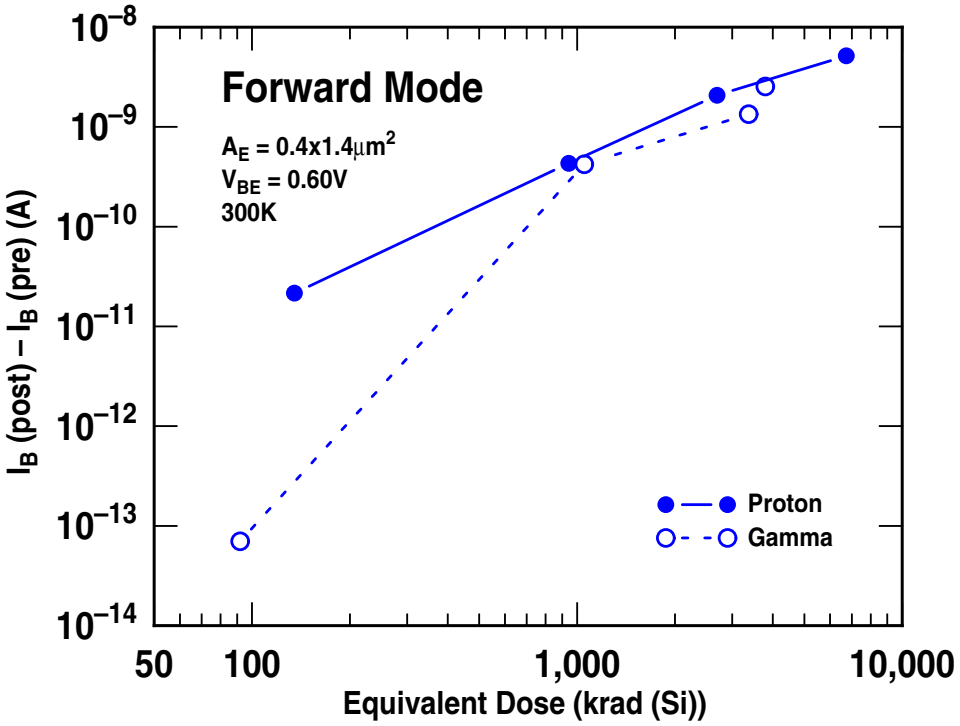

Figure 16: Forward-mode excess base current as a function of equivalent dose for both proton and gamma radiation.

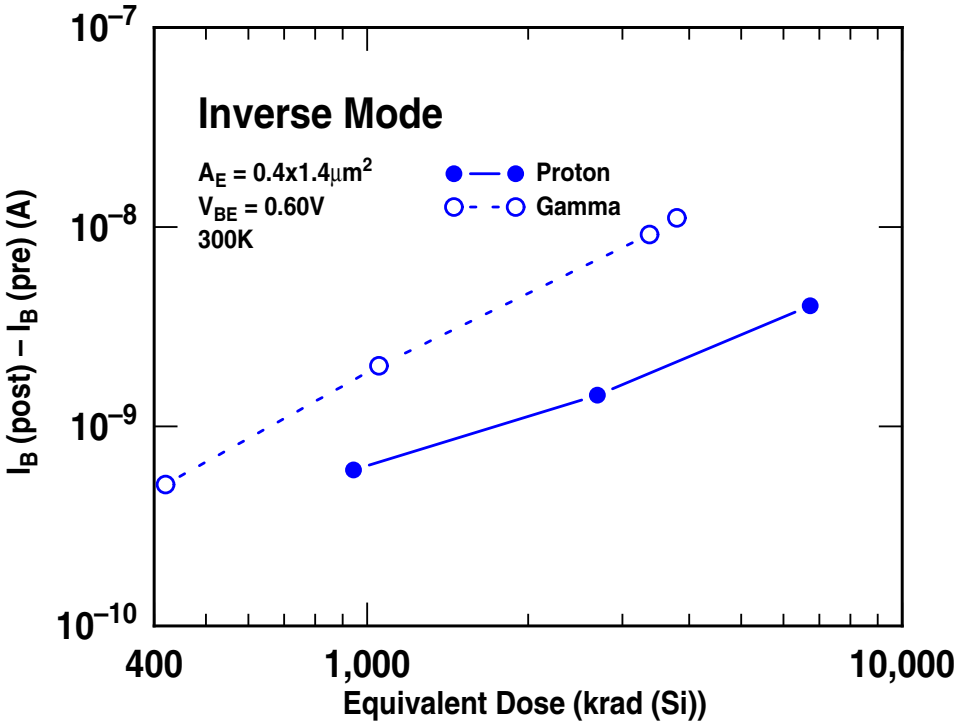

Figure 17: Inverse-mode excess base current as a function of equivalent dose for both proton and gamma radiation.

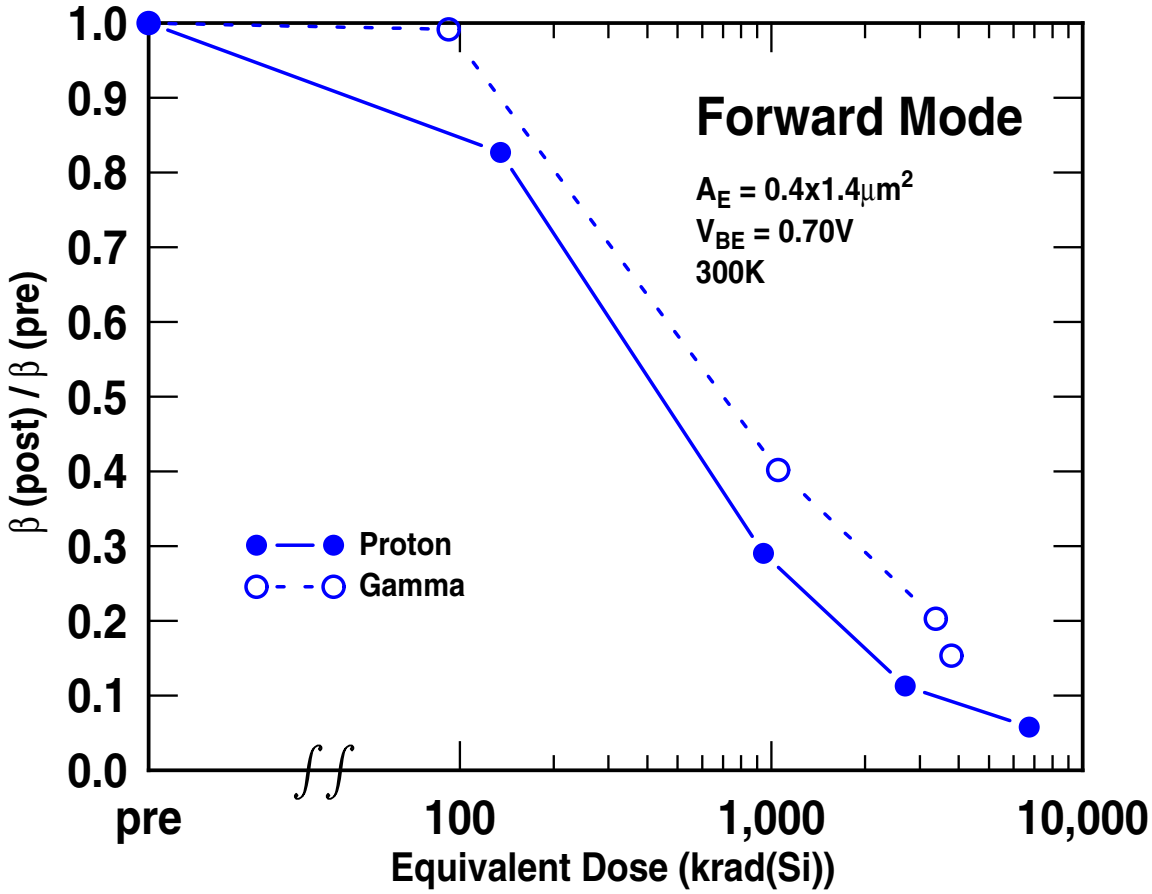

Figure 18: Normalized current gain as a function of equivalent dose for proton and gamma radiation.

The devices were re-measured five and eleven weeks after proton exposure and 11 and 18 weeks after gamma exposure. Figure 19 shows the normalized forward- and inverse-mode excess base current density as a function of time after final exposure. A reduction in forward-mode base current was observed for both gamma and proton irradiation. This suggests there is a self-annealing process that reduces the number of G/R trap centers in the emitter-base spacer oxide. Interestingly, very little annealing was observed for inverse-mode gamma radiation, while the proton radiation inverse-mode base current actually increased with time after exposure. These observations indicate that there is a fundamental difference between the radiation-induced G/R mechanisms in the emitter-base spacer oxide and the STI. The inverse-mode annealing results are different from those observed in other

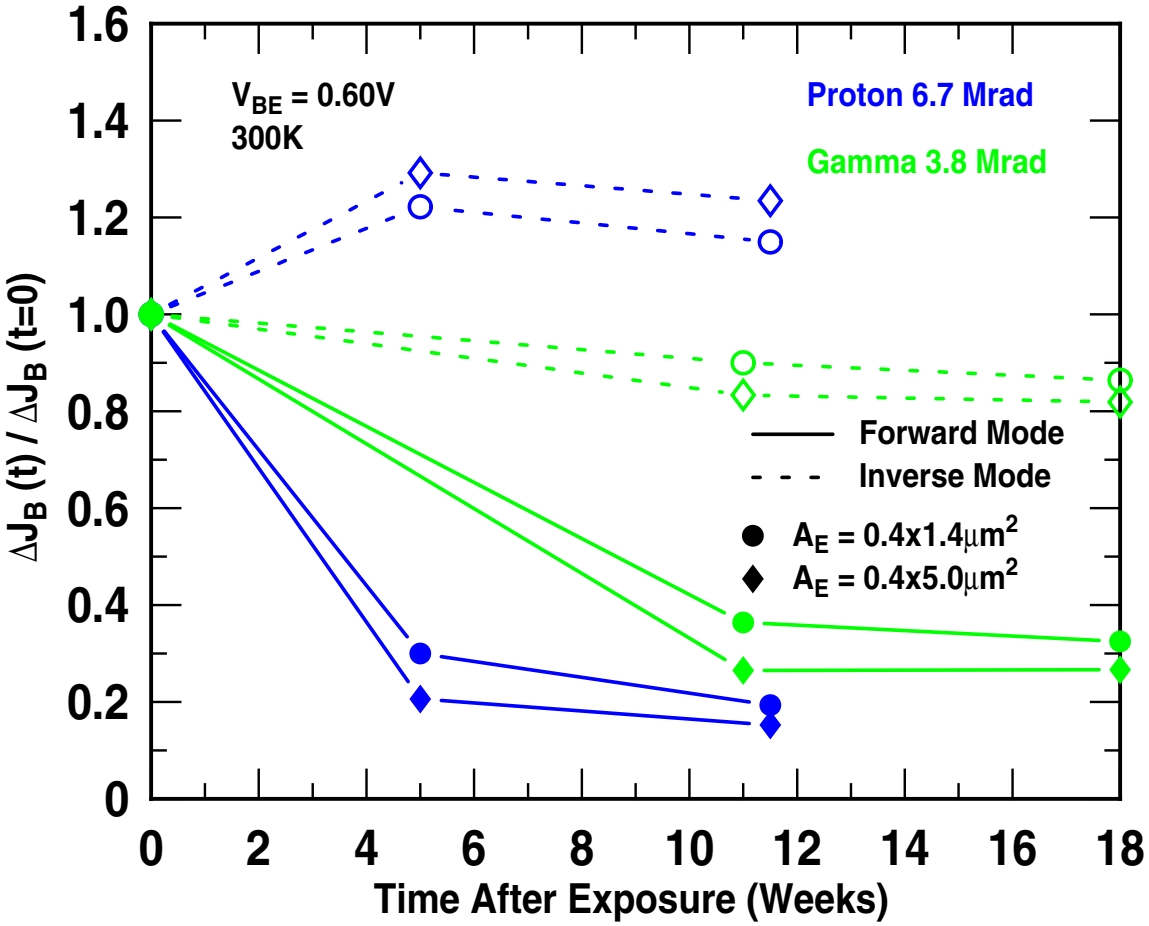

Figure 19: Normalized forward- and inverse-mode excess base current density as a function of time after exposure.

SiGe technologies.

The National BiCMOS8 SiGe technology is reasonably tolerant to both proton and gamma radiation (up to Mrad-level equivalent dose), without any intentional radiation hardening, as indicated by the above results.

3.2.3 *ac* Results

The scattering parameters (S-parameters) were characterized up to 48 GHz over a wide span of bias currents at a fixed collector-base voltage (V_{CB}). A standard "open" structure was used to de-embed the data to facilitate the calculation of the small-signal current gain (h_{21}) and the Maximum Unilateral Gain (U). The unity gain cutoff frequency (f_T) and the

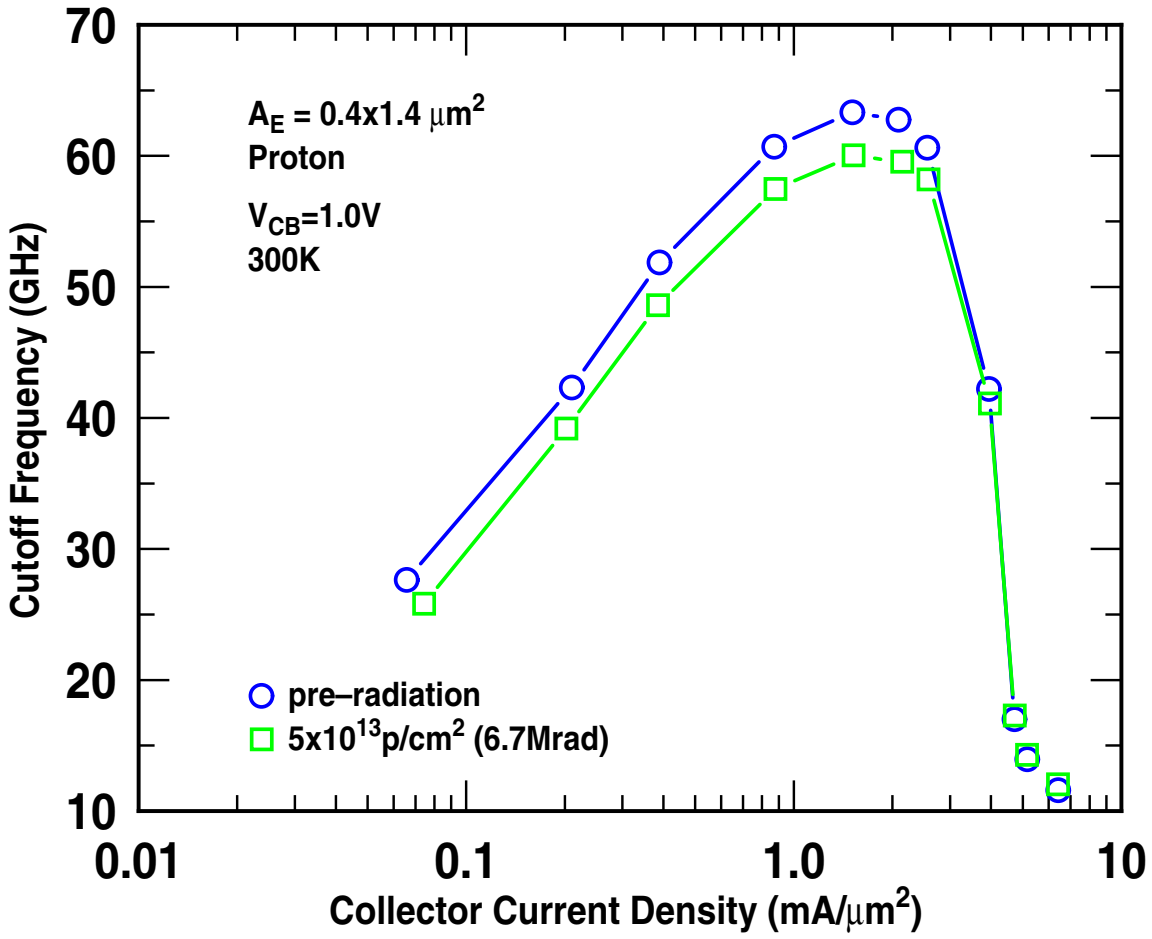

Figure 20: f_T on J_C as a function of proton fluence.

maximum oscillation frequency (f_{max}) were determined by extrapolating a -20 dB/decade slope from the values measured at 40 GHz. Representative pre- and post-proton radiation plots of f_T and f_{max} are depicted in Figures 20 and 21, respectively. As has been reported for other SiGe HBT technologies, there is negligible change between the pre- and post-radiation f_T. At first glance there appears to be a substantial decrease ($\sim$ 10%) in the post-radiation f_{max}. If the degradation was truly due to radiation, however, one would expect to see an increase in the dynamic base resistance (r_{bb}) as well. However, Figure 22 clearly indicates there is essentially no change in r_{bb} post radiation. This leads us to believe that the variation of f_{max} post radiation is likely a result of the inherent error associated with the S-parameter measurement and de-embedding of these particular *ac* test structures. Similar

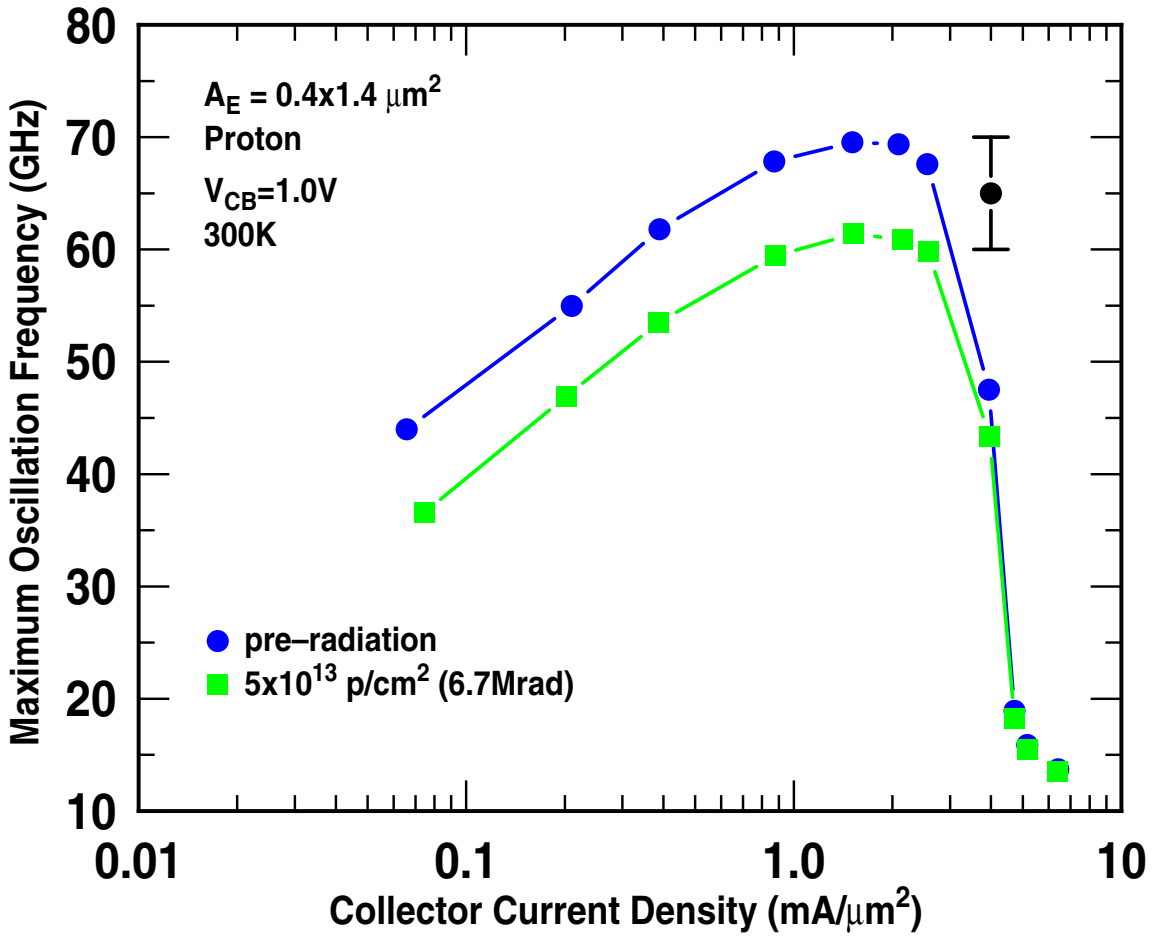

Figure 21: f_{max} versus J_C as a function of proton fluence.

results were observed for gamma radiation. The *ac* parameters are essentially unaffected by proton and gamma radiation, and is consistent with reported data for other commercial SiGe technologies.

3.2.4 Differential Oscillator Circuit

A fully-integrated differential LC tank oscillator [31] was incorporated in the proton irradiation study to investigate the effects of irradiation on a highly relevant (and potentially radiation sensitive) RF circuit. This oscillator was fabricated on a pre-production hardware lot using the identical process flow (National BiCMOS8) and device dimensions. The circuit is based on a standard feedback topology and dissipates 12mW of a 3.3V supply,

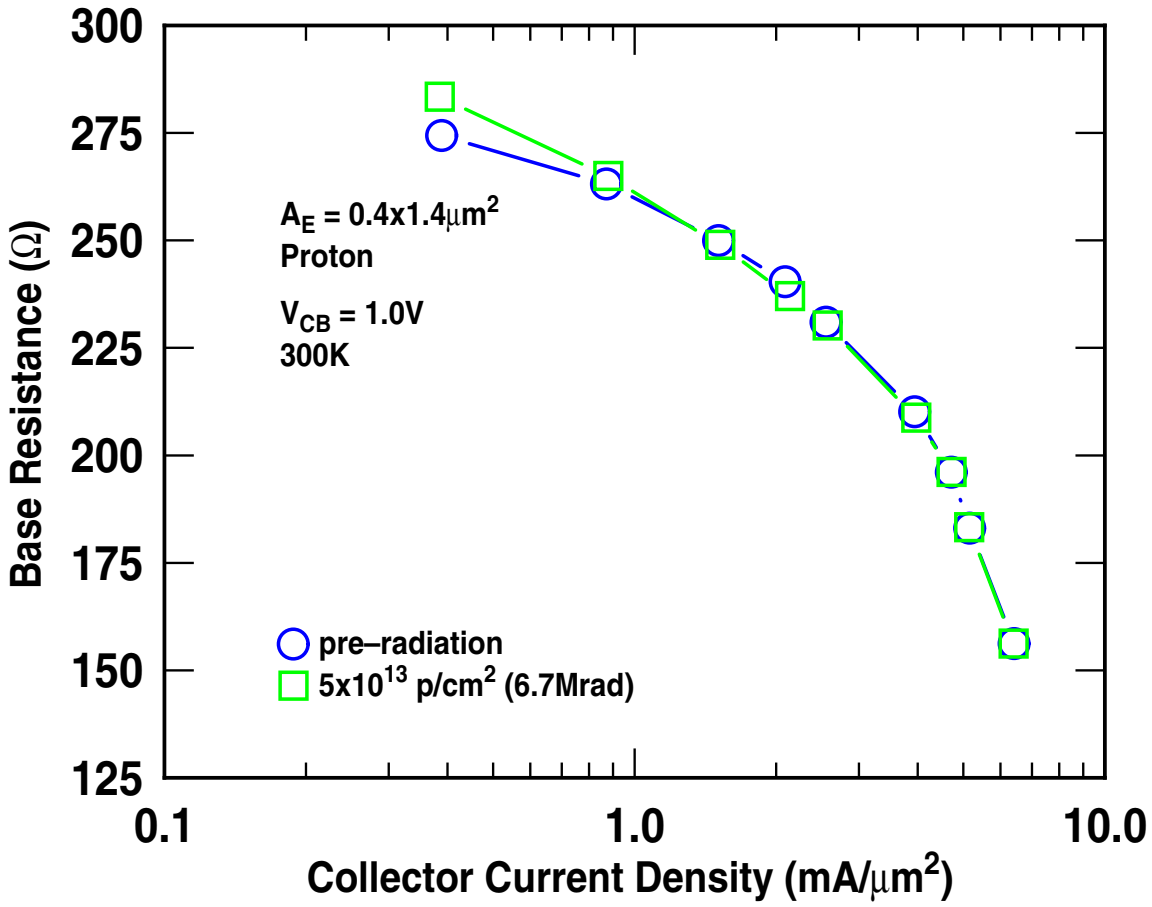

Figure 22: r_{bb} as a function of proton fluence.

Table 2: Pre- and Post-radiation Oscillator Performance Metrics.

Performance Metrics	Pre-Radiation	Post-Radiation
Output Power (dBm)	-6.8	-7.4
Oscillation Frequency (GHz)	2.63	2.63
Phase Noise at 100 kHz offset (dBc/Hz)	-91	-89
Phase Noise at 1 MHz offset (dBc/Hz)	-118	-117

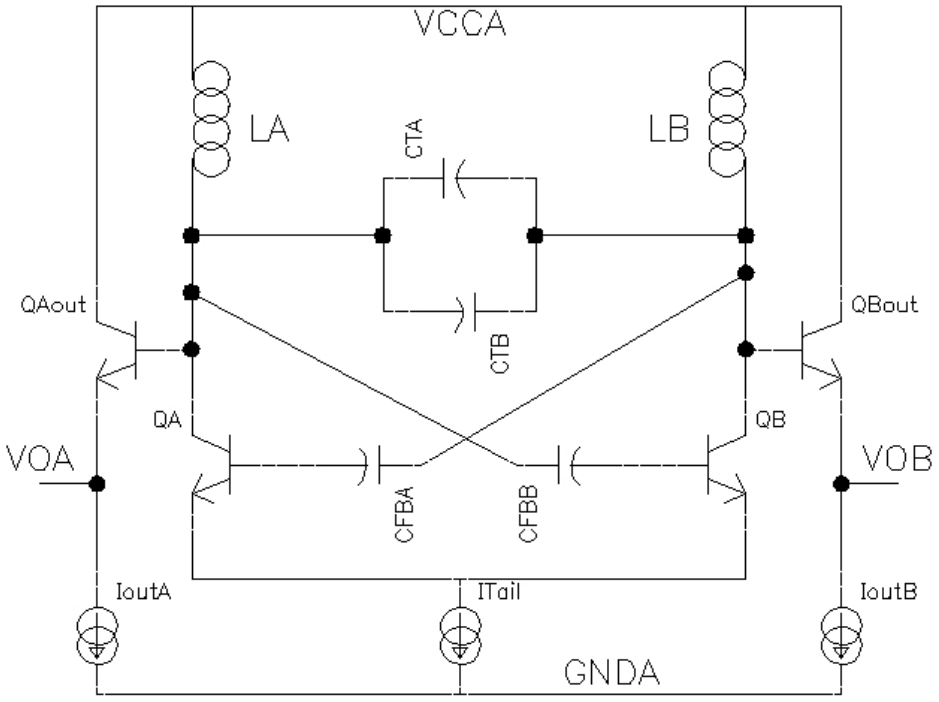

Figure 23: Schematic of SiGe LC oscillator.

while delivering an output power of -6.8 dBm at a frequency of oscillation of 2.63 GHz. The schematic is shown in Figure 23. The phase noise performance of the oscillator was measured at wafer level both pre- and post-radiation. The pre-radiation phase noise performance was -118 dBc/Hz at 1MHz offset from the frequency of oscillation. There was no measurable difference in performance post radiation, as indicated in Table 2, clearly good news from a circuit perspective.

3.2.5 SiGe HBT Technology Comparison

The *dc* and *ac* proton radiation response for the present work is compared with previously published results on four different SiGe HBT technologies, as shown in Table 3. Meaningful comparisons between various technologies are challenging to perform due to differences in Ge profile, standard device geometries, etc. To facilitate a clearer comparison, the *dc* performance metrics were calculated in terms of base current density at a fixed V_{BE} of 0.6V. Note that the National BiCMOS8 (this work) EB junction is slightly more susceptible

Table 3: Comparison of Proton Tolerance for the Present Work and Various Previously Reported SiGe HBT Technologies.

Parameters	This Work - 60 GHz	SiGe #1 - 50 GHz [7]	SiGe #2 - 28 GHz [32]	SiGe #3 - 120 GHz [8]	SiGe #4 - 120 GHz [33]
Fluence(p/cm^2)	5×10^{13}	5×10^{13}	5×10^{13}	5×10^{13}	5×10^{13}
$J_{B(post)} - J_{B(pre)}$ at V_{BE} = 0.6V (nA)	9.23	2.28	4.31	11.57	5.71
Inverse Mode $J_{B(post)} - J_{B(pre)}$ at V_{BE} = 0.6V (nA)	7.19	23.70	160.02	32.65	16.46
$\beta_{(post)}/\beta_{(pre)}$ V_{BE}=0.7V	0.06	0.28	0.16	0.05	0.27
$f_{T(post)}/f_{T(pre)}$ (V_{CB}=1.0V)**	0.95	0.97	—	0.98 *	0.99*
$f_{max(post)}/f_{max(pre)}$ (V_{CB}=1.0V)**	0.88	0.97	—	0.92 *	0.96*

* Data measured at V_{CB}=0.5V with fluence of 7x10^{12} p/cm^2

** estimated 10% error in measurement + extraction

to radiation damage, while the CB junction is more robust than other reference technologies. However, in general, all five SiGe technologies exhibit exceptional proton irradiation tolerance without additional radiation hardening.

3.3 Proton Radiation Effects in Si nFETs

Si nFETs with a channel width of 10.0 μm and lengths ranging from 1.6 to 0.12 μm were used for the *dc* investigation. The transistors were designed using conventional high-speed layouts, and do not, for instance, use annular (enclosed) layouts for reducing radiation damage. The *ac* measurements were made on multi-fingered (32 fingers) devices with a W/L of 2.0/0.12 μm per finger. The 63.3MeV proton irradiation was performed at the Crocker Nuclear Laboratory at the University of California at Davis. The dosimetry measurements used a five-foil secondary emission monitor calibrated against a Faraday cup. The radiation source (Ta scattering foils) located several meters upstream of the target establish a beam spatial uniformity of about 15% over a 2.0 cm radius circular area. Beam currents from

about 20 nA to 80 nA allow testing with equivalent gamma doses from 10 krad to 1Mrad. The dosimetry system has been previously described [25], [26], and is accurate to about 10%.

The Si nFET *dc* test structures were irradiated at equivalent gamma doses ranging from 10 krad to 1 Mrad (proton fluences from 7.4×10^{10} to 7.4×10^{12}) under two different bias conditions. Under the first condition, the source, drain, and substrate terminals were grounded, and V_{DD} (1.2V) was applied to the gate terminal (the conventional worst case bias condition for FETs). For the second bias condition, the source and drain terminals were grounded, V_{DD} (1.2V) was applied to the gate terminal, and negative V_{DD} (-1.2V) was applied to the substrate terminal. The *ac* test structures and circuits were irradiated with all terminals floating at a dose of 1 Mrad. Wirebonding of *ac* test structures and circuits is not compatible with robust broadband measurements, and hence on-wafer probing of S-parameters was used to characterize the high-frequency performance. The samples were measured at room temperature with an Agilent 4155 Semiconductor Parameter Analyzer (*dc*) and an Agilent 8510C Vector Network Analyzer (*ac*).

3.3.1 *dc* Results

Figures 24 and 25 depict the transfer characteristics for Si nFETs with W/L=10.0/0.12 μm with 0V and -1.2V substrate irradiation bias conditions, respectively. The substrate was grounded during measurement for both irradiation bias conditions. For the 0V irradiation substrate bias, the subthreshold leakage is essentially constant ($\sim$ 1 pA) for doses up to 60 krad and then appears to saturate at approximately 10 nA for doses from 100 krad to 1 Mrad. Observe that there is significantly more subthreshold leakage for the -1.2V irradiation substrate bias condition. The leakage occurs at doses as low as 10 krad. A similar apparent leakage saturation occurs slightly above 10 nA for doses from 60 krad to 1 Mrad. It appears that there are two fundamentally different leakage mechanisms at work for the two irradiation substrate bias conditions. In both cases, however, the off-state

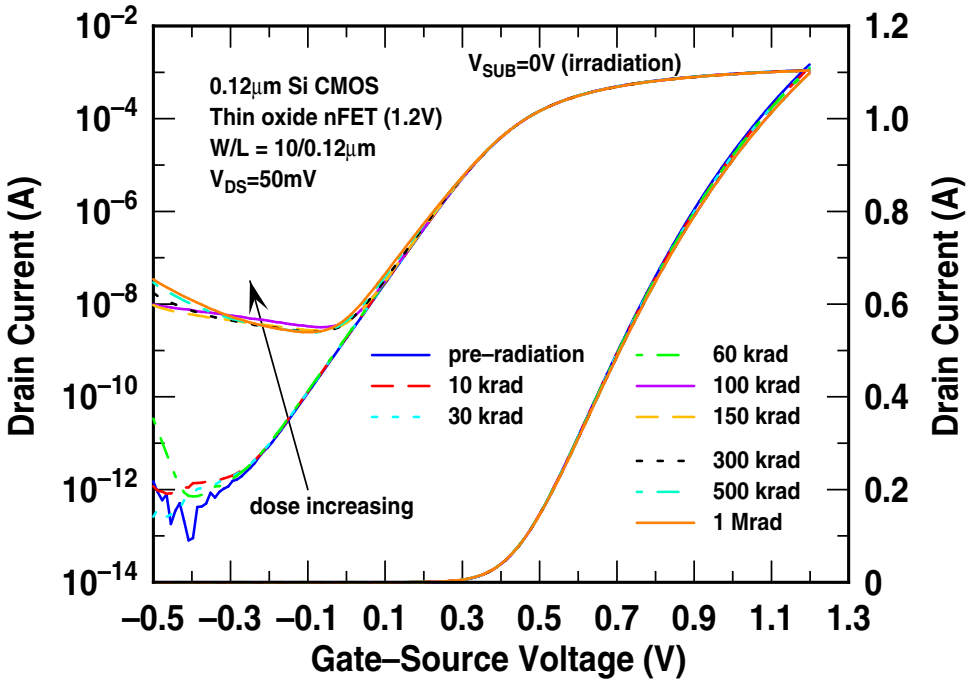

Figure 24: Transfer characteristics for an irradiation substrate bias of 0V as a function of equivalent dose.

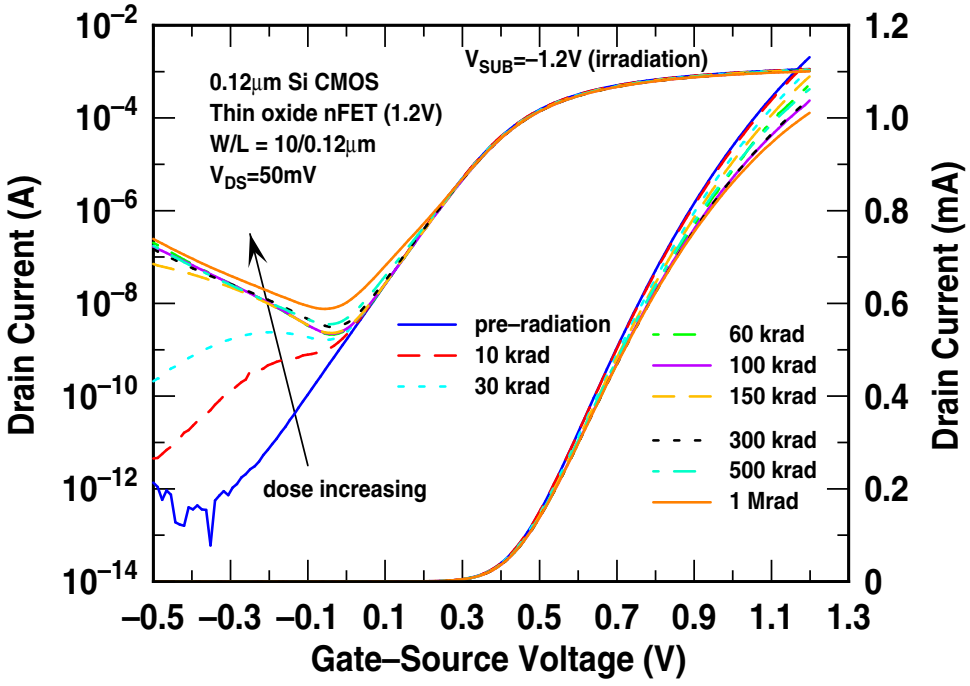

Figure 25: Transfer characteristics for an irradiation substrate bias of -1.2V as a function of equivalent dose.

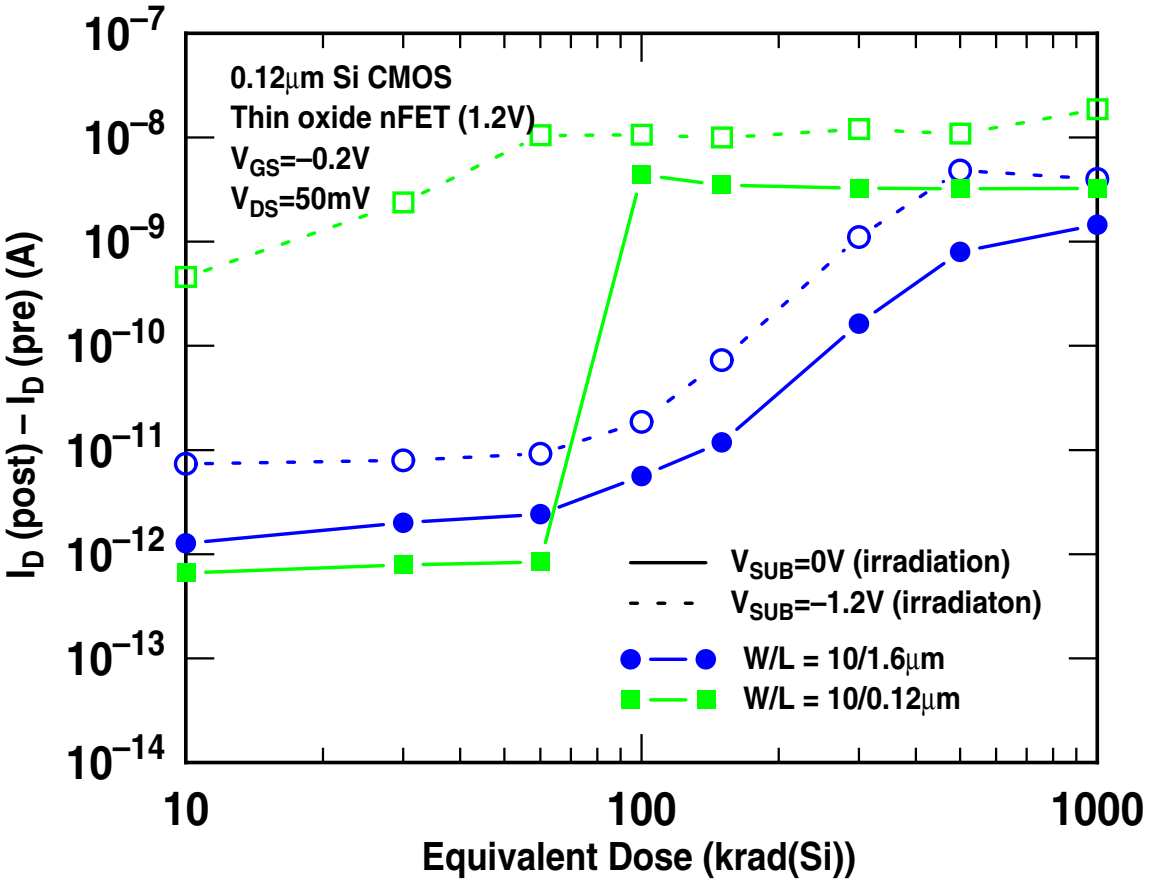

Figure 26: Change in sub-threshold leakage as a function of equivalent dose.

leakage is in the 1.0 nA/μm range, which is acceptable for many circuits, without using layout techniques or process modifications for hardening.

Figure 26 shows the change in net subthreshold leakage post-radiation for devices of different channel lengths (1.6 and 0.12 μm) at both substrate bias conditions. The difference in radiation-induced leakage due to substrate irradiation bias is again manifested here. In addition, we also see that the shorter channel device suffers more radiation damage than the longer channel device. This effect has previously been reported for 180 nm nFETs [35].

The threshold voltage shift ($\Delta V_T = V_{T_{post}} - V_{T_{pre}}$) was extracted for the same devices and is shown in Figure 27. The pre- and post-radiation threshold voltage was extracted using the peak transconductance technique. In this method, the point of maximum slope on the $I_D - V_{GS}$ curve is determined by a maximum in the transconductance, $g_m = \partial I_D / \partial V_{GS}$, a straight

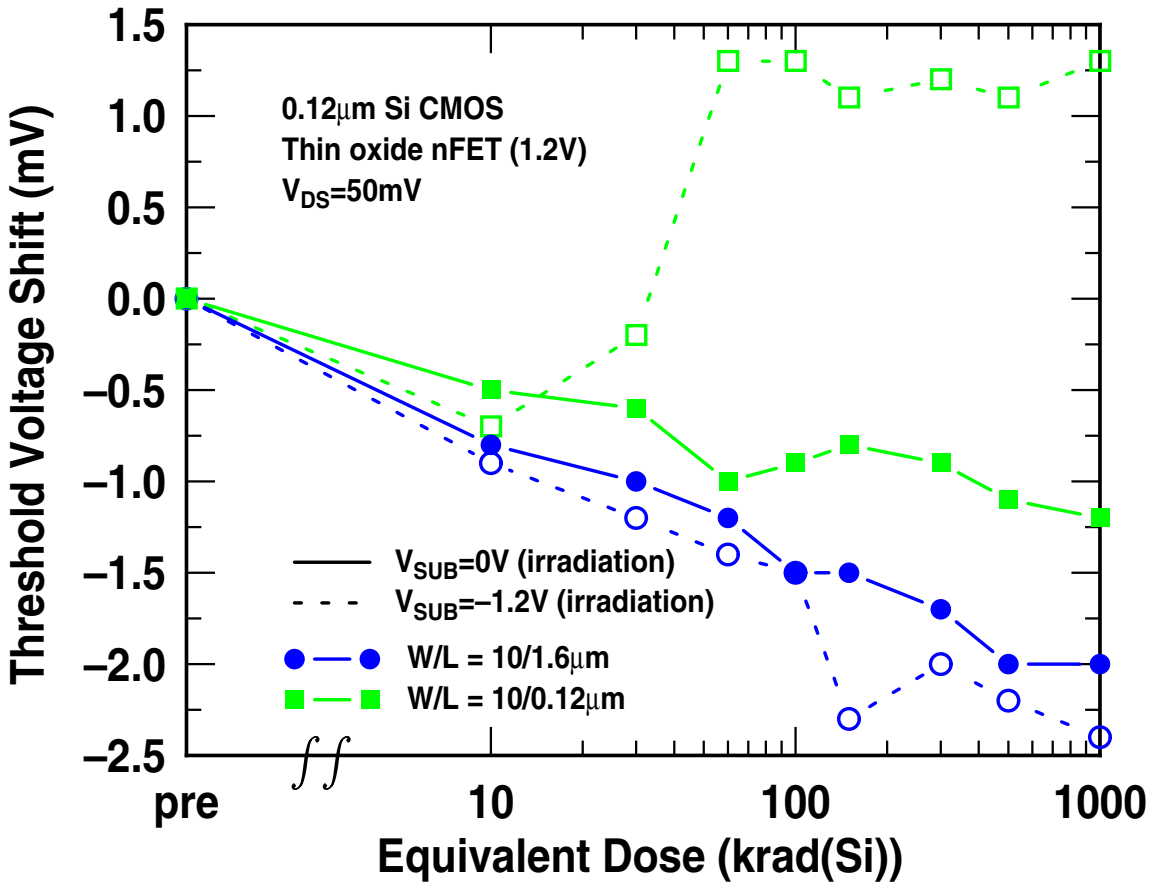

Figure 27: Threshold voltage shift as a function of equivalent dose.

line is fitted to the curve at that point and extrapolated to $I_D = 0$. The threshold voltage is given by the extrapolated intercept [34]. There is very little change in threshold voltage up to 1 Mrad, as expected, due to the very thin gate oxide. The longer channel (L=1.6 μm) device exhibits a decrease in V_T with radiation for both substrate irradiation bias conditions, whereas the shorter channel (L=0.12μm) device demonstrates a V_T decrease only for the 0V substrate bias. Interestingly, the V_T increases after a dose of 30 krad for the short channel, negative irradiation substrate bias condition. This increase in V_T post radiation has been reported previously for short channel devices with terminals floating during irradiation [35].

The pre- and post-radiation effective mobility (μ_{eff}) was extracted as a function of gate overdrive (V_G-V_T) using a technique capable of taking into account the bias dependence

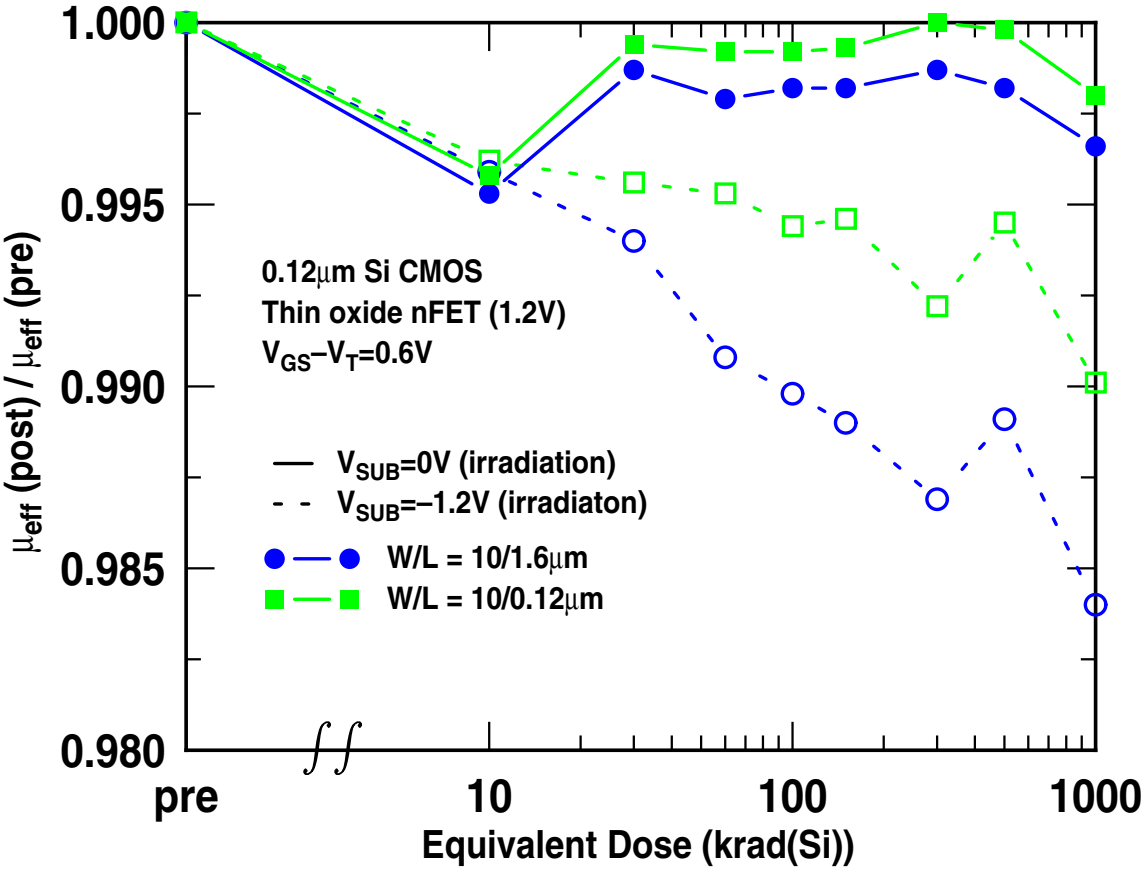

Figure 28: Effective mobility degradation as a function of equivalent dose.

of the source-drain resistance (R_{SD}) in lightly-doped-drain (LDD) CMOS devices [36]. The first step in this extraction technique is determining the total resistance (R_{tot}) in the presence of series resistance given by:

$$R_{tot}(\text{measured}) \equiv \frac{V_{DS}}{I_{DS}} = A(L_m - \Delta L) + R_{SD} = AL_m + B \tag{19}$$

where

$$A = \frac{1}{\mu_{eff} W Q_{inv}} \tag{20}$$

$$B = R_{SD} - A\Delta L. \tag{21}$$

Parameters A and B are the slope and intercept of the measured resistance R_{tot} versus mask length L_m at given gate bias. The effective mobility can be extracted without involving

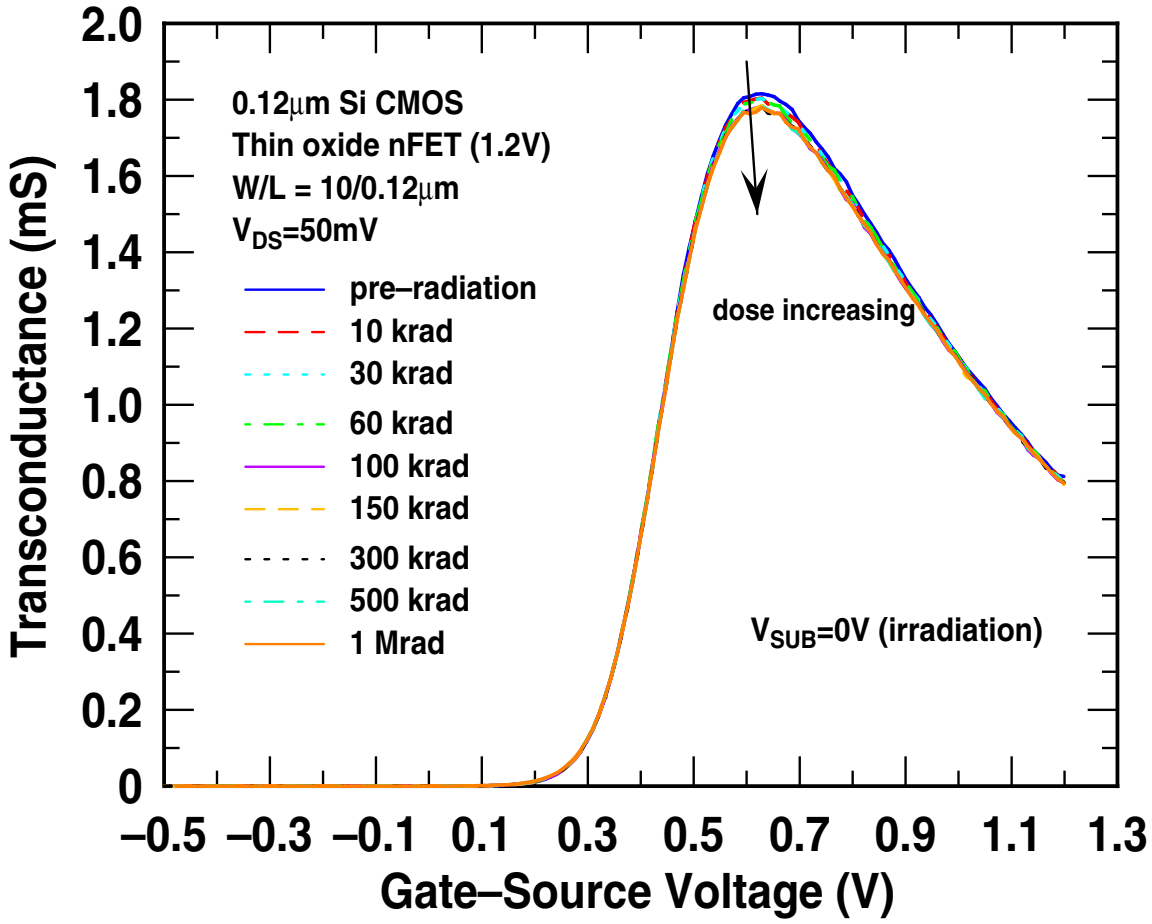

Figure 29: Transconductance versus gate-source voltage for an irradiation substrate bias of 0V.

$L_{eff}(\Delta L)$ by using multiple devices with different mask lengths, thus removing the series resistance effect:

$$\mu_{eff} = \frac{1}{WQ_{inv}A}. \tag{22}$$

Figure 28 illustrates the μ_{eff} degradation as a function of equivalent dose. There is essentially no change in mobility with proton radiation for either channel length or substrate bias condition. This result is expected because, as mentioned in Chapter II, any reduction in post-radiation mobility is due to scattering at the radiation-induced oxide and interface traps. However, in this technology the gate oxide is very thin (2.2 nm) and very few charges are trapped leading to negligible mobility degradation.

From the linear transfer characteristics (Figures 24 and 25), we see there is very little

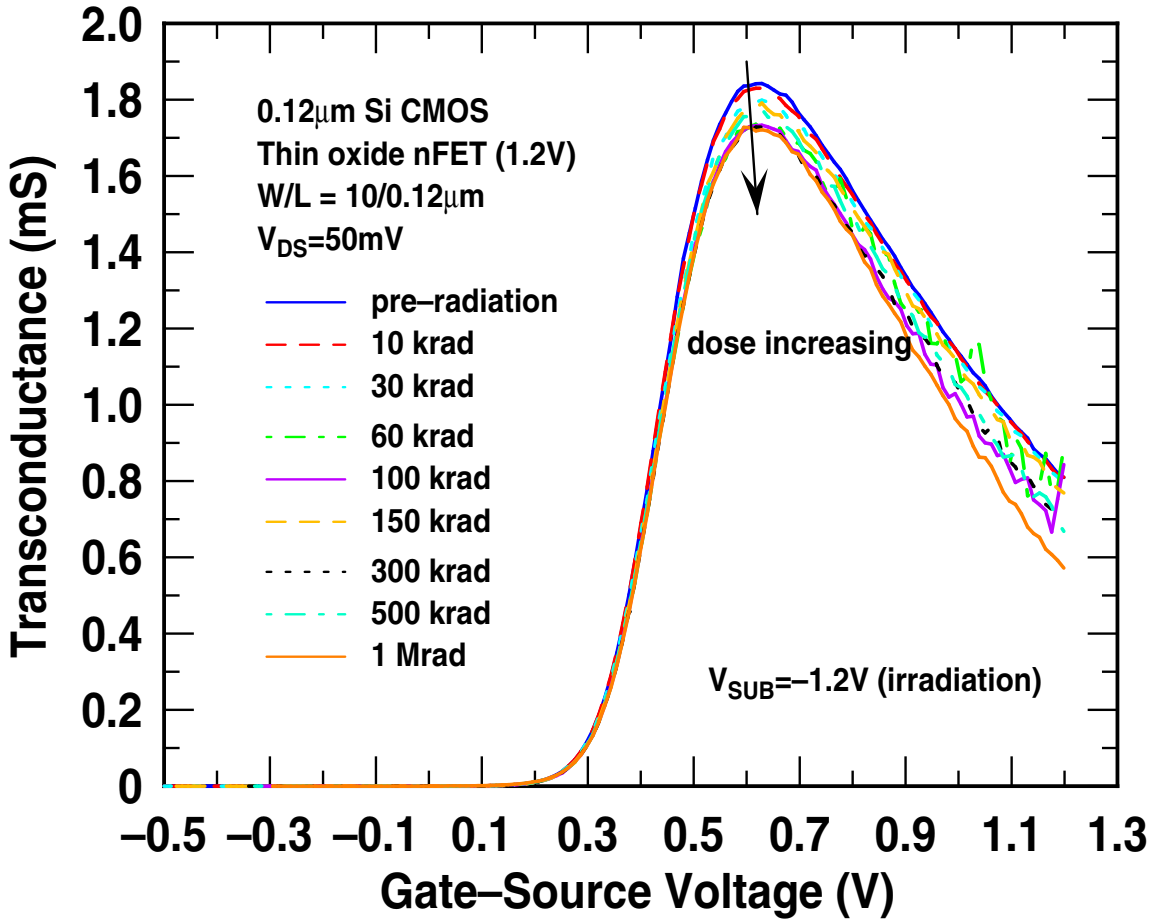

Figure 30: Transconductance versus gate-source voltage for an irradiation substrate bias of -1.2V.

degradation in the drain current (I_D) for the strong inversion region of operation for the 0V substrate bias condition. This however, is not the case for negative substrate bias irradiation. Here we see significant degradation in the strong inversion region. As expected, this is also apparent in the transconductance (g_m), as seen in Figures 29 and 30. Since there is very little change in both V_T and μ_{eff} post radiation, the g_m degradation is believed to be due to an increase in R_{SD}, and is consistent with enhanced damage in the gate-to-drain overlap region (i.e., the LDD) in the Gate-Induced-Drain-Leakage path described in the next section.

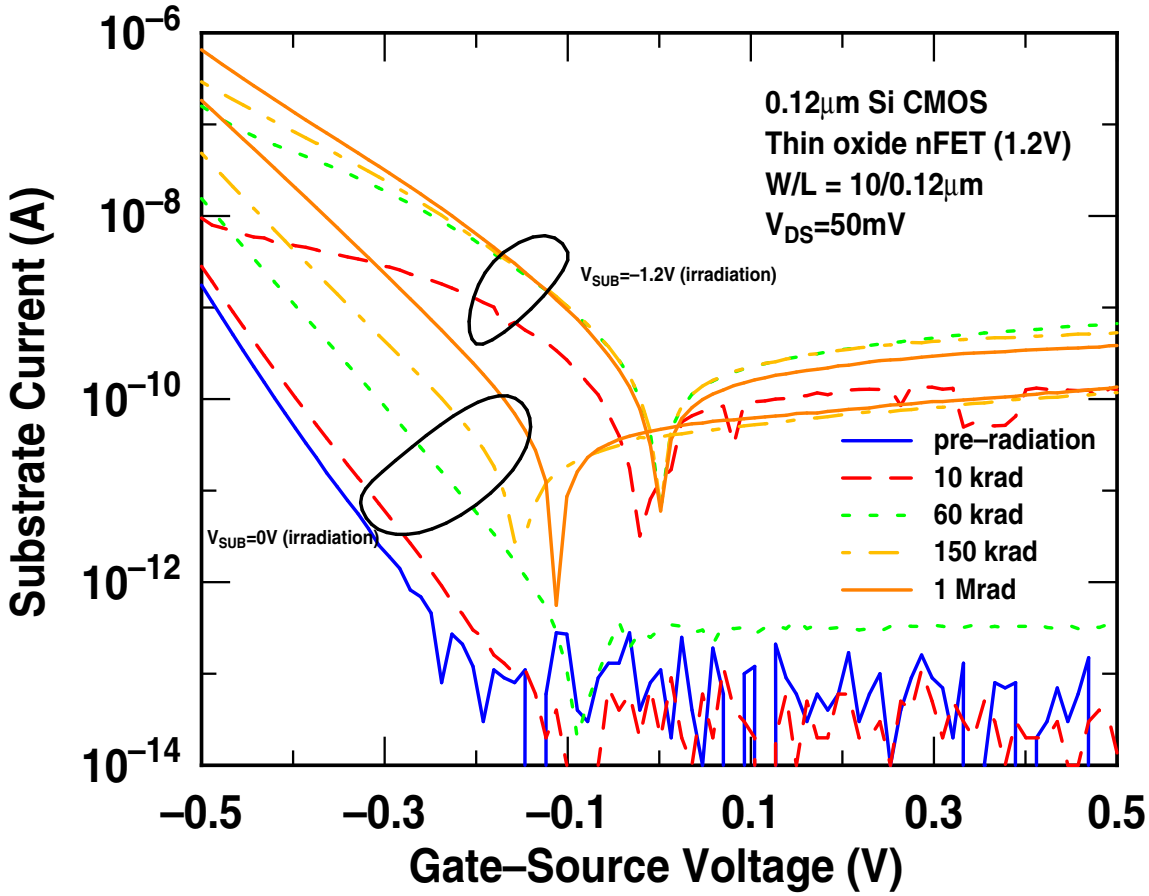

Figure 31: Substrate current for both irradiation substrate biases as a function of equivalent dose.

3.3.2 Leakage Mechanisms

An examination of the substrate current versus gate-source voltage for both substrate bias conditions (see Figure 31), as well as the transfer characteristics, allows for better understanding of the leakage mechanisms in play. We believe that in both substrate bias cases the subthreshold leakage is due to a combination of two radiation induced leakage mechanisms. One cause of subthreshold leakage is the presence of radiation-induced charge physically located in the region where the gate extends beyond the shallow trench isolation (STI) edge (see Figure 32). At sufficiently high dose a parasitic leakage path forms between the source and drain, producing a shunt leakage path [37]. A classic signature of STI edge leakage is a positive sloping drain current for gate voltage (V_G) < 0.

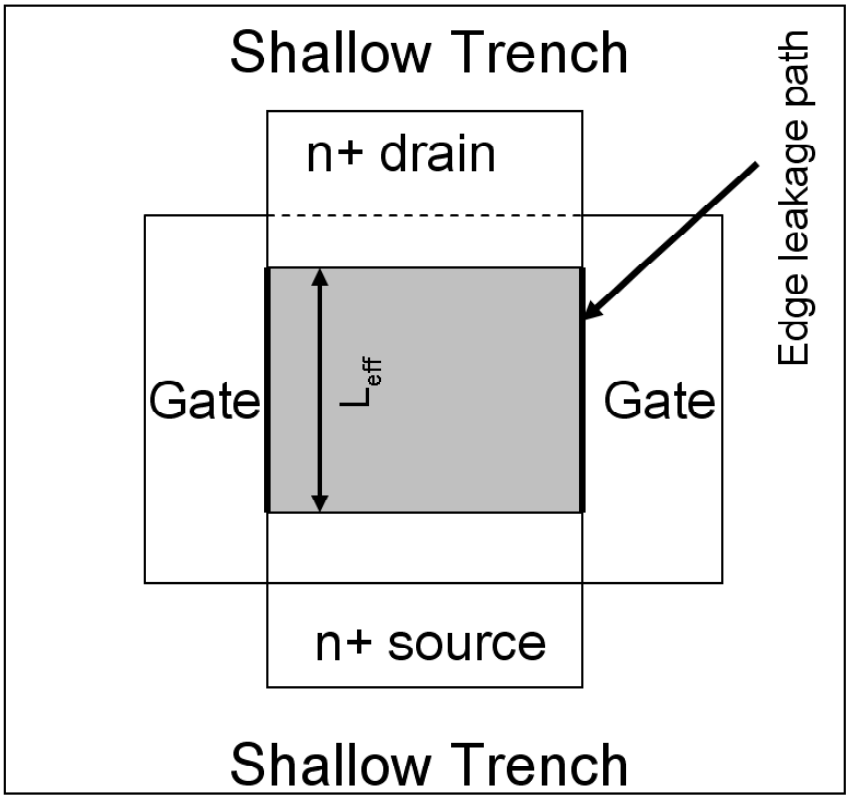

Figure 32: A schematic top view of the STI edge leakage path.

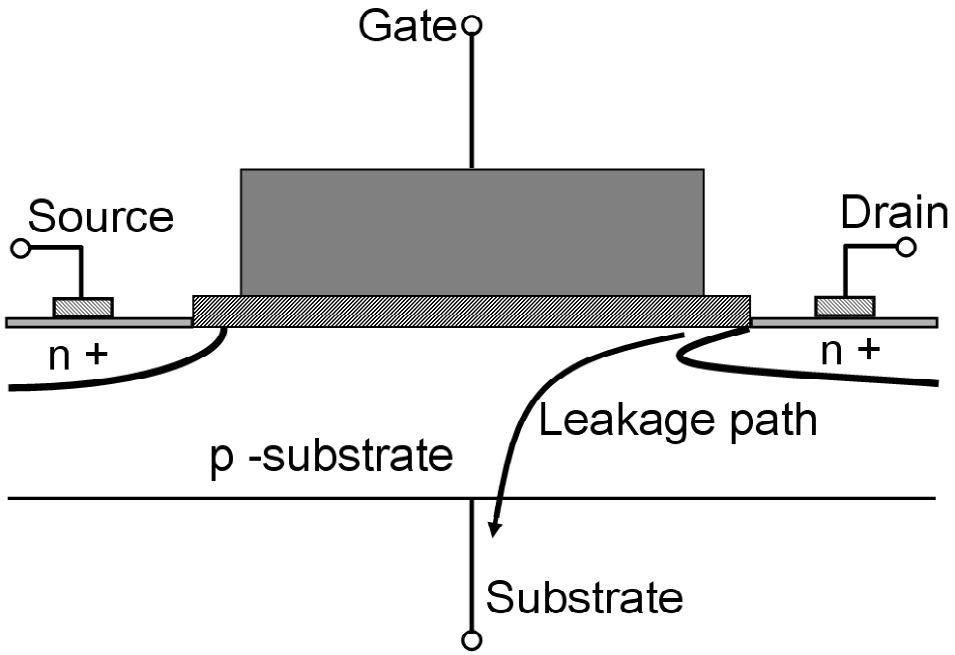

Figure 33: A schematic view of the GIDL leakage path.

The other cause of subthreshold leakage appears to be radiation-induced tunneling (band-to-band and/or trap-assisted) in the gate-to-drain overlap region, as evidenced by a negative sloping drain current for $V_G < 0$. This leakage mechanism is generally known as Gate-Induced-Drain-Leakage (GIDL) [38], [39]. In GIDL, the junction field increases with decreasing gate bias, causing minority carriers under the gate to be swept into the substrate (see Figure 33), resulting in increased leakage current. For the 0V substrate bias case, Figure 31 indicates a strong GIDL component that increases with increasing dose. However, the transfer characteristic (Figure 24) does not show the expected strong negative slope due to GIDL. We believe the transfer characteristic shows a "weak" negative slope because the STI edge leakage at high dose (> 60 krad) is larger than GIDL (see Figure 34). In the -1.2V substrate bias case, as Figure 25 indicates, the transfer characteristics display the classic signature of STI edge leakage for doses of 10 and 30 krad. Above 30 krad, it appears there is a very strong GIDL component. This is corroborated by Figure 31. It seems that the GIDL component is stronger than the STI edge leakage component for the -1.2V

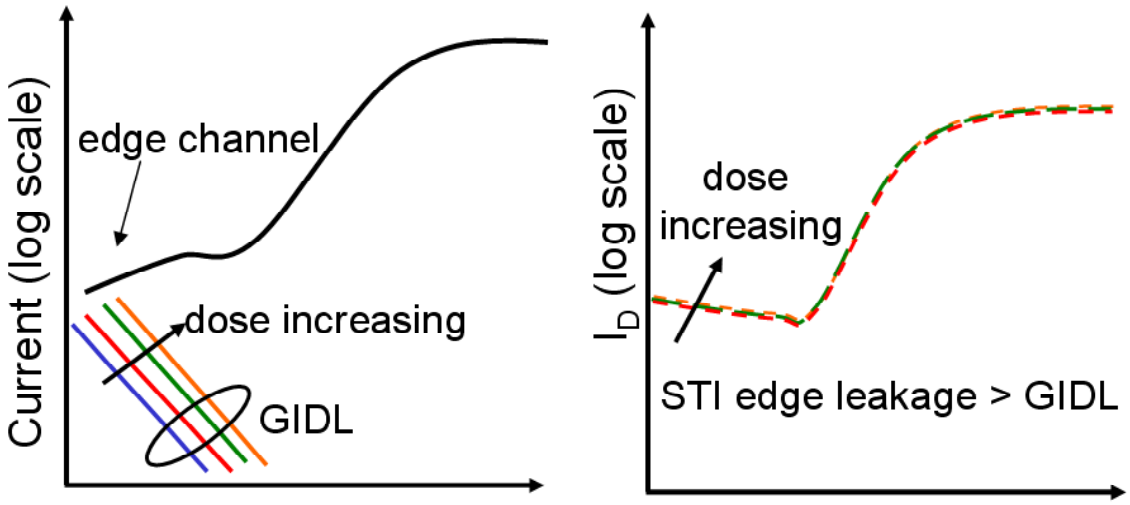

Figure 34: Leakage current components for 0V irradiation substrate bias.

substrate bias condition. Figure 31 indicates that GIDL saturates at high dose for the -1.2V substrate bias condition, but increases with dose for the 0V case. The GIDL component is larger for the negative bias substrate condition presumably due in part to the higher field inducing more traps (damage) in the drain-substrate junction during irradiation. The GIDL observed in this work is clearly radiation triggered and is also dependent on the body bias during exposure, and thus of potential concern from a hardness assurance perspective. 3-D simulations will be required to determine the exact leakage mechanisms. As mentioned above, there is clearly more radiation induced damage for the -1.2V irradiation substrate bias. Similar stress-induced degradation has been reported for this negative substrate bias [40].

It has been previously reported that negative substrate bias during measurement can suppress the radiation-induced STI leakage. In that work, the substrate was grounded during irradiation [37]. The present work examines the effects of negative substrate bias during operation for devices irradiated with the -1.2V substrate bias condition. Figure 35 shows the $I_D - V_{GS}$ curve for measurement substrate potentials of both 0V and -1.2V, at two values of drain voltage, after 1 Mrad total dose. It is evident that a negative operational substrate

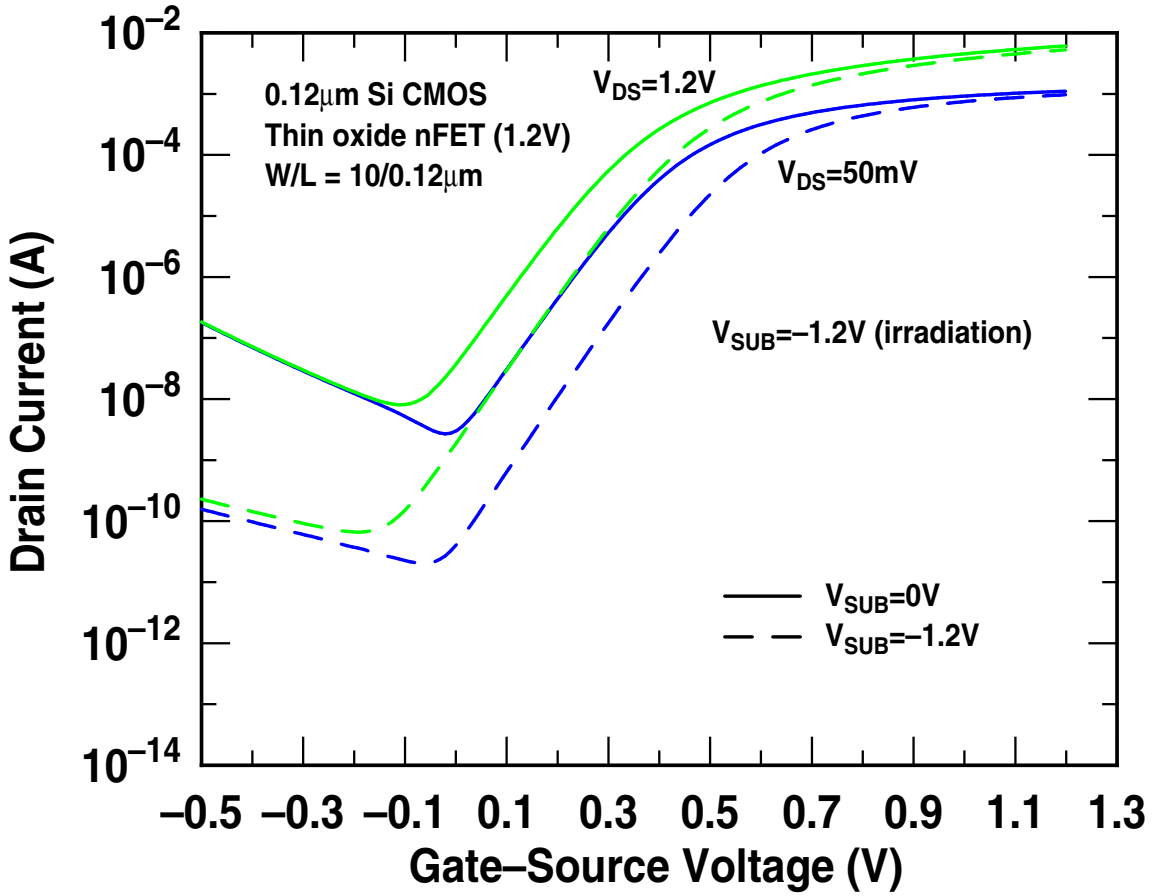

Figure 35: Transfer characteristics after 1 Mrad equivalent dose for substrate biases of 0 and -1.2V.

bias is very effective in reducing the radiation-induced leakage, despite the enhanced damage, compared with the 0V operational substrate bias. Note that these measurements were made approximately four months after the 1 Mrad irradiation. The subthreshold leakage was essentially unchanged from that measured in-situ after 1 Mrad.

3.3.3 *ac* Results

The scattering parameters (S-parameters) were also measured for a thin oxide nFET with W/L = 32 gate fingers. Open and short structures were used to de-embed the data in order to calculate the small-signal current gain (h_{21}). The cutoff frequency (f_T) was determined from the magnitude of h_{21} by extrapolating a -20 dB/decade slope across a wide frequency

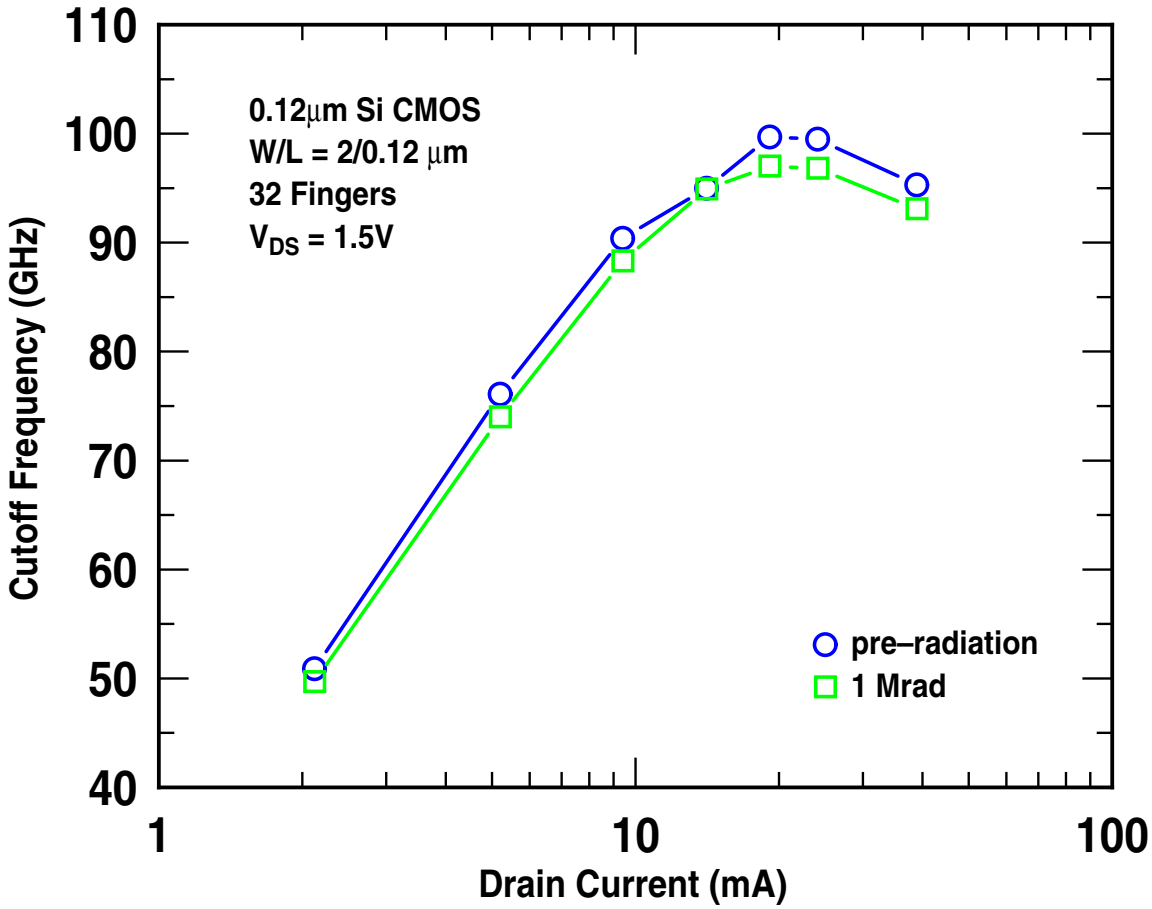

Figure 36: Cutoff frequency as a function of drain current pre and post radiation.

range. The pre- and post-proton radiation f_T-I_D characteristics are depicted in Figure 36. There is an apparent very slight degradation in f_T post-radiation ($\sim 3\%$), but this is well within the error associated the measurement, and judged to be negligible.

3.3.4 Technology Comparison

Finally, we compare the proton tolerance of this work with a previously reported 180 nm CMOS technology node [41]. The change in subthreshold leakage is shown for the 180 nm and 130 nm nFETs in Figure 37. The scaled CMOS exhibits improved radiation tolerance than the previous generation. This off-state leakage result is somewhat surprising, in fact, since the STI thickness of the 130 nm CMOS is actually slightly thicker than that for the 180 nm process. This is presumably due to the subtleties associated with the STI-to-channel

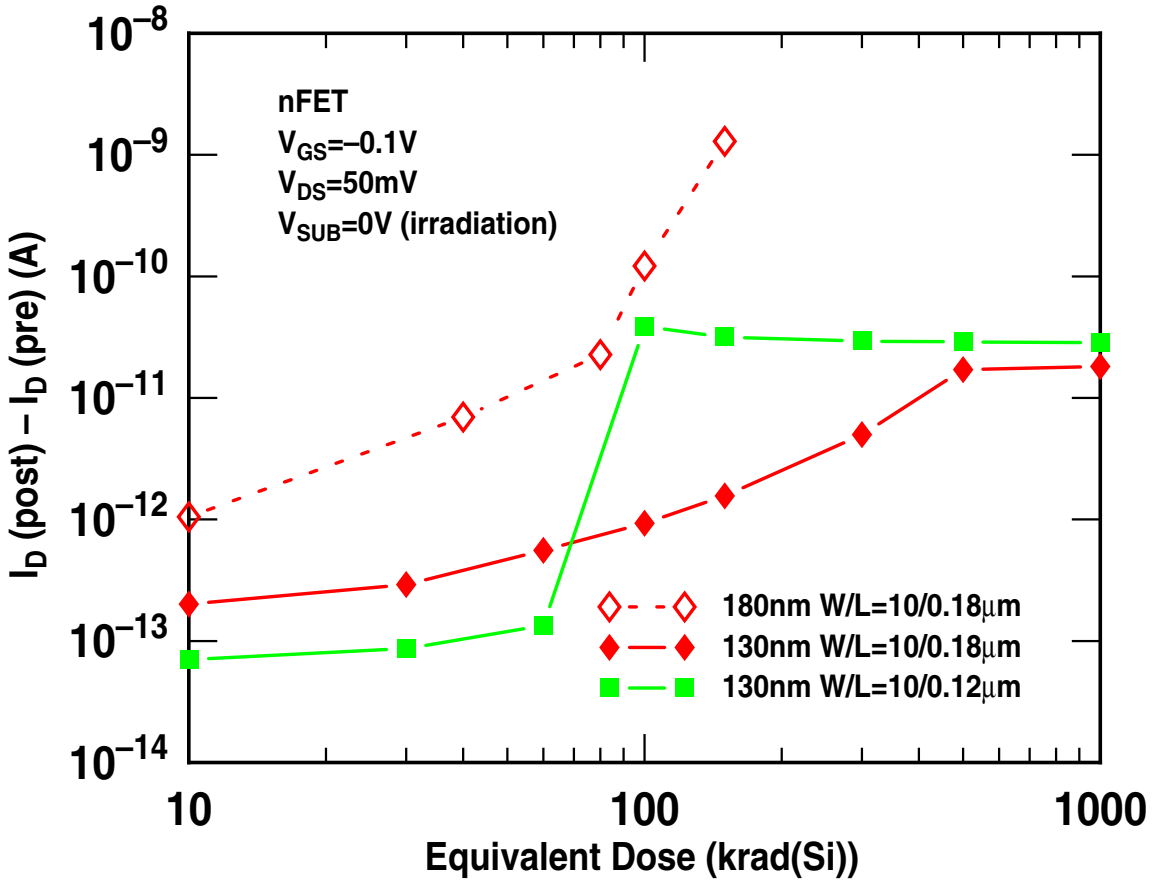

Figure 37: Change in sub-threshold leakage for 130 and 180 nm technology nodes.

physical shape at the channel edge.

3.4 Summary

This work reports the first proton and gamma radiation tolerance study on the National BiCMOS8 SiGe technology. When compared with the *dc* results for previously reported SiGe technologies, the EB junction appears to be slightly less robust, while the CB junction is more tolerant. The *ac* and oscillator results indicate negligible performance degradation post radiation. The National BiCMOS8 SiGe technology is tolerant to both proton and gamma radiation (up to Mrad-level equivalent dose) without any radiation hardening, indicating that it is potentially a viable option for spaceborne electronic systems.

This chapter also investigates the impact of substrate bias on proton damage in a 130 nm

CMOS technology. For both irradiation substrate bias conditions the subthreshold leakage is due to a combination of two radiation-induced leakage mechanisms, STI edge leakage and GIDL. We find that grounded versus negative substrate bias during radiation produces different dominant damage mechanisms. STI edge leakage appears to dominate in the 0V bias case, while the GIDL component appears larger for the -1.2V bias condition. There is very little change in threshold voltage and mobility post radiation due to the thin oxide in this technology. The *ac* results suggest there is negligible change in f_T post radiation. This 130 nm CMOS also shows improved radiation tolerance over the 180 nm technology node. The off-state leakage for both bias conditions is tolerable for many circuits, without and radiation hardening.

CHAPTER IV

IMPACT OF STRAIN ON SI CMOS

4.1 Introduction

Si CMOS geometrical scaling to nanometer dimensions is progressively becoming more expensive and complicated as scaling is approaching its practical limits. Straining silicon is widely recognized as a potential alternative to dimensional scaling for enhanced CMOS performance. Strain alters the band structure of silicon, which in turn changes the electrical properties of the material. Several publications have demonstrated significant drain current improvements (10 to 30%) associated with strain-induced carrier mobility enhancement.

Two main methods of inducing strain in MOSFETs have been explored by various groups [42]. In one method, biaxial tensile strain is induced by Si-SiGe lattice mismatch. Here a thin epitaxial Si layer is grown on a relaxed SiGe substrate. Biaxial tensile strain is induced in the Si layer because the lattice constant of Si is smaller than the SiGe lattice constant (see Figure 38). The strain alters the bandstructure leading to mobility enhancement, which will be described in more detail below. Biaxial tensile strain in the Si layer increases with increasing Ge content in the SiGe layer. There are several issues with this straining method such as dislocation defects in the SiGe layer, Si relaxation due to thermal processing, and Ge out-diffusion. Optimization of the thermal budget during processing can eliminate strain relaxation and Ge out-diffusion in the channel layer. Another issue with this method of strain is the requirement of a large Ge content to achieve the large amount of tensile strain needed for significant improvement in hole mobility. Moreover, this enhancement decreases at high vertical electric fields. Typically, Ge > 20% (equivalent to approximately 0.8% strain) is necessary to see sizeable mobility enhancement [43]. However, there are process integration issues for large Ge content.

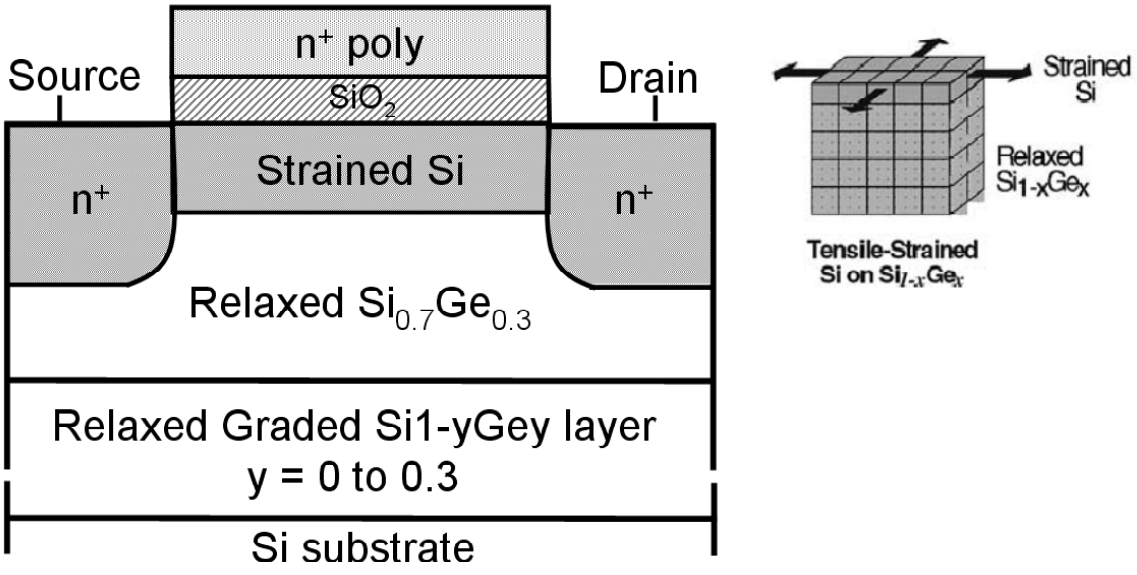

Figure 38: Illustration of a strained Si/relaxed $Si_{1-x}Ge_x$ nFET and biaxial tensile strain after [42].

Another method is process induced strain, which can place tensile or compressive uniaxial strain in different regions of the device. There can be many variations of process induced strain. One method that has been implemented in a 90 nm logic technology makes use of $Si_{1-x}Ge_x$ in the source and drain regions of the pMOSFET and a silicon nitride capping film for the nMOFSET [44]. The $Si_{1-x}Ge_x$ in the source and drain regions induces uniaxial compressive strain in the channel of the pMOSFET. The silicon-nitride capping layer introduces in-plane tensile strain and out-of-plane compressive strain in the nMOSFET. Thus, this method can be used to optimize nMOSFET and pMOSFET devices on the same wafer independently. A drawback of process induced strain is each method is very sensitive to device layout.

A third way of inducing strain is mechanical, which is presented here. This method is applied post fabrication, unlike the two techniques mentioned above [45],[46]. Both uniaxial and biaxial strain can be realized in this manner. Previous work has studied the effects of uniaxial mechanical strain on MOSFET devices [45]. In this work, the results

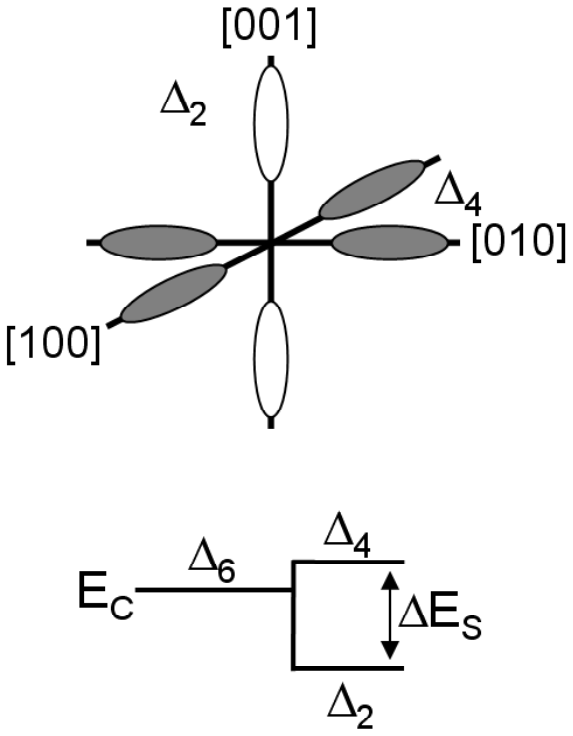

Figure 39: Conduction band splitting for biaxial strain.

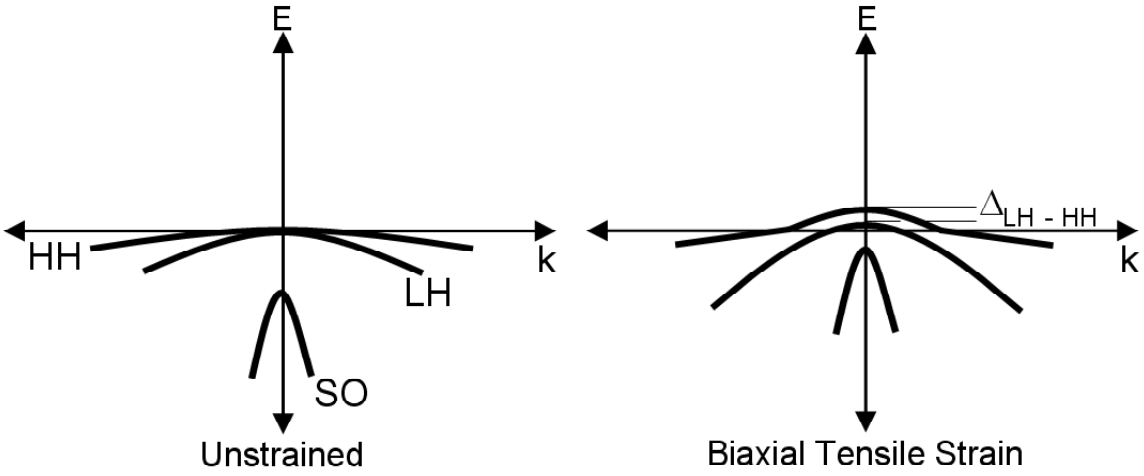

Figure 40: Valance band splitting for biaxial strain after [44].

of mechanical planar biaxial tensile strain applied to a Si/SiGe HBT BiCMOS technology are reported. Biaxial strain is known to alter both the conduction and valence bands of Si. Figure 39 illustrates the biaxial strain induced splitting of the previously degenerate Si conduction band. The valence band in the in-plane direction is shown in Figure 40. Here, biaxial tensile strain increases the energy separation between the heavy hole and light hole bands. The strain alters the shape of valence bands, while leaving the shape of the conduction bands unchanged [47].

4.2 Strain Effects in Si CMOS

Three fully-integrated BiCMOS technologies were investigated in this study: a 0.50μm, 50GHz peak f_T SiGe HBT BiCMOS, the 0.35μm standard Si CMOS on this technology platform (strained together on the same die for unambiguous comparisons), a 0.50μm epitaxial base Si BJT control (fabricated identically in the same wafer lot as the SiGe HBT), the 0.35μm standard Si CMOS on this technology platform (identical to the Si CMOS on the SiGe HBT wafer), and a 0.18μm 120GHz peak f_T SiGe HBT BiCMOS, with three distinct 0.18μm Si CMOS device versions [7], [8].

These wafers were diced and thinned to (flexible) membrane dimensions ($\leq$ 25μm thickness). Planar biaxial strain was achieved by using a novel differential thermal bonding technique [48], [49], in which the thinned membrane is bonded to a substrate of different coefficient of thermal expansion (CTE) at high temperature. The biaxial strain is induced as the bonded pair returns to ambient temperature (see Figure 41). The applied biaxial tensile strain was calculated to be 0.123%. Pre- and post-strain measurements were carefully made using an Agilent 4155 Parameter Analyzer.

4.2.1 nFET Results and Discussion

Figure 42 depicts the output characteristics of a 1.8V, high V_T, 10×10 μm nFET. Post strain, there is a 9.52% increase in the saturation current (I_{sat}), as well as a reduction in channel

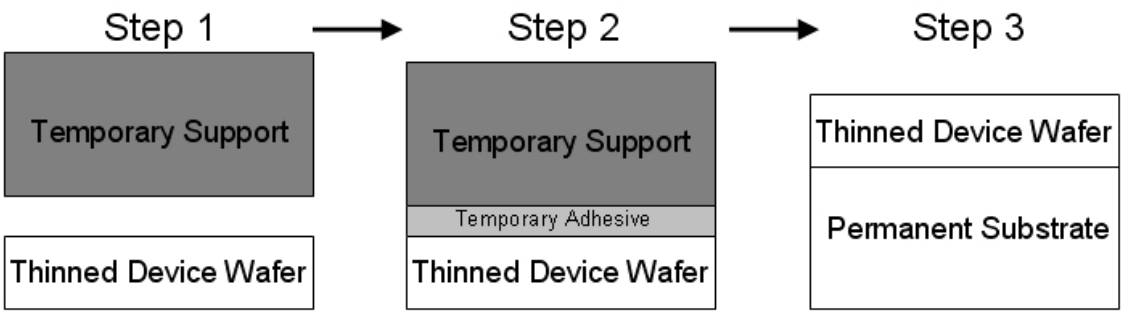

Figure 41: Process flow for the planar biaxial strain by differential thermal bonding.

resistance. Figure 43 illustrates the corresponding transfer characteristics for pre- and post-strain, both on linear and log scales. The post-strain leakage floor increase is believed to be a measurement artifact in this particular device, and in general there was no observed change in the leakage floor pre- and post-strain. The pre- and post- strain transconductance (g_m) is shown in Figure 44. As expected from the transfer characteristics, there is a 9.94% increase in g_m after strain. The effective mobility (μ_{eff}) versus effective field (E_{eff}) for a 1.8V, high V_T, 10 × 10 μm nFET is shown in Figure 45. After strain, the μ_{eff} is improved by 9.54%.

The following equation was used in the calculations:

$$\mu_{eff} = \frac{g_d}{\left(\frac{W}{L}\right) Q_i} \tag{23}$$

for

$$Q_i = C_{ox} \left(V_{GS} - V_T\right) \tag{24}$$

where g_d is the drain conductance ($\partial I_{DS}/\partial V_{DS}$) and C_{ox} is the oxide capacitance. Note the pre- and post- strain V_T was extracted using the peak transconductance technique as described in Chapter III. The vertical effective electric field was calculated using the following equation for nFETs [50]:

$$E_{eff} = \frac{V_{GS} + V_T}{6t_{ox}} \tag{25}$$

where t_{ox} is the oxide thickness.

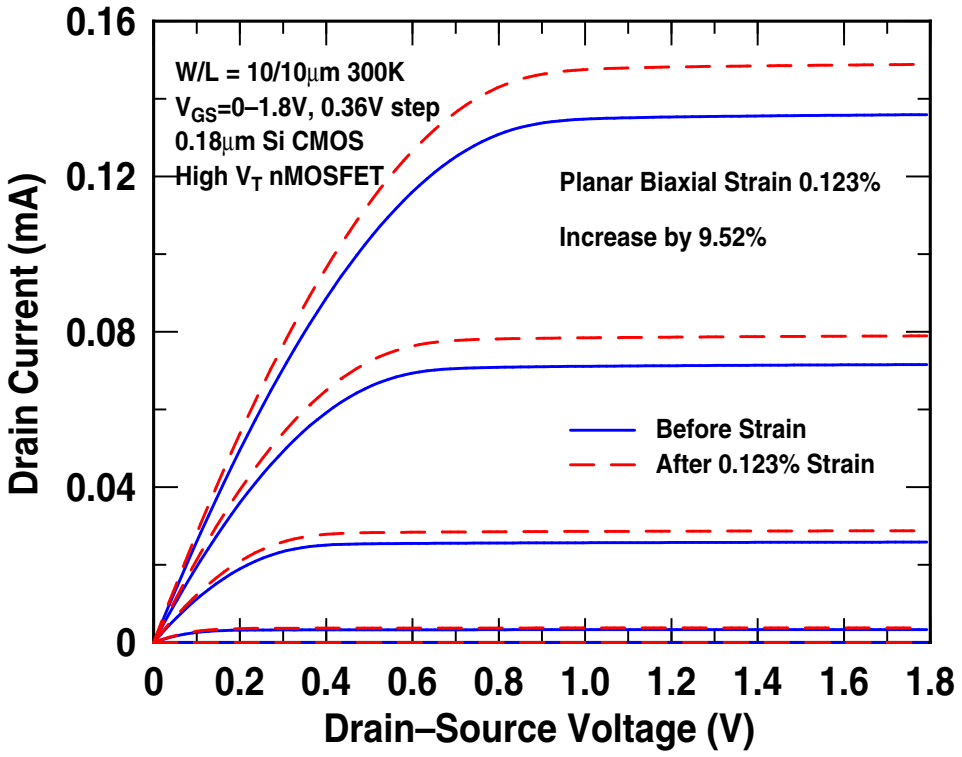

Figure 42: nFET output characteristics for both pre-strain and post 0.123% strain.

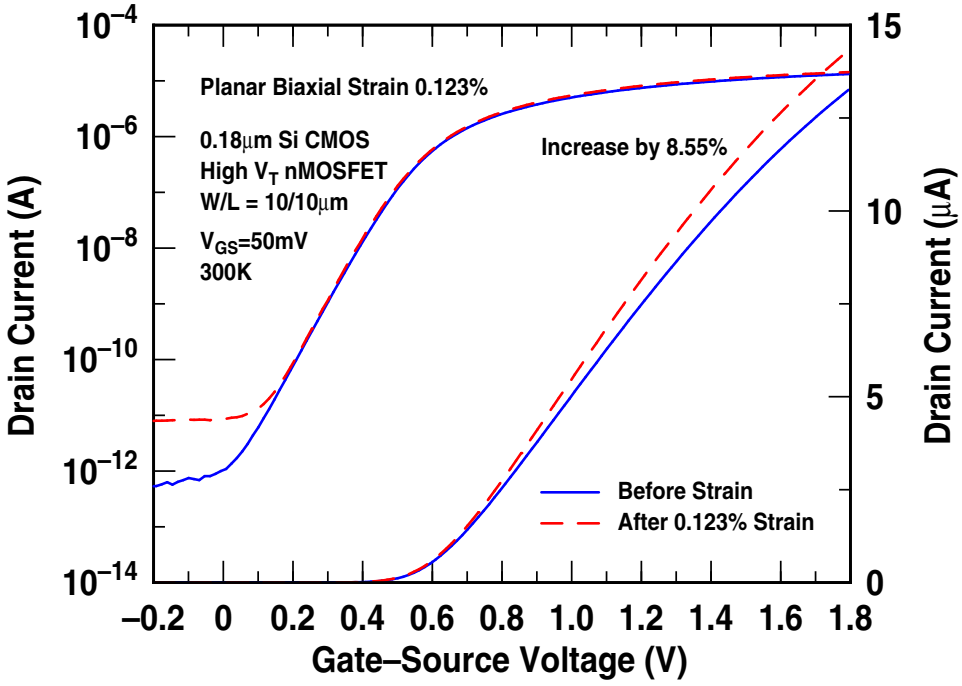

Figure 43: nFET transfer characteristics for both pre-strain and post 0.123% strain.

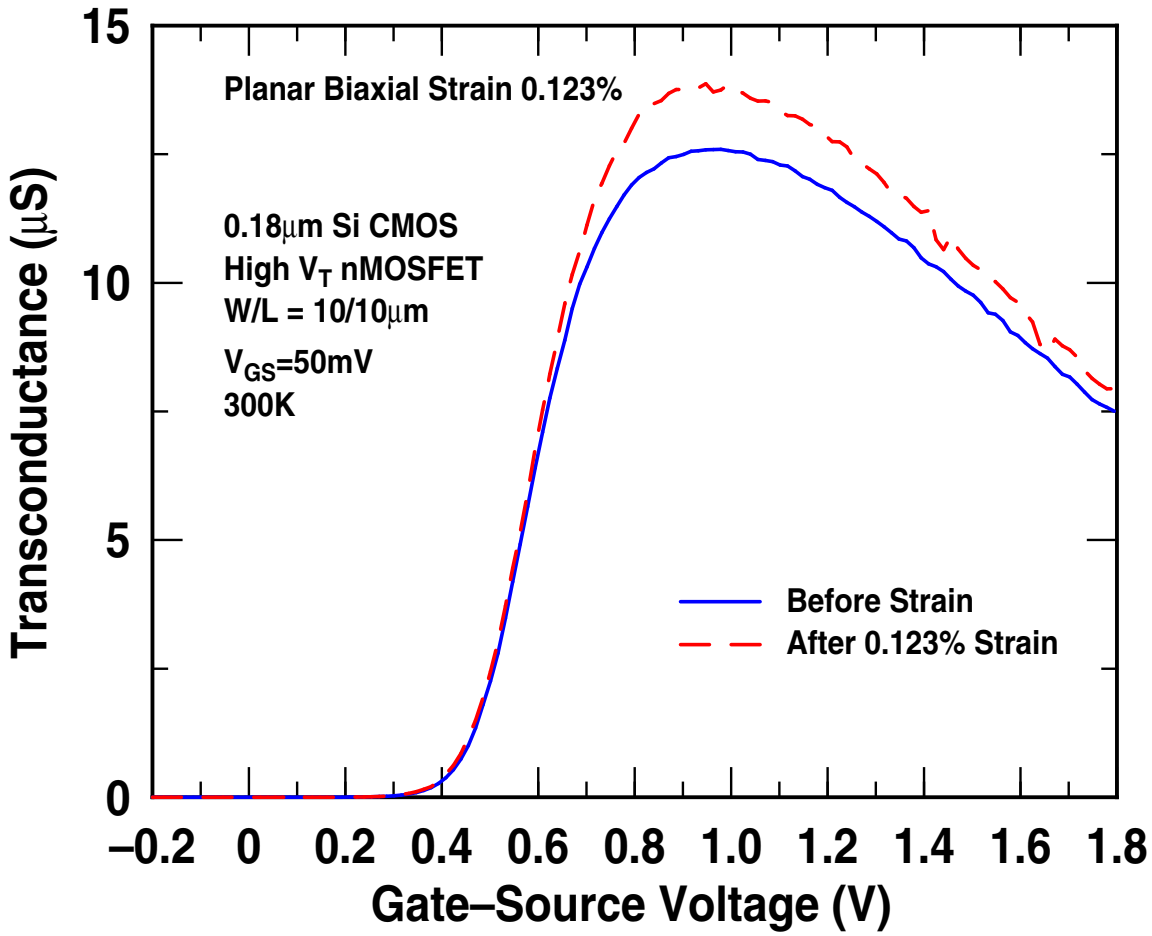

Figure 44: nFET transconductance for both pre-strain and post 0.123% strain.

The enhanced nFET performance with strain is attributed to the reduction of both the in-plane effective mass and intervalley scattering [51], [52]. As Figure 39 indicates, biaxial strain lifts the six-fold degeneracy of the Si conduction band. The energy of the two perpendicular valleys (Δ_2) is lowered with respect to the four in-plane valleys (Δ_4). Since electrons prefer to occupy the lowest energy state, they will preferentially populate the lower energy Δ_2 valleys. The inplane effective mass is lower in the Δ_2 valleys ($m^* = 0.19m_o$) leading to increased electron low-field effective mobility. Another cause of the increase in electron mobility is the suppression of intervalley phonon-carrier scattering between the Δ_2 and Δ_4 valleys. The reduction in scattering is also attributed to the conduction band energy splitting.

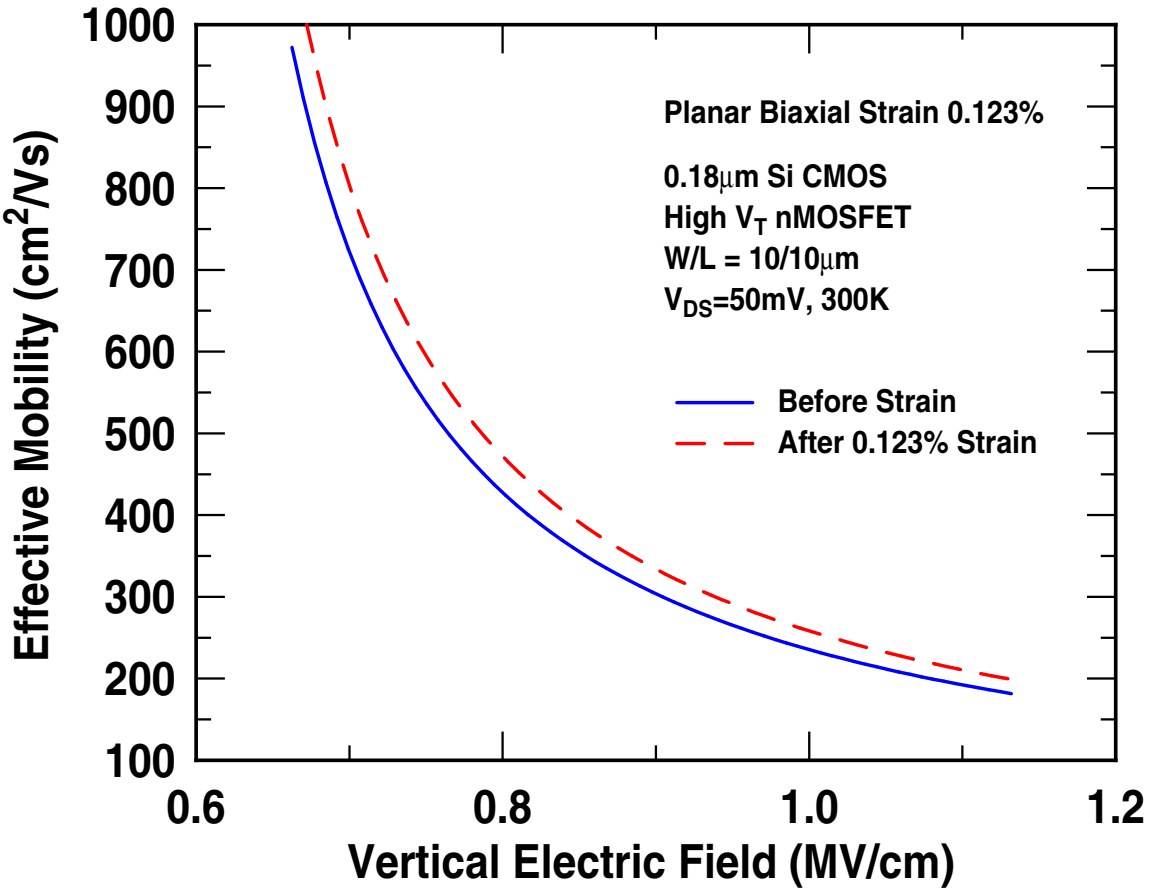

Figure 45: nFET μ_{eff} vs E_{eff} for pre-strain and post 0.123% strain.

The percentage change in I_{sat} and effective mobility (μ_{eff}) versus drawn channel length for 1.8V (nominal and high V_T) and 3.3V nFET devices are shown in Figures 46 and 47, respectively. We see that the nFET I_{sat} improvement and mobility enhancement due to strain decrease as channel length decreases. This result is also reflected in the transfer characteristics, which are not shown here for brevity. Similar trends were observed for the 0.35μm Si CMOS devices in the 0.50μm Si/SiGe BiCMOS technologies. It has been reported that for uniaxial tensile strain applied parallel to the direction of carrier transport, the drain current and mobility are dependent on the channel length, while applied perpendicular strain indicates no dependence on the channel length [53]. In this work, we have biaxial strain which is the tensor addition of strain applied parallel and perpendicular to the direction of carrier transport. The parallel component of low level biaxial strain is dominant for nFETs, as in-

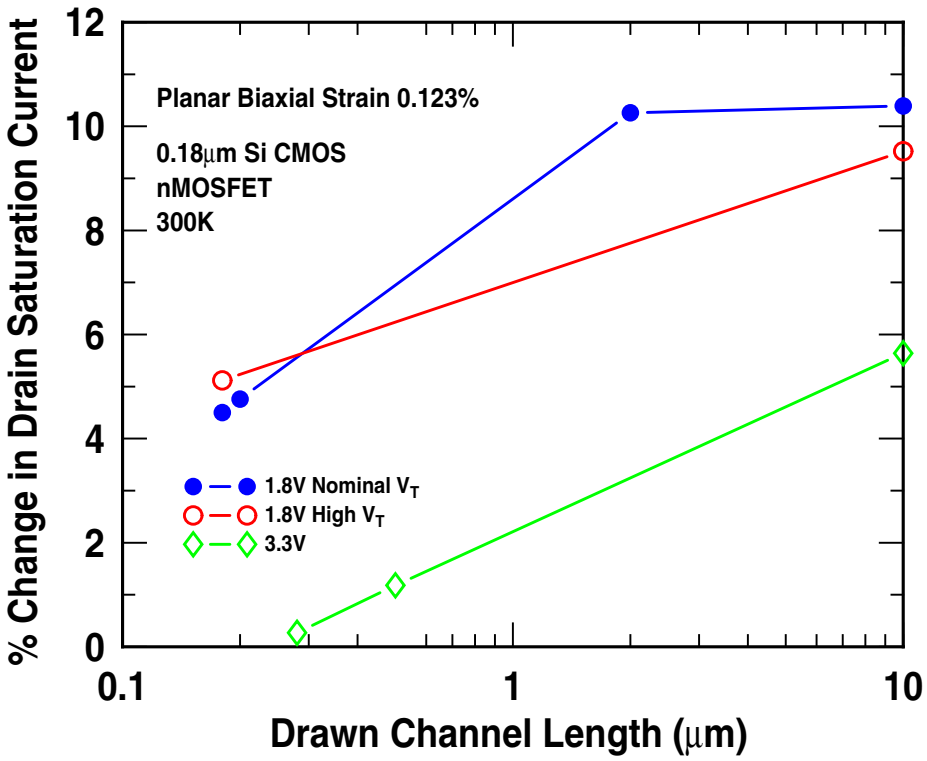

Figure 46: Percent change in I_{sat} as a function of drawn channel length.

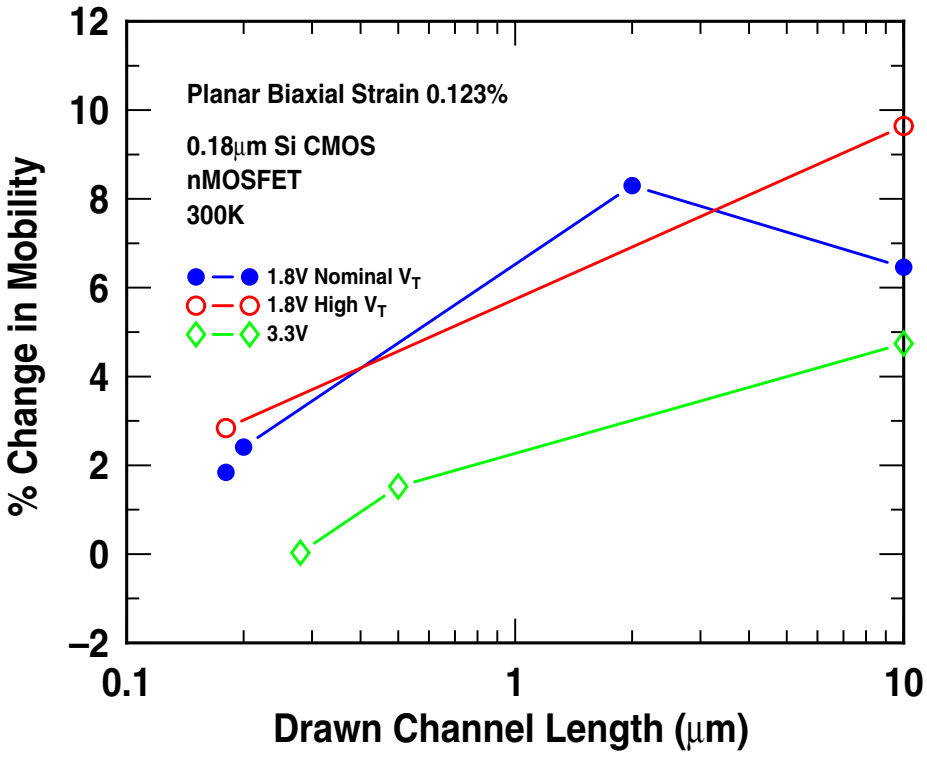

Figure 47: Percent change in μ_{eff} as a function of drawn channel length.

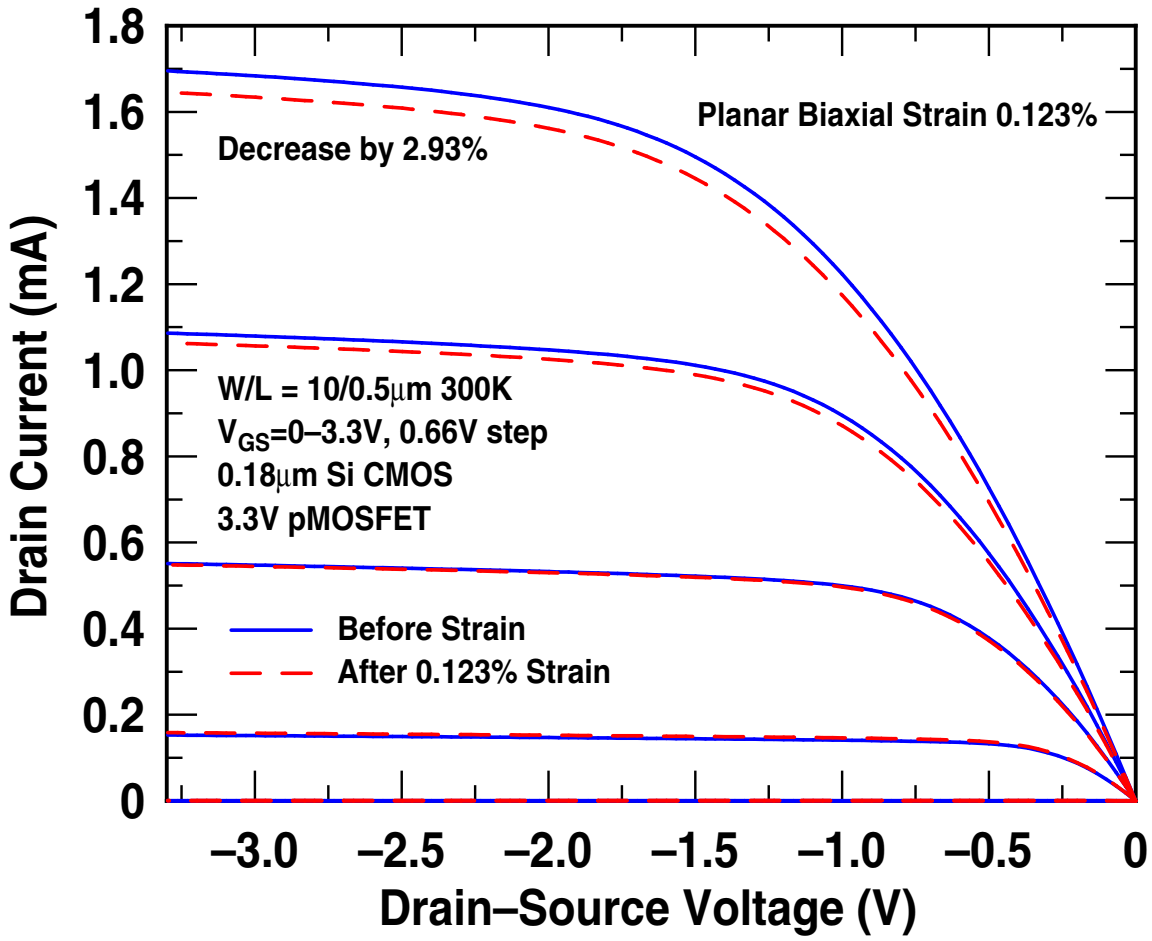

Figure 48: pFET output characteristics for both pre-strain and post 0.123% strain.

dicated by the observed I_{sat} and μ_{eff} channel length dependence. The nFET enhancement due to low level biaxial strain tends to increase with increasing channel length.

4.2.2 pFET Results and Discussion

In Figure 48, the output characteristics of a 3.3V, 10 × 0.5 μm pFET are shown. We see that the applied strain has decreased the saturation current by approximately 2.93%. Again, the corresponding pFET transfer characteristics both linear and log scales are presented in Figure 49. The pre- and post- strain pFET transconductance (g_m) is shown in Figure 50. There is a 4.64% decrease in g_m after strain, as expected. Figure 51 depicts effective mobility (μ_{eff}) versus effective field (E_{eff}) for a 3.3V, 10 × 0.5μm pFET. The pFET μ_{eff} is

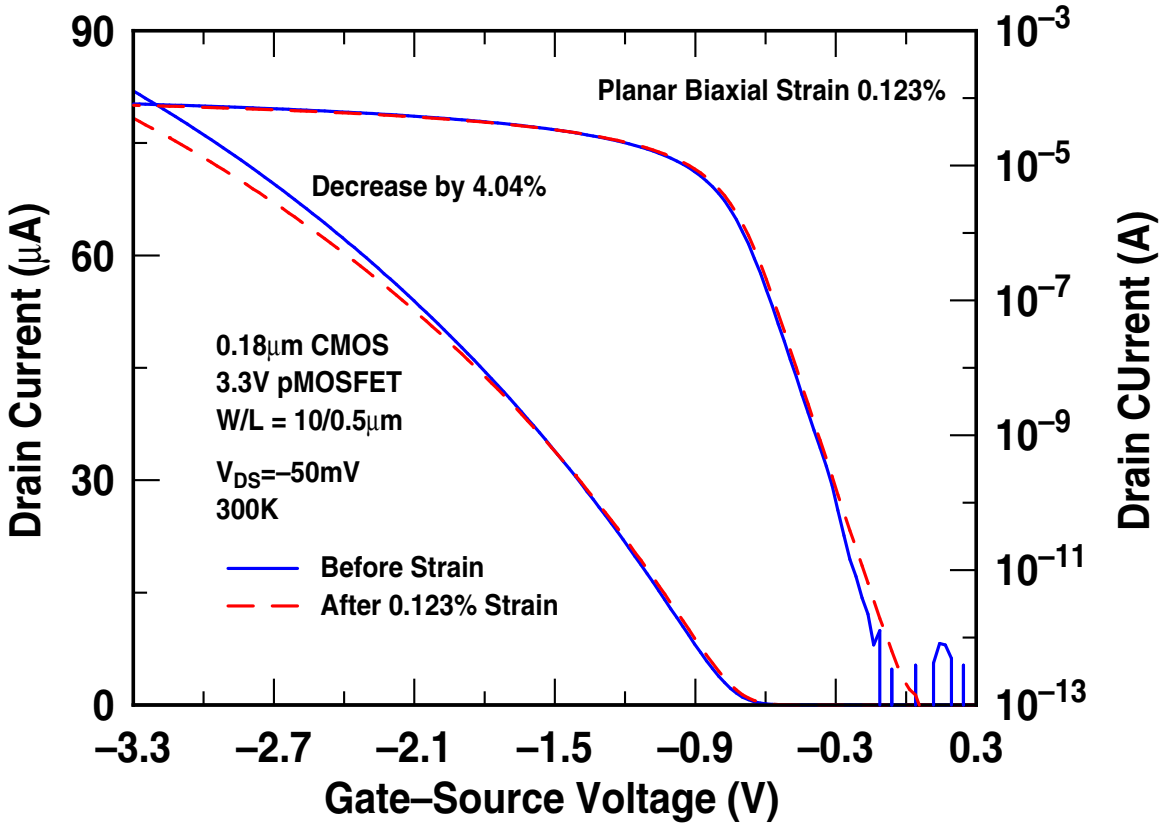

Figure 49: pFET transfer characteristics for both pre-strain and post 0.123% strain.

calculated in the same manor as described in the previous section. The vertical effective electric field was calculated using the following equation for pFETs [50]:

$$E_{eff} = \frac{V_{GS} + 1.5V_T}{7.5t_{ox}} \tag{26}$$

where t_{ox} is the oxide thickness. There is a degradation in μ_{eff} after strain, which is consistent with the results shown in Figures 48 and 49.

Our results indicate that pFET performance, in general, tends to degrade with this method of induced tensile biaxial strain. It is instructive to note that pFETs generally require much larger levels of biaxial tensile strain (1.2%, equivalent to a Ge content of 30%) before significant mobility enhancement is observed [45]. The level of strain reported here is 0.123%, far less than the necessary strain level for substantial mobility enhancement. The degradation observed in pFET mobility is consistent with the results of [54] for low

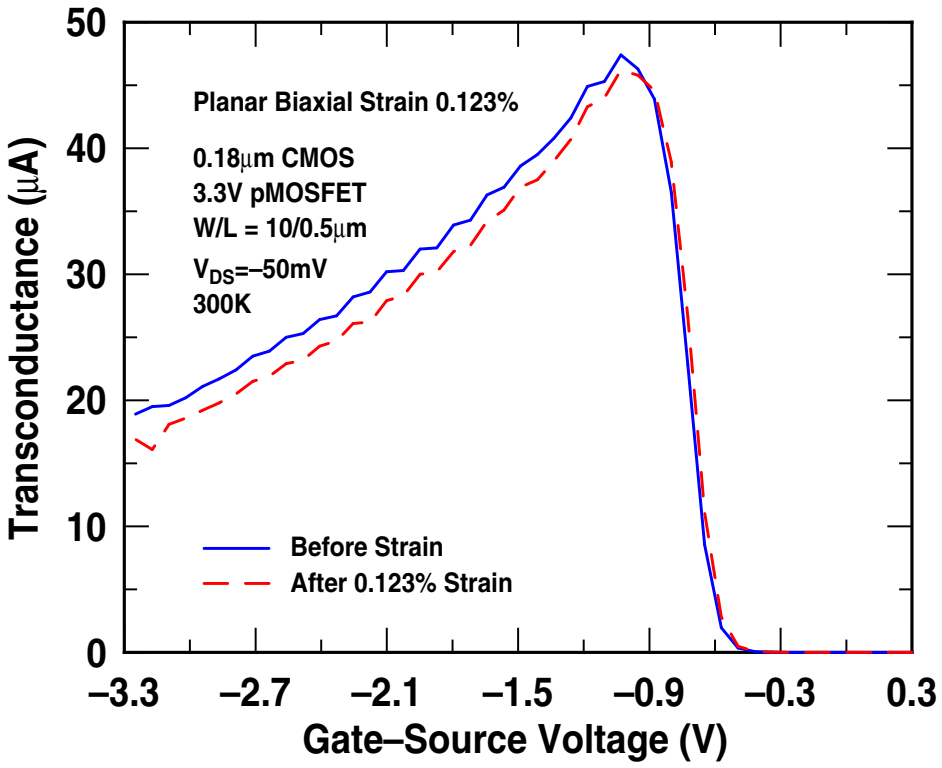

Figure 50: pFET transconductance for both pre-strain and post 0.123% strain.

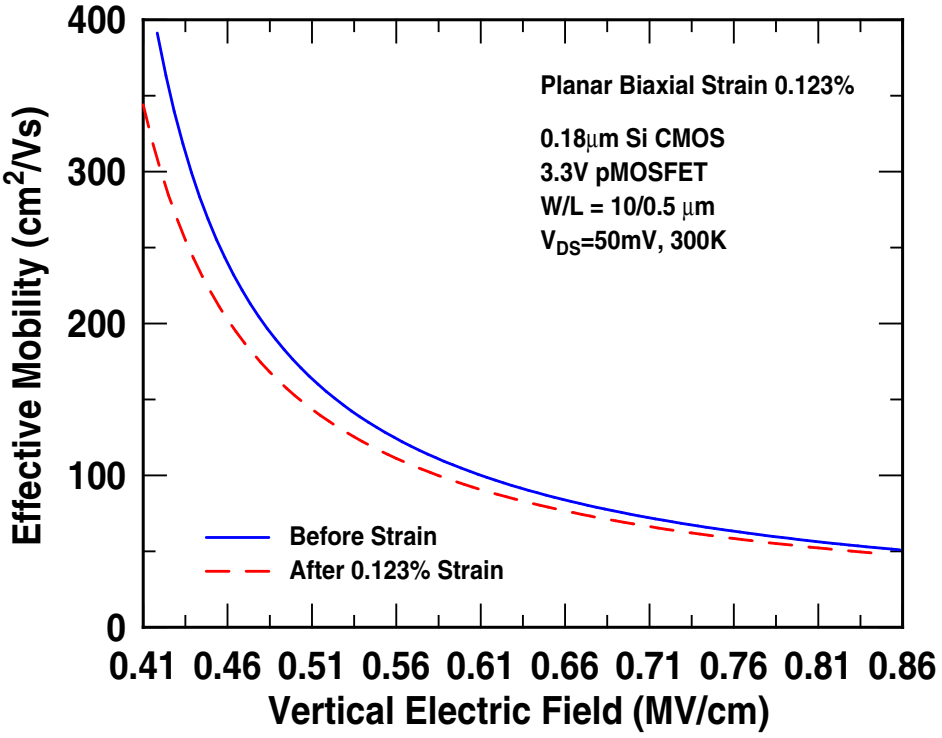

Figure 51: pFET μ_{eff} vs E_{eff} for pre-strain and post 0.123% strain.

strain levels ($\leq 0.52\%$, $\leq 13\%$ Ge content). For these low strain levels, the dominant factor affecting the mobility is the small effective mass variation and the corresponding band/subband repopulation. However for larger strains, band repopulation caused by large strain-induced valance band energy shifts and the reduction of interband scattering lead to the enhancement in mobility [47]. Investigations in pFET strain–channel length dependence were inconclusive. Our results indicate an anomalous shift in pFET threshold voltage (V_T) after strain in many devices, and thus result is still under investigation.

4.3 Summary

The effects of mechanical planar biaxial tensile strain applied, post fabrication, to Si/SiGe HBT BiCMOS technology have been investigated. The results indicate that this method of strain yields enhanced nFET performance and degraded pFET performance. The diminished pFET performance is believed to be due to the low level of strain applied in this method (0.123%). A channel length dependence for the nFETs has been observed. The nFET biaxial strain induced performance improvement increases as the channel length increases.

CHAPTER V

CONCLUSION

5.1 Conclusion

The purpose of this work was to investigate the effects of radiation and strain in various SiGe HBT BiCMOS technologies.

The space community is increasingly using COTS parts in spaceborne systems, thus radiation testing on new commercial technologies is imperative. Chapter III examined the effects of radiation on various SiGe HBT BiCMOS technologies. The effects of proton and gamma irradiation on a new commercially-available SiGe technology were examined for the first time. The results of proton irradiation on a differential SiGe HBT LC oscillator are also reported to gauge the circuit-level impact. We report that proton induces slightly more damage in the SiGe HBT operating in forward-mode, as expected. Surprisingly, the empirical data indicates gamma irradiation creates more damage in the SiGe HBT operating in inverse-mode. Nonetheless, our findings indicate that the *dc*, *ac*, and RF circuit performance is total dose tolerant up to Mrad-level equivalent total dose. A technology comparison is drawn between the results of this work and the three other previously reported SiGe technologies. We find that all reported SiGe HBT technologies to date show acceptable proton radiation tolerance up to Mrad levels.

This chapter also reports on the effects of proton irradiation on the *dc* and *ac* properties of a 130 nm Si CMOS technology. The impact of substrate bias is reported for the first time. Two different irradiation substrate conditions were used, yielding different results. The increasing subthreshold leakage current with increasing equivalent total dose is caused by a combination of two leakage mechanisms, STI edge leakage and GIDL. In the case of 0V irradiation substrate bias, the dominant subthreshold leakage mechanism is STI edge

leakage. However, GIDL is also present and appears to increase with increasing equivalent dose. GIDL is the dominant mechanism for the -1.2V irradiation substrate bias condition and it saturates at high dose. It was observed that the 130 nm CMOS technology investigated in this work is more radiation tolerant than a previously reported 180 nm CMOS technology node.

Chapter IV presents the results of the effects of mechanical planar biaxial tensile strain applied, post fabrication, to SiGe BiCMOS technology. Device characterization was performed before and after strain, under identical conditions. At a strain level of 0.123%, increases in the saturated drain current as well as effective mobility are observed for the nFETs. However, there was a post-strain degradation in the pFET performance. This result is due to the fact that strain-induced performance enhancement in pFETs requires large amounts of strain.

5.2 Future Directions

In Chapter III, the proton and gamma radiation tolerance of a new commercial SiGe HBT technology was investigated. The results for the SiGe HBT operating in the inverse-mode were unexpected, as gamma radiation seemed to cause more damage than proton radiation. This anomalous result could be due to differences in the proton and gamma dose rates. A dose rate study on this technology could shed light on this issue. SEU sensitivity is a well-known issue for SiGe technologies. SEU testing of this technology would be necessary complete radiation hardness assurance of this commercial offering. Also, neutron testing could assist in comparing the effects of ionization and displacement damage in this new technology

Chapter III also reports on the effects of proton radiation on 130 nm CMOS. Two radiation-induced leakage mechanisms were discussed. However, full 3-D simulations are necessary to fully understand the leakage dependence on substrate bias and equivalent total dose.

Chapter IV examines the effects of strain on Si CMOS in various SiGe BiCMOS technologies. Many of the pFETs investigated had an anomalous shift in the threshold voltage post strain. Thus, more experiments are necessary in order to investigate a pFET strain–channel length dependence for this method of strain. Also, inducing different amounts of strain would allow for the investigation of the device performance a function of strain.

REFERENCES

[1] D.C. Ahlgren, J. Dunn, and B. Jagannathan, "SiGe comes of age in the semiconductor industry," *Future Fab International*, vol. 13, July, 2002.

[2] J.D. Cressler, "SiGe HBT technology: A new contender for Si-based RF and microwave circuit applications," *IEEE Transactions on Microwave Theory and Techniques*, vol. 46, pp. 572–589, 1998.

[3] J.D. Cressler and G. Niu, *Silicon-Germanium Heterojunction Bipolar Transistors*, Artech House, Boston, 2003.

[4] B.M. Haugerud, M.B. Nayeem, R. Krithivasan, Y. Lu, C. Zhu, J.D. Cressler, R.E. Belford, and A.J. Joseph, "The effects of mechanical planar biaxial strain in Si/SiGe HBT BiCMOS technology," *Solid-State Electronics*, Accepted for publication, 2005.

[5] B.M. Haugerud, S. Venkataraman, A.K. Sutton, A.P.G. Prakash, J.D. Cressler, G. Niu, P.W. Marshall, and A.J. Joseph, "The impact of substrate bias on proton damage in 130 nm CMOS technology," *IEEE Radiation Effect Data Workshop Record*, Accepted for publication, 2005.

[6] B.M. Haugerud, J.P. Comeau, A.K. Sutton, A.P.G. Prakash, J.D. Cressler, P.W. Marshall, C.J. Marshall, R.L. Ladbury, M. El-Diwany, C. Mitchell, L. Rockett, T. Bach, R. Lawrence, and N. Haddad, "Proton and gamma radiation effects in a new first-generation SiGe HBT technology," *Solid-State Electronics*, Submitted for publication, 2005.

[7] D.C. Ahlgren, G. Freeman, S. Subbanna, R. Groves, D. Greenberg, J. Malinowski, D. Nguyen-Ngoc, S.J. Heng, K. Stein, K. Schonenberg, D. Kiesling, B. Martin, S. Wu, D. Harame, and B. Meyerson, "A SiGe HBT BiCMOS technology for mixed-signal RF applications," *Proceedings of the Bipolar/BiCMOS Circuits and Technology Meeting*, pp. 195–197, 1997.

[8] A. Joseph, D. Coolbaugh, M. Zierak, R. Wuthrich, P. Geiss, Z. He, X. Liu, B. Orner, J. Johnson, G. Freeman, D. Ahlgren, B. Jagannathan, L. Lanzerotti, V. Ramachandran, J. Malinowski, H. Chen, J. Chu, P. Gray, R. Johnson, J. Dunn, S. Subbanna, K. Schonenberg, D. Harame, R. Groves, K. Watson, D. Jadus, M. Meghelli, and A. Rylyakov, "A 0.18 μm BiCMOS technology featuring 120/100 GHz (f_T/f_{max}) HBT and ASIC-compatible CMOS using copper interconnect," *Proceedings of the Bipolar/BiCMOS Circuits and Technology Meeting*, pp. 143–146, 2001.

[9] B.A. Orner, Q.Z. Liu, B. Rainey, A. Stricker, P. Geiss, P. Gray, M. Zierak, M. Gordon, D. Collins, V. Ramachandran, W. Hodge, C. Willets, A. Joseph, J. Dunn, J.-S. Rieh, S.-J. Jeng, E. Eld, G. Freeman, and D. Ahlgren, "A 0.13μm BiCMOS technology

featuring a 200/280 GHz (f_T /f_{max}) SiGe HBT," *Proceedings of the Bipolar/BiCMOS Circuits and Technology Meeting*, pp. 203-206, 2003.

[10] H. Kromer, " Two integral relations pertaining to electron transport through a bipolar transistor with a nonuniform energy gap in the base region," *Solid-State Electronics*, vol. 28, pp. 1101–1103, 1985.

[11] E.J. Prinz, P.M. Garone, P.V. Schwartz, X. Xiao, and J.C. Sturm, "The effect of emitter-base spacers and strain-dependent density-of-states in Si/SiGe/Si heterojunction bipolar transistors," *Technical Digest IEEE International Electron Device Meeting*, pp. 639–642, 1989.

[12] D.L. Harame, J.H. Comfort, J.D. Cressler, E.F. Crabbé, J.Y-C. Sun, B.S. Meyerson, and T. Tice, "Si/SiGe epitaxial-base transistors – part I: materials, physics, and circuits," *IEEE Transactions on Electron Device*, vol. 42, pp. 455–468, 1995.

[13] S.S. Iyer, G.L. Patton, J.M.C. Stork, B.S. Meyerson, and D.L. Harame, "Heterojunction bipolar transistors using Si-Ge alloys," *IEEE Transactions on Electron Device*, vol. 36, pp. 2043–2064, 1989.

[14] J. Barth, "Modeling space radiation environments," Short Course Notes, *IEEE Nuclear Space and Radiation Effects Conference*, 1997.

[15] J.R. Srour and J.M. McGarrity, "Radiation Effects on Microelectronics in Space," *Proceedings of the IEEE*, vol. 76, pp. 1443-1469, 1988.

[16] C. Claeys and E. Simoen, *Radiation Effects in Advanced Semiconductor Materials and Devices*, Springer, Berlin, 2002.

[17] F.B. McLean and T.R. Oldham, "Basics mechanisms of radiation effects in electronic materials and devices," *US Army Lab Command*, HDL-TR-2129, US Army Command, Harry Diamond Laboratories, MD, USA, 1987.

[18] J.R. Srour, C.J. Marshall, and P.W. Marshall, "Review of displacement damage effects in silicon devices," *IEEE Transactions on Nuclear Science*, vol. 50, pp. 653-670, 2003.

[19] C. Marshall and P. Marshall, "Proton effects and test issues for satellite designers - Part B: Displacement effects," Short Course Notes, *IEEE Nuclear Space Radiation Effects Conference*, 1999.

[20] E. Zhao, A.K. Sutton, B.M. Haugerud, J.D. Cressler, P.W. Marshall, R.A. Reed, B. El-Kareh, S. Balster, and H. Yasuda, "The effects of radiation on 1/f noise in complementary (*npn* + *pnp*) SiGe HBTs," *IEEE Transactions on Nuclear Science*, vol. 51, pp. 3243-3249, 2004.

[21] J.P. Comeau, A.K. Sutton, B.M. Haugerud, J.D. Cressler, W-M.L. Kuo, P.W. Marshall, R.A. Reed, A. Karroy, and R. Van Art, "Proton tolerance of advanced SiGe HBTs fabricated on different substrate materials," *IEEE Transactions on Nuclear Science*, vol. 51, pp. 3743-3247, 2004.

[22] X. Lui and S. Mourad, “Performance of submicron CMOS devices and gates with substrate biasing,” *IEEE International Symposium on Circuits and Systems*, vol. 4, pp. 9-12, 2000.

[23] L.T. Clark, M. Morrow, and W. Brown, “Reverse-body bias and supply collapse for low effective standby power,” *IEEE Transactions on Very Large Scale Integration(VLSI) Systems*, vol. 12, pp. 947-956, 2004.

[24] S. Terry, B.J. Blalock, L. Yong, B. Dufrene, and M. Mojarradi, “Complementary body driving - A low voltage analog circuit technique for SOI,” *Proceedings of the IEEE International SOI Conference*, pp. 80-82, 2002.

[25] K.M. Murray, W.J. Stapor, and C. Casteneda, "Calibrated charged particle radiation system with precision dosimetric measurement and control," *Nuclear Instruments and Methods in Physics Research*, vol. A281, pp. 616-621, Sept. 1989.

[26] P.W. Marshall, C.J. Dale, M. A. Carts, and K.A. LaBel, "Particle-induced bit errors in high performance fiber optic data links for satellite data management", *IEEE Transactions on Nuclear Science*, vol. 41, No. 41, pp. 1958-1965, December 1994.

[27] S. Zhang, J.D. Cressler, G. Niu, C.J. Marshall, P.W. Marshall, H.S. Kim, R.A. Reed, M.J. Palmer, A.J. Joseph, and D.L. Harame, “The effects of operating bias conditions on the proton tolerance of SiGe HBTs,” *Solid-State Electronics*, vol. 47, pp. 1729-1734, 2003.

[28] S. Zhang, G. Niu, J.D. Cressler, S.D. Clark, and D.C. Ahlgren, “The effects of proton irradiation on the RF performance of SiGe HBTs,” *IEEE Transactions on Nuclear Science*, vol. 46, NO. 6, pp. 1716-1721, December 1999.

[29] J.D. Cressler, R. Krithivasan, G. Zhang, G. Niu, P.W. Marshall, H.S. Kim, R.A. Reed, M.J. Palmer, and A.J. Joseph, “An investigation of the origins of the variable proton tolerance in multiple SiGe HBT BiCMOS technology generations,” *IEEE Transactions on Nuclear Science*, vol. 49, pp. 3203-3207, 2002.

[30] J.D. Cressler, R. Krithivasan, A.K. Sutton, J.E.Seiler, J.F. Krieg, S.D. Clark, and A.J. Joseph, “The impact of gamma irradiation on SiGe HBTs operating at cryogenic temperature,” *IEEE Transactions on Nuclear Science*, vol. 50, pp. 1805-1810, 2003.

[31] T.K. Johansen and L.E. Larson, “Optimization of SiGe HBT VCOs for wireless applications,” *IEEE Radio Frequency Integrated Circuits Symposium*, pp.273-275, 2003.

[32] B. El-Kareh, S. Balster, W. Leitz, P. Steinmann, H. Yasuda, M. Corsi, K. Dawoodi, C. Dirnecker, P. Foglietti, A. Haeusler, P. Menz, M. Ramin, T. Scharnagl, M. Schiekofer, M. Schober, U. Schulz, L. Swanson, D. Tatman, M. Waitschull, J.W. Weijtmans, and C. Willis, “A 5 V complementary-SiGe BiCMOS technology for high-speed precision analog circuits,” *Proceedings of the Bipolar/BiCMOS Circuits and Technology Meeting*, pp. 211-214, 2003.

[33] M. Racanelli and P. Kempf, "SiGe BiCMOS technology for communication products," *Proceedings of the IEEE Custom Integrated Circuits Conference*, pp. 331-334, 2003.

[34] D.K. Schroder, *Semiconductor Material and Device Characterization*, Wiley, New York, 1990.

[35] E. Simoen, J. Hermans, A. Mercha, W. Vereecken, C. Vermoere, C. Claeys, E. Augendre, G. Badenes, and A. Mohammadzadeh, "60 MeV proton irradiation effects on NO-annealed and standard-oxide deep submicron MOSFETs," *IEEE European Conference on Radiation and Its Effects on Components and Systems*, pp. 69-76, 2001.

[36] G. Niu, J.D. Cressler, S.J. Mathew, and S. Subbanna, "A total resistance slope-based effective channel mobility extraction method for deep submicrometer CMOS technology," *IEEE Transactions on Electron Devices*, vol. 46, pp. 1912-1914, 1999.

[37] G. Niu, S.J. Mathew, G. Banerjee, J.D. Cressler, S.D. Clark, M.J. Palmer, and S. Subbanna, "Total dose effects on the shallow-trench isolation leakage current characteristics in a 0.35μm SiGe BiCMOS technology," *IEEE Transactions on Nuclear Science*, vol. 46, pp. 1841-1847, 1999.

[38] T. Chan, J. Chen, P. Ko, and C. Hu, "The impact of gate-induced drain leakage on MOSFET scaling," *IEEE Technical Digest International Electron Devices Meeting*, pp. 721-724, 1987.

[39] S.A. Parke, J.E. Moon, H.C. Wann, P.K. Ko, and C. Hu, "Design for suppression of gate-induced drain leakage in LDD MOSFETs using a quasi-two-dimensional analytical model," *IEEE Transactions on Electron Devices*, vol. 39, pp. 1694-1703, 1992.

[40] N.R. Mohapatra, S. Mahapatra, and V.R. Rao, "The study of damage generation in n-channel MOS transistors operating in the substrate enhanced gate current regime," *IEEE Proceedings of the International Symposium on the Physical and Failure Analysis of Integrated Circuits*, pp. 27-30, 2002.

[41] Y. Li, J.D. Cressler, Y. Lu, J. Pan, G. Niu, R.A. Reed, P.W. Marshall, C. Polar, M.J. Palmer, and A.J. Joseph, "Proton tolerance of multiple-threshold voltage and multiple-breakdown voltage CMOS device design points in a 0.18μm system-on-a-chip CMOS technology," *IEEE Transactions on Nuclear Science*, vol. 50, pp. 1834-1838, 2003.

[42] J.L. Hoyt, " Enhanced mobility CMOS," *Electrochemical Society Proceedings*, vol. 7, pp. 15-24, 2004.

[43] K. Rim, R. Anderson, D. Boyd, F. Cardone, K. Chan, H. Chen, S. Christansen, J. Chu, K. Jenkins, T. Kanarsky, S. Koester, B.H. Lee, K. Lee, V. Mazzeo, A. Mocuta, D. Mocuta, P.M. Mooney, P. Oldiges, J. Ott, P. Ronsheim, R. Roy, A. Steegen, M. Yang, H. Zhu, M. Ieong, and H.-S.P. Wong, "Strained Si CMOS (SS CMOS) technology: opportunities and challenges," *Solid-State Electronics*, vol. 47, pp. 1133-1139, 2003.

[44] S.E. Thompson, M. Armstrong, C. Auth, M. Alavi, M. Buehler, R. Chau, S. Cea, T. Ghani, G. Glass, T. Hoffman, C.-H. Jan, C. Kenyon, J. Klaus, K. Kuhn, Z. Ma, B. Mcintrye, K. Mistry, A. Murthy, B. Obradovic, R. Nagisetty, P. Nguyen, S. Sivakumar, R. Shaheed, L. Shifren, B. Tufts, S. Tyagi, M. Bohr, Y. and El-Mansy, "A 90-nm logic technology featuring strained silicon," *IEEE Transactions on Electron Devices*, vol. 51, pp. 1790-1797, 2004.

[45] B.M. Haugerud, L.A. Bosworth, and R.E. Belford, "Mechanically induced strain enhancement of metal-oxide-semiconductor field effect transistors," *Journal of Applied Physics*, vol. 94, pp. 4102-4107, 2003.

[46] C.W. Liu, S. Maikap, M.H. Liao, F. Yuan, and M.H. Lee, "BiCMOS devices under mechanical strain," *Electrochemical Society Proceedings*, vol. 7 pp. 437-448, 2004.

[47] M.V. Fischetti, Z. Ren, P.M. Solomon, M. Yang, and K. Rim, "Six-band kp calculation of the hole mobility in silicon inversion layers: Dependence on surface orientation, strain, and silicon thickness," *Journal of Applied Physics*, vol. 94, pp. 1079-1095, 2003.

[48] R.E. Belford, U.S. Patent, No. 6,455,397 B1 (Sept. 2002).

[49] R.E. Belford, U.S. Patent, No. 6,514,836 B2 (Feb. 2003).

[50] K. Chen, H.C. Wann, J. Dunster, P.K. Ko, and C. Hu, "MOSFET carrier mobility model based on gate oxide thickness, threshold, and gate voltages," *Solid State Electronics*, vol. 39, pp. 1515-1518, 1996.

[51] S. Takagi, "Subband structure engineering for realizing scaled CMOS with high performance and low power consumption," *IEICE Transactions on Electronics*, vol. E85-C, pp. 1064-1072, 2002.

[52] M.V. Fischetti, F. Gámiz , W. Hänsch, "On the enhanced electron mobility in strained-silicon inversion layers," *Journal of Applied Physics,* vol. 92, pp. 7320-7324, 2002.

[53] W. Zhao, J. He, R.E. Belford, L.-E. Wernersson, and A. Seabaugh, "Partially depleted SOI MOSFETs under uniaxial tensile strain," *IEEE Transactions on Electron Devices*, vol. 51 pp. 317-323, 2004.

[54] K. Rim, J. Chu, H. Chen, K.A. Jenkins, T. Kanarsky, K. Lee, A. Mocuta, H. Zhu, R. Roy, J. Newbury, J. Ott, K. Petarca, P. Mooney, D. Lacey, S. Koester, K. Chan, D. Boyd, M. Ieong, and H.-S. Wong, "Characteristics and device design of sub-100 nm strained Si n- and pMOSFETs," *Symposium on VLSI Technology Technical Digest*, pp. 98-99, 2002.